VERIFICATION, OPTIMIZATION AND REFINEMENT OF A DIRECT-INVERSE TRANSONIC WING DESIGN METHOD INCLUDING WEAK VISCOUS INTERACTION

A Thesis

by

ROBERT R. RATCLIFF

Submitted to the Office of Graduate Studies of
Texas A&M University
in partial fulfillment of the requirements for the degree of

MASTER OF SCIENCE

August 1989

Major Subject: Aerospace Engineering

VERIFICATION, OPTIMIZATION AND REFINEMENT OF A DIRECT-INVERSE TRANSONIC WING DESIGN METHOD INCLUDING WEAK VISCOUS INTERACTION

A Thesis

by

ROBERT R. RATCLIFF

Approved as to style and content by:

Leland A. Carlson
(Chair of Committee)

Cyrus Ostowari
(Member)

Erian A. Baskharone
(Member)

Walter E. Haisler
(Head of Department)

August 1989

ABSTRACT

Verification, Optimization and Refinement of a Direct-Inverse Transonic Wing Design Method Including Weak Viscous Interaction. (August 1989)

Robert R. Ratcliff, B.S., Texas A&M University

Chair of Advisory Committee: Dr. Leland A. Carlson

New developments in the direct-inverse wing design method in curvilinear coordinates are presented. A spanwise oscillation problem and proposed remedies are discussed. Test cases are presented which reveal the approximate limits on wing aspect ratio and leading edge sweep angle for a successful design, and which show the significance of spanwise grid skewness, grid refinement, viscous interaction, the initial airfoil section and Mach number - pressure distribution compatibility on the final design. Furthermore, preliminary results are shown which indicate that it is feasible to successfully design a region of the wing which begins aft of the leading edge and terminates prior to the trailing edge.

ACKNOWLEDGMENTS

The work presented in this paper was primarily supported by the National Aeronautics and Space Administration under Grant NAG-1-619 with Richard L. Campbell of the Langley Research Center as technical monitor. The author expresses his appreciation to Dr. Carlson for his support, guidance, and patience and to Thomas Gally for his assistance and helpful suggestions. Much thanks also goes to the Computer Service Center at Texas A&M University for their very generous computer support.

NOMENCLATURE

A	influence coefficients used in compensation terms
AR	aspect ratio
cos	cosine
c	local chord
C_l	airfoil section lift coefficient
C_L	wing lift coefficient
C_p	pressure coefficient
c_p	specific heat at constant pressure
cosh	hyperbolic cosine
F	Wing surface function in the physical domain
a	speed of sound
$a_{i,j}$	Fourier coefficients used in grid scheme
d	the relative x distance from the sectional quarter chord point
f	general function
$\|h\|$	determinant of the inverse jacobian matrix
H	inverse Jacobian transformation matrix
h	enthalpy per unit mass
I, J, K	grid locations in ξ, η, ζ directions
J	Jacobian transformation matrix
M	Mach number

P, Q, R	Jameson's upwinding terms
p	pressure
Q	compensation terms
q	magnitude of physical velocity
r	radius, radial distance; coefficient of determination
Re	Reynolds number
R_f	radius of fuselage
R_t	radius of wing tip
S	coordinates of the wing's surface in the auxiliary plane
S	wing surface function in the computational domain
S_w	arc length along approximated wake location
U	velocity at the edge of the boundary layer
$\mathbf{U}$	velocity vector in Cartesian coordinates
u , v , w	velocity components in Cartesian coordinates
U, V, W	contravariant velocity components
$\mathbf{V}$	velocity vector in computational space
x, y, z	Cartesian coordinates
y_{design}	ordinate of the design section
y_{mean}	mean ordinate of the target section
y_t	ordinate of airfoil at trailing edge
z	$\bar{x} + i\bar{\theta}$
α	angle of attack

β	angle between the wall shear line and the external streamline of the boundary layer
Δ	transformed boundary layer displacement thickness
Δl	magnitude of change in the airfoil surface in physical coordinates
Δ_t	user specified trailing edge thickness in units of chord fraction
δ	central-difference operator defined in Eq. (2-20)
δ_r	relofting correction
δ^*	boundary layer displacement thickness
ϵ	degree of extrapolation coefficient
γ	ratio of specific heats
Γ	circulation
κ_w	flow curvature at the approximate wake location
μ	averaging operator defined in Eq. (2-20)
∇	vector differential operator
ϕ	reduced velocity potential function
Φ	velocity potential function
ρ	density
σ	smoothing operator, standard deviation
sinh	hyperbolic sine
τ	airfoil section thickness
τ_1	original airfoil thickness
τ_2	airfoil thickness at different Mach number
θ	momentum thickness

ε	degree of smoothing coefficient
ξ', η'	coordinates in auxiliary plane
ξ, η, ζ	transformed coordinates

Subscripts

avg	average quantity
$idle$	forward direct-inverse interface
$idte$	aft inverse-direct interface
II	index increment
i, j, k	grid locations in the ξ, η, ζ directions
ky	value at the wing's surface
l	lower surface
le	leading edge
o	stagnation conditions
s	singular line location
T	iteration time level
te	trailing edge
u	upper surface
w	wake
x, y, z	components in the x, y, z directions
∞	freestream conditions
ξ, η, ζ	components in the ξ, η, ζ directions

Superscripts

n	iteration time level
o	degrees

TABLE OF CONTENTS

LIST OF TABLES

LIST OF FIGURES

Figure Page

CHAPTER I

INTRODUCTION

With the advent of efficient numerical schemes that accurately model the irrotational transonic flow about complex configurations such as wing-bodies and the appearance of computers with memory capacities and computational speeds necessary to execute these schemes in a reasonable amount of time, the efficient design of wings for transonic flight is quickly becoming a reality. Although transonic potential schemes combined with integral boundary layer solvers may not model the real flowfield as accurately as Euler or Navier Stokes schemes,[1–3] their use can significantly reduce the costs and time expenditures associated with transonic wing design.

There are basically two general types of inverse design methods: inverse solvers and predictor/corrector (P/C) methods. In the P/C type methods, an analysis code is used to calculate the flowfield for an arbitrary initial geometry; and then, this geometry is systematically modified by considering the differences between the calculated and target pressures. The changes to the airfoil sections can be obtained through optimization type procedures; or, as shown by Campbell,[4] the appropriate geometry changes can be systematically determined by using a design algorithm which relates pressure changes to changes in airfoil curvature.

An example of an inverse solver is the direct-inverse transonic wing analysis-design method, which has been under development at Texas A&M University.[5–15] In

Journal model is *AIAA Journal of Aircraft* this method, the wing geometry is determined by specifying pressure distributions over part of the wing and then solving the mixed Neumann and Dirichlet boundary value problem associated with the full potential equation for compressible flow via finite difference and/or finite-volume techniques. The specified pressure distributions can be selected by the experienced designer to have such desirable characteristics as weak or nonexistent shock waves, a slowly increasing adverse pressure gradient to limit boundary layer separation, a center of pressure location giving a desirable pitching moment, or an efficient spanwise loading. The designer may also use wind-tunnel tests of successful airfoils as an aid in picking a desirable pressure distribution. The direct-inverse technique has been successfully used in stretched and sheared Cartesian coordinate systems[5-12,16,17] and most recently by Gally[13-15] in a curvilinear coordinate system.

It would be convenient if only the inviscid flowfield had to be included in the design process; but, unfortunately, it has been verified through transonic wind tunnel tests at low Reynold's numbers and flight testing at high Reynold's numbers that viscous effects are very significant[18]. For example, as the Reynold's number increases, the shock wave location is further aft on the wing. Thus, the shock wave in a viscous flowfield (finite Re) is located further upstream than that predicted by an inviscid (infinite Re) flowfield calculation. Although the inclusion of the viscous interaction significantly weakens the shock strength compared to inviscid results, the accompanying upstream displacement of the shock wave causes the sum of the differences between the upper and lower surface pressure distributions to be smaller than in the inviscid case; hence, the wing lift coefficient will be smaller in the viscous case.

Furthermore, it has been discovered that a wing using an aft-cambered airfoil section designed inviscidly for transonic conditions might develop 25-50% less lift in a viscous environment[9].

In light of the previous discussion its obvious that viscous effects must be taken into account through some means. One approach that applies in cases where there are no regions of massive separation is referred to as the weak viscous interaction technique. Since the weak primary viscous interaction effect is the formation of a boundary layer on the wing which effectively makes the airfoil thicker, the external streamlines for the wing boundary of the inviscid potential field are shifted outwards by a distance called the displacement thickness. This shifting is due to the decrease in velocity of the fluid in the boundary layer[19]. Thus, to include the effects of weak viscous interaction in an analysis of a wing, one simply needs to determine the potential solution for the surface, find the displacement thickness using the properties associated with the streamline representing the body, add this displacement thickness to the original surface, and repeat the process until the displacement thicknesses and the potential field converge.

Weak viscous interaction can be included in the inverse design process in much the same way. In the inverse regions, where the pressure boundary condition is applied, the new surface which approximately satisfies the boundary condition is calculated periodically by an integration of the flow boundary condition. At that time, the displacement thickness from the boundary layer calculations can be subtracted from this new surface to yield the hard or actual designed airfoil. This process can be carried out iteratively until there is an insignificant change in the displacements due to boundary layer interaction and the inverse boundary condition, and in the flowfield's potential solution.

Fortunately, there is a computer program called TAWFIVE (for Transonic Analysis of a Wing And Fuselage and Interacted Viscous Effects) which not only has the capability of computing the potential field about a wing and fuselage combination but also contains a robust three dimensional integral boundary layer scheme which provides the necessary viscous effects in the form of boundary layer displacement thickness, wake curvature, and wake thickness. It should be noted that a three dimensional boundary layer code is desirable in order to properly predict the increased decambering of the sections near the tip due to the cross flow in the boundary layer[20]. In TAWFIVE, the inviscid numerical scheme is based upon Jameson and Caughey's FLO-30 conservative, finite-volume, full-potential flow method where computations are performed on a body-fitted, sheared, parabolic, wind-tunnel type coordinate system. The three dimensional boundary layer scheme added by Streett[20] to the originally-inviscid code computes the first order, weak, self-consistent, viscous interactions which include the boundary layer displacement effect on the wing's surface, the displacement in the wake, and the curvature/pressure jump in the wake. The boundary layer on the wing is found using a compressible integral method for laminar and turbulent flow with a fixed transition location. The turbulent method was based on work by Smith[21], while the laminar method was developed by Stock[22]. Small regions of separation are also modeled. This latter feature is an important addition for successful convergence, since small regions of separation often occur in the initial stages of computations behind shockwaves, in the cove region of aft-cambered airfoils and near the trailing edge on the upper surface of the wing, even though they may not exist in the final converged solution[11]. The parameters in the wake region are computed in streamwise strips using a two dimensional entrainment integral technique. This method has been deemed valid for transport type wings[20].

Gally[13-15] has successfully incorporated the inverse design process into the TAWFIVE program. Since the modifications made were compatible with the existing computational methods and program structure of TAWFIVE, his work resulted in a versatile design code capable of allowing the user to design an entirely new wing or even discontinuous, nonadjacent segments of a wing. The latter option may be invaluable to engineers who are typically faced with the dilemma of designing around regions where the wing geometry may be fixed by constraints other than aerodynamic considerations. As seen in Fig. 1 these segments can even be non-adjacent upper or lower surfaces with overlapping lower or upper surfaces respectively.

On the other hand, as a consequence of the inverse method, previous experience has revealed that specified pressure distributions may not be imposed in regions less than about ten percent behind the leading edge of the wing section. This limitation was due to the difficulties associated with enforcing the pressure boundary condition near the leading edge of the airfoil where the vertical velocities are large. However this feature was not viewed as a real limitation since the leading edge regions of most airfoils are similar, the leading edge shapes may be constrained by non-aerodynamic factors, and since a leading edge geometry can be selected to produce the desired pressure values at the beginning of the design region[13].

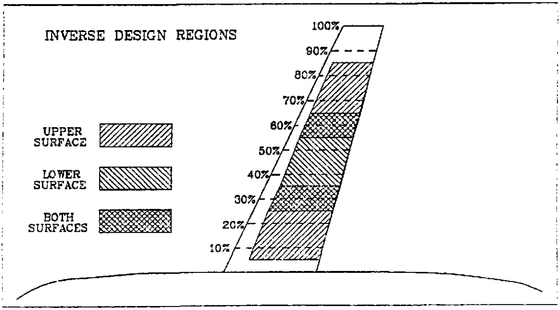

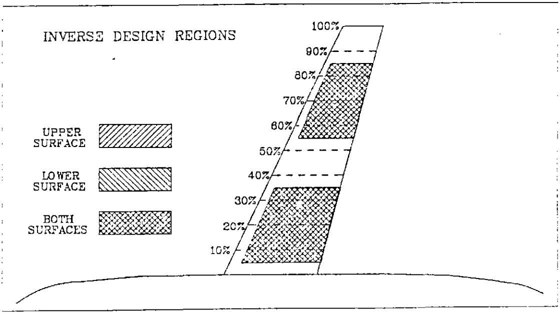

Fig. 1 Typical examples of overlapping and non-adjacent design regions [13]

Moreover, the imposed pressure distributions may often lead to an impractical airfoil that has an excessively blunt trailing edge or one in which the upper or lower surfaces cross prior to the trailing edge resulting in a fish tail shape. An excessively blunt trailing edge might cause a wing to have an excessive amount of drag due to base pressure at the trailing edge, while the fish tail shape would be impossible to construct. Since the nose shape or curvature has been shown to control trailing edge closure,[10,12,23,24] these undesirable shapes can be eliminated with a procedure which systematically modifies the leading edge thickness distribution called relofting. Two types of relofting procedures have already been included in the program by Gally. One is a simple linear rotation scheme where the surface being designed is rotated about the leading edge a proper amount to achieve the desired trailing edge thickness. In the second procedure, the leading edge is proportionally thinned or thickened a proper amount so that the relofted leading edges are in the same family of airfoil shapes.

Gally's original design code has been tested in a variety of ways for a Lockheed Wing-A wing-body. The self-consistency of the approach was tested by designing airfoil sections using certain desired pressure distributions, analyzing the resulting designed airfoils, and then comparing the desired pressure distributions input to those found through analysis. In all of the inviscid cases considered, the code proved itself consistent; the section lift coefficients of the designed and target sections and the respective pressure distributions were in strong agreement. The relofting procedures and the ability of the code to make large surface changes was verified by transforming a 12% thick airfoil at supercritical conditions to a 6% thick airfoil at subcritical conditions in the same NACA family.

Although the code worked well for the inviscid cases attempted, there were some modifications and test cases which were required to make this code more valuable. For instance, since Streett found that the wake effects (wake displacement and curvature) were relatively important in the calculation of the lift distribution on a three dimensional wing,[20] presumably their inclusion in the design process would be important as well. This was investigated by utilizing the wake options in the code and and comparing their effect on the design of a wing. The logic necessary to include the viscous effects in the design process originally added by Gally was tested and modified where necessary.

Recently, a spanwise decoupling in the design regions which led to instabilities in the design solution was observed. The supposed source of this instability and the various methods used to combat this problem will be discussed later in the report.

One modification added to the program, which helps smooth out the rippling spanwise variations in the wing and give the designer added versatility, is an option where the user specifies pressure distributions at the edges of the design region and then the changes in the thicknesses of the airfoil sections calculated by the program for those stations are interpolated and added to the stations delimited by the edges. This approach is different from the original method where the target pressure distributions, not the change in thicknesses, were interpolated to the stations in the design region.

Since the designer is admonished in the TAWFIVE user's manual[25] that the wing is not modeled accurately enough to allow analysis of very low-aspect ratio wings and that grid problems may be encountered for wings which have high taper ratios or sweep angles, three wings of different aspect ratios and sweep angles will be used in the inverse design process to approximately delimit the range of geometries applicable to the present design code, TAW5D.

Because of the high computer costs associated with executing this program for fine computational grids, results will be shown which will reveal how fine the grid needs to be for satisfactory preliminary designs.

In summary, this thesis presents developments in the inverse design method. It includes a brief description of the analysis and design methods and techniques used to suppress a spanwise oscillation problem resulting from the interaction of the design method with the potential solver. In addition, it presents a series of test cases that reveal the lack of dependency of the design on the initial airfoil section, the importance of including viscous effects in wing design, and constraints due to aspect ratio, wing sweep, spanwise grid skewness. In addition, some questions about the necessary refinement of the grid and about any necessary constraints due to Mach-number-input-pressure-distribution compatibility will be answered.

CHAPTER II

DESCRIPTION OF TAWFIVE

As was stated in the introduction, the inverse-wing-design program, TAW5D, which was originally modified by Gally,[13–15] uses as its core the computer program TAWFIVE, which can be broken into three major sections: the inviscid, transonic, potential flow solver; the cylindrical/wind-tunnel type grid generation scheme; and the three dimensional, laminar and turbulent, integral boundary layer code included by Streett[20] which is based on the works of Smith[21], Stock[22] and Green.[26–28] Since the theory behind the code is spread across numerous references, an attempt will be made to summarize its formulation in a succinct fashion for the reader's convenience.

II.1 FLO-30

The transonic potential flow solver, FLO-30, [29–35] by Jameson and Caughey, is a finite volume method which solves the full potential equation in divergence form

$$(\rho u)_x + (\rho v)_y + (\rho w)_z = 0 \qquad (2-1)$$

transformed from Cartesian to curvilinear coordinates :

$$(\rho hU)_\xi - (\rho hV)_\eta + (\rho hW)_\zeta = 0 \qquad (2-2)$$

The derivation of the transformation of Eq. (2-2) is presented in Appendix A.

An expression for the local density, ρ, and the local speed of sound, a, nondimensionalized by the appropriate freestream quantities can be found by beginning with the energy equation

$$\frac{q_1^2}{2} + h_1 = \frac{q_2^2}{2} + h_2 \qquad (2-3)$$

where $q^2 = \left(u^2 + v^2 + w^2\right) q_\infty^2$

Then assuming the existence of a perfect gas such that

$$h = c_p T = \frac{a^2}{\gamma - 1} \tag{2-4}$$

the energy equation becomes

$$\frac{\gamma - 1}{2} q_1^2 + a_1^2 = \frac{\gamma - 1}{2} q_2^2 + a_2^2 \tag{2-5}$$

Next, assuming freestream and stagnation conditions such that

$$\begin{aligned} q_1 &= q_\infty \qquad & a_1 &= a_\infty \\ q_2 &= 0 \qquad & a_2 &= a_o \end{aligned} \tag{2-6}$$

and upon normalizing all the primitive variables by the appropriate freestream quantities

$$\begin{aligned} \bar{p} &= \frac{p}{\rho_\infty q_\infty^2} \qquad & \bar{\rho} &= \frac{\rho}{\rho_\infty} \\ \bar{a} &= \frac{a}{q_\infty} \qquad & \bar{T} &= \frac{T}{T_\infty} \end{aligned} \tag{2-7}$$

The bars on the nondimensionalized quantities will hereafter be omitted for convenience.

Eq. (2-5) becomes

$$a_o^2 = \frac{\gamma - 1}{2} + \frac{1}{M_\infty^2} \tag{2-8}$$

The local speed of sound is obtained using Eqs. (2-5) and (2-8), yielding

$$a^2 = a_o^2 - \left(\frac{q}{q_\infty}\right)^2 \left(\frac{\gamma - 1}{2}\right) \tag{2-9}$$

Using the isentropic relation

$$\frac{p}{p_\infty} = \rho^\gamma \tag{2-10}$$

and realizing that

$$p_\infty = \frac{1}{\gamma M_\infty^2} \qquad (2-11)$$

the isentropic relation becomes

$$p = \frac{\rho^\gamma}{\gamma M_\infty^2} \qquad (2-12)$$

Then making use of the speed of sound relation

$$a^2 = \frac{\gamma p}{\rho} \qquad (2-13)$$

a relation for density is found

$$\rho = (a M_\infty)^{\frac{2}{\gamma-1}} \qquad (2-14)$$

which for air can be simplified to

$$\rho = \left(\frac{a}{a_\infty}\right)^{\frac{2}{\gamma-1}} = \left(\frac{a}{a_\infty}\right)^5 \qquad (2-15)$$

This expansion is the actual form used in FLO-30, but the more familiar formula for density is shown in Eq. (2-16) and can be easily determined by substituting the speed of sound relation of Eq. (2-9) into Eq. (2-14).

$$\rho = \left[1 + \frac{\gamma - 1}{2} M_\infty^2 \left(1 - u^2 - v^2 - w^2\right)\right]^{\frac{1}{\gamma-1}} \qquad (2-16)$$

The nonconservative form of Eq. (2-1) shown in Eq. (2-17) can be determined by expanding the derivatives of Eq. (2-1); substituting in the appropriate derivatives of the density using the expression in Eq. (2-3); multiplying by $\frac{\rho}{a^2}$; and then implementing the equation of state for a perfect gas, the definition of the speed of sound; and finally defining the velocities in terms of a velocity potential, ϕ.

$$\begin{aligned}(a^2 - u^2)\,\phi_{xx} + (a^2 - v^2)\,\phi_{yy} + (a^2 - w^2)\,\phi_{zz}& \\ - 2uv\phi_{xy} - 2vw\phi_{yz} - 2uw\phi_{xz} &= 0\end{aligned} \qquad (2-17)$$

Both of these forms are valid for isentropic, irrotational flows of Mach numbers ranging from zero to transonic[25]; but, by using the conservative form of the potential equation, a finite difference scheme will result[36] which conserves mass, especially in areas containing large gradients such as with the flow through a shock. Although, nonconservative schemes have been successively implemented due in part to the fact that the effective mass production at the base of the shock wave fortuitously models the shock/boundary layer interactions, the best approach may be to use a conservative scheme with viscous corrections added by a separate boundary layer model[37]. This approach is the method utilized by TAWFIVE to include viscous effects.

FLO-30 uses a finite-volume type scheme which makes use of a staggered box approach. Its formulation is directly analagous to the control volume approach used to derive the original PDE in Eq. (2-1), except in the finite-volume scheme, the discrete nature of the finite difference model is considered from the onset by using a finite control volume in the neighborhood of a grid point in the finite-difference mesh[36]. This method is best illustrated by using it to discretize the following two-dimensional, incompressible version of Eq. (2-1) written in Cartesian coordinates

$$u_x + v_y = 0 \qquad (2-18)$$

With the aid of the two-dimensional box shown in Fig. 2, it can be seen that the staggered box scheme derives its name from the way in which the primary and secondary boxes interlock. The values of the potentials at the four grid points which

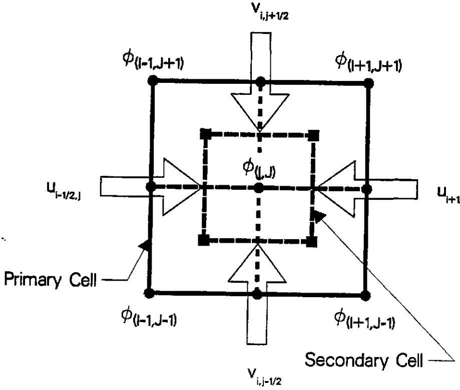

Fig. 2 Staggered box finite-volume cell

make up the corners of each primary box are used to calculate the velocities, u, v, in the following manner:

$$u = \phi_x = \mu_y \delta_x \phi$$
$$v = \phi_y = \mu_x \delta_y \phi \qquad (2-19)$$

where μ and δ are averaging and differentiating operators respectively and are defined by Jameson as

$$\mu_x f = \frac{1}{2}\left(f_{i+\frac{1}{2},j} + f_{i-\frac{1}{2},j}\right)$$
$$\delta_x f = f_{i+\frac{1}{2},j} - f_{i-\frac{1}{2},j} \qquad (2-20)$$

where it is assumed that $\Delta x = 1$. Therefore, the velocity, u, for instance, at the primary box center located at $(i+\frac{1}{2}, j+\frac{1}{2})$ is found by

$$u_{i+\frac{1}{2},j+\frac{1}{2}} = (\mu_y \delta_x \phi)_{i+\frac{1}{2},j+\frac{1}{2}} = \frac{(\phi_{i+1,j} - \phi_{i,j}) + (\phi_{i+1,j+1} - \phi_{i,j+1})}{2} \qquad (2-21)$$

The flux at the midpoint of each secondary box is determined by averaging the velocities u and v at the corners of that box in the y and x direction respectively; and the net flux into the secondary box at (i, j) is obtained, giving the discretized version of Eq. (2-18)

$$\mu_y \delta_x (u) + \mu_x \delta_y (v) = 0 \tag{2-22}$$

where for example

$$(\mu_y \delta_x u)_{i,j} = \frac{\left(u_{i+\frac{1}{2},j-\frac{1}{2}} - u_{i-\frac{1}{2},j-\frac{1}{2}} + u_{i+\frac{1}{2},j+\frac{1}{2}} - u_{i-\frac{1}{2},j+\frac{1}{2}}\right)}{2} \tag{2-23}$$

The previous discussion implicitly assumes that the velocity varies in a linear fashion between the primary cell centers so that the flux into the top of the secondary cell face would be, for instance:

$$\begin{aligned} \int_{x_{i-\frac{1}{2},j+\frac{1}{2}}}^{x_{i-\frac{1}{2},j+\frac{1}{2}}} v(x,y)dx \approx & \int_{x_{i-\frac{1}{2},j+\frac{1}{2}}}^{x_{i-\frac{1}{2},j+\frac{1}{2}}} \frac{v_{i-\frac{1}{2},j+\frac{1}{2}} - v_{i-\frac{1}{2},j+\frac{1}{2}}}{\Delta x} x - v_{i-\frac{1}{2},j-\frac{1}{2}} dx \\ =& \left(\frac{v_{i-\frac{1}{2},j+\frac{1}{2}} + v_{i+\frac{1}{2},j+\frac{1}{2}}}{2} \right) \end{aligned} \tag{2-24}$$

Jameson and Caughey found that this lumping of the fluxes at the primary cell centers reduced to a rotated Laplacian type difference scheme and hence to an uncoupling of the solution between adjacent grid points. Therefore, compensation terms were added which basically extrapolate the fluxes from the corners of the secondary cell to a distance, ϵ, towards the midpoint of each secondary cell face. Considering Fig. 3 and using an $\epsilon = .25$, the flux, u, at the corresponding grid location $(i + \frac{1}{2}, j + \frac{1}{4})$ is

$$u_{i+\frac{1}{2},j+\frac{1}{4}} = u_{i+\frac{1}{2},j+\frac{1}{2}} - .25 \left(\frac{\partial u}{\partial y}\right)_{i+\frac{1}{2},j+\frac{1}{2}} \tag{2-25}$$

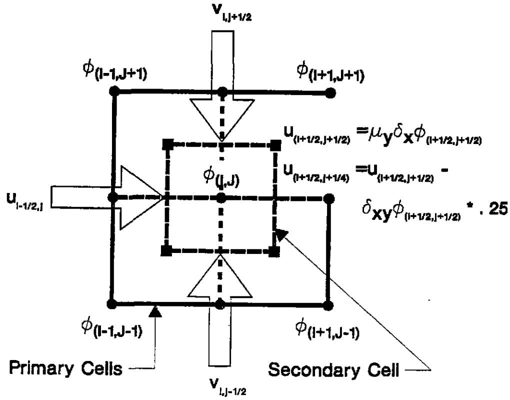

Fig. 3 Staggered box finite-volume cell with compensation terms defined

where

$$\left(\frac{\partial u}{\partial y}\right)_{i+\frac{1}{2},j+\frac{1}{2}} = \delta_{xy}(\phi)_{i+\frac{1}{2},j+\frac{1}{2}} \qquad (2-26)$$

When all the fluxes are extrapolated in this manner, the fluxes at the secondary cell centers become

$$\begin{aligned}
u_{i+\frac{1}{2},j} &= \frac{u_{i+\frac{1}{2},j-\frac{1}{2}} - \epsilon(\phi_{xy})_{i+\frac{1}{2},j+\frac{1}{2}} + u_{i-\frac{1}{2},j-\frac{1}{2}} + \epsilon(\phi_{xy})_{i-\frac{1}{2},j-\frac{1}{2}}}{2} \\
u_{i-\frac{1}{2},j} &= \frac{u_{i-\frac{1}{2},j-\frac{1}{2}} - \epsilon(\phi_{xy})_{i-\frac{1}{2},j+\frac{1}{2}} + u_{i-\frac{1}{2},j-\frac{1}{2}} + \epsilon(\phi_{xy})_{i-\frac{1}{2},j-\frac{1}{2}}}{2} \\
v_{i,j+\frac{1}{2}} &= \frac{v_{i+\frac{1}{2},j+\frac{1}{2}} - \epsilon(\phi_{xy})_{i+\frac{1}{2},j+\frac{1}{2}} + v_{i-\frac{1}{2},j+\frac{1}{2}} + \epsilon(\phi_{xy})_{i-\frac{1}{2},j+\frac{1}{2}}}{2} \\
v_{i,j-\frac{1}{2}} &= \frac{v_{i+\frac{1}{2},j-\frac{1}{2}} - \epsilon(\phi_{xy})_{i+\frac{1}{2},j-\frac{1}{2}} + v_{i-\frac{1}{2},j-\frac{1}{2}} + \epsilon(\phi_{xy})_{i-\frac{1}{2},j-\frac{1}{2}}}{2}
\end{aligned} \qquad (2-27)$$

When the net flux into the secondary box is accounted for, Eq. (2-22) becomes

$$\mu_y\delta_x u + \mu_x\delta_y v$$
$$-\epsilon\left((\phi_{xy})_{i+\frac{1}{2},j+\frac{1}{2}} - (\phi_{xy})_{i+\frac{1}{2},j-\frac{1}{2}} - (\phi_{xy})_{i-\frac{1}{2},j+\frac{1}{2}} + (\phi_{xy})_{i-\frac{1}{2},j-\frac{1}{2}}\right) = 0 \qquad (2-28)$$

which is equivalent to

$$\mu_{yy}\delta_{xx}\phi + \mu_{xx}\delta_{yy}\phi - \epsilon\delta_{xxyy}\phi = 0 \qquad (2-29)$$

(Typically, ϵ is .25)

Notice that the compensation terms lead to a fourth derivative of the potential; this higher order derivative will become important later in the discussion of a spanwise oscillation problem that occured in the design process.

The previous concepts can be extended to three dimensional compressible flow in curvilinear coordinates by considering eight primary boxes as shown in Fig. 4. The three-dimensional potential equation

$$(\rho hU)_\xi + (\rho hV)_\eta + (\rho hW)_\zeta = 0 \qquad (2-30)$$

is again descretized in the same way as in the two-dimensional case to give

$$\mu_{\eta\zeta}\delta_\xi(\rho hU) + \mu_{\zeta\xi}\delta_\eta(\rho hV) + \mu_{\xi\eta}\delta_\zeta(\rho hW) = 0 \qquad (2-31)$$

The same averaging scheme is used in this case except that the derivatives now have to be averaged in two of the coordinate directions instead of one. For example, $(\rho hW)_\zeta$ becomes:

$$(\mu_{\xi\eta}\delta_\zeta\rho hW)_{i,j,k} =$$
$$\frac{\left(\rho hW_{i+\frac{1}{2},j+\frac{1}{2},k-\frac{1}{2}} + \rho hW_{i+\frac{1}{2},j-\frac{1}{2},k-\frac{1}{2}} + \rho hW_{i-\frac{1}{2},j+\frac{1}{2},k-\frac{1}{2}} + \rho hW_{i-\frac{1}{2},j-\frac{1}{2},k-\frac{1}{2}}\right)}{4}$$
$$-\frac{\left(\rho hW_{i+\frac{1}{2},j+\frac{1}{2},k+\frac{1}{2}} + \rho hW_{i+\frac{1}{2},j-\frac{1}{2},k+\frac{1}{2}} + \rho hW_{i-\frac{1}{2},j+\frac{1}{2},k+\frac{1}{2}} + \rho hW_{i-\frac{1}{2},j-\frac{1}{2},k+\frac{1}{2}}\right)}{4}$$
$$(2-32)$$

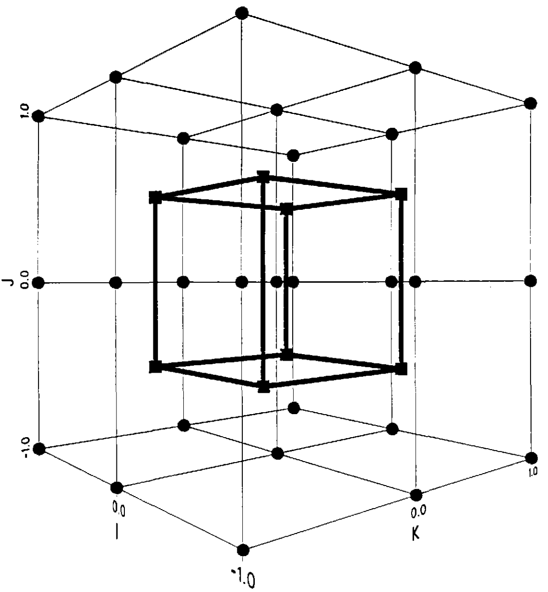

Fig. 4 Three dimensional staggered box finite-volume cell

Since relating the potential, ϕ, to the contravariant velocities, U, V, and, W may be somewhat unclear to the uninitiated, it is explained here for convenience. First, considering the the full potential function, Φ, defined as

$$\Phi = \phi + x\cos(\alpha) + y\sin(\alpha) \tag{2-33}$$

the standard chain rule can be applied to it to give u, v and, w as follows:

$$\begin{aligned} u &= \frac{\partial \Phi}{\partial x} = \frac{\partial \phi}{\partial \xi}\frac{\partial \xi}{\partial x} + \frac{\partial \phi}{\partial \eta}\frac{\partial \eta}{\partial x} + \frac{\partial \phi}{\partial \zeta}\frac{\partial \zeta}{\partial x} + \cos\alpha \\ v &= \frac{\partial \Phi}{\partial y} = \frac{\partial \phi}{\partial \xi}\frac{\partial \xi}{\partial y} + \frac{\partial \phi}{\partial \eta}\frac{\partial \eta}{\partial y} + \frac{\partial \phi}{\partial \zeta}\frac{\partial \zeta}{\partial y} + \sin\alpha \\ w &= \frac{\partial \Phi}{\partial z} = \frac{\partial \phi}{\partial \xi}\frac{\partial \xi}{\partial z} + \frac{\partial \phi}{\partial \eta}\frac{\partial \eta}{\partial z} + \frac{\partial \phi}{\partial \zeta}\frac{\partial \zeta}{\partial z} \end{aligned} \tag{2-34}$$

Defining

$$[J] = \begin{pmatrix} \xi_x & \eta_x & \zeta_x \\ \xi_y & \eta_y & \zeta_y \\ \xi_z & \eta_z & \zeta_z \end{pmatrix} \tag{2-35}$$

and realizing that

$$[J] = \left[\mathbf{H}^T\right]^{-1} \tag{2-36}$$

where $\mathbf{H}$ is the transformation matrix defined by

$$\mathbf{H} = \begin{pmatrix} x_\xi & x_\eta & x_\zeta \\ y_\xi & y_\eta & y_\zeta \\ z_\xi & z_\eta & z_\zeta \end{pmatrix} \qquad \text{with} \qquad h = |\mathbf{H}| \tag{2-37}$$

the physical velocities, u, v, w normalized by q_∞ can be related to the gradient of the reduced potential function, ϕ, by

$$\begin{pmatrix} u \\ v \\ w \end{pmatrix} = \left[\mathbf{H}^T\right]^{-1} \begin{pmatrix} \phi_\xi \\ \phi_\eta \\ \phi_\zeta \end{pmatrix} + \begin{pmatrix} \cos\alpha \\ \sin\alpha \\ 0 \end{pmatrix} \tag{2-38}$$

Note that since the grid point coordinate locations in the physical space, $(x,\ y,\ z)$, are generated as functions of $(\xi,\ \eta,\ \zeta)$, it is convenient to use $\mathbf{H}$ instead of $\mathbf{J}$ explicitly.

The contravariant velocities U, V, W, whose directions lie along the corresponding ξ, η, ζ grid lines are related to the physical velocities by :

$$\begin{pmatrix} U \\ V \\ W \end{pmatrix} = \mathbf{H}^{-1} \begin{pmatrix} u \\ v \\ w \end{pmatrix} \qquad (2-39)$$

and the derivatives of the potentials and the metrics are defined as:

$$\begin{aligned} \phi_\xi &= \mu_{\eta\zeta}\delta_\xi(\phi) \qquad & x_\xi &= \mu_{\eta\zeta}\delta_\xi(x) \\ \phi_\eta &= \mu_{\zeta\xi}\delta_\eta(\phi) \qquad & y_\xi &= \mu_{\eta\zeta}\delta_\xi(y) \\ \phi_\zeta &= \mu_{\xi\eta}\delta_\zeta(\phi) \qquad & z_\xi &= \mu_{\eta\zeta}\delta_\xi(z) \end{aligned} \qquad (2-40)$$

The density, ρ, and Jacobian, h, are evaluated at the centers of the of their respective primary cell centers. Again, by lumping the fluxes at the corners of the secondary cell's corners, the solution is decoupled on odd and even grid points leading to two independent solutions. This problem is remedied with compensation terms which again move the evaluation location of the fluxes to a point somewhere in between the corner and the midpoint of the secondary cell face. When this procedure is performed for all the cell faces, the potential equation takes on the form of

$$\begin{aligned} &\mu_{\eta\zeta}\delta_\xi(\rho h U) + \mu_{\zeta\xi}\delta_\eta(\rho h V) + \mu_{\xi\eta}\delta_\zeta(\rho h W) \\ &\quad - \epsilon\left(\mu_\zeta\delta_{\xi\eta}Q_{\xi\eta} + \mu_\xi\delta_{\eta\zeta}Q_{\eta\zeta} + \mu_\eta\delta_{\zeta\xi}Q_{\zeta\xi} - \frac{1}{2}\delta_{\xi\eta\zeta}Q_{\xi\eta\zeta}\right) = 0 \end{aligned} \qquad (2-41)$$

where the Q's are the compensation terms defined by Jameson as :

$$\begin{aligned} Q_{\xi\eta} &= (A_\xi + A_\eta)\,\mu_\zeta\delta_{\xi\eta}\phi \\ Q_{\eta\zeta} &= (A_\eta + A_\zeta)\,\mu_\xi\delta_{\eta\zeta}\phi \\ Q_{\zeta\xi} &= (A_\zeta + A_\xi)\,\mu_\eta\delta_{\zeta\xi}\phi \\ Q_{\xi\eta\zeta} &= (A_\xi + A_\eta + A_\zeta)\,\delta_{\xi\eta\zeta}\phi \end{aligned} \qquad (2-42)$$

Here, A_ξ, A_η, A_ζ are the influence coefficients which compensate for the dependence of ρ on ϕ_ξ, ϕ_η, and ϕ_ζ. These terms end up being the coefficients of of $\phi_{\xi\xi}$, $\phi_{\eta\eta}$ and $\phi_{\zeta\zeta}$ in the expanded form of Eq. (2-30)[35].

Since the formation of entropy through a shock wave has been neglected through the use of the potential function, artificial viscosity must be added to eliminate the physically unrealistic solutions. In general, if central differences are used throughout the flow field, it is possible for the solution to predict discontinuous expansion shocks followed by compression shocks. This situation is a case where entropy decreases which is a physical impossibility, and is remedied by adding Jameson's[30,31] P, Q, and R terms which provide the necessary artificial viscosity by producing an upwind bias in the supersonic zones. The form of these terms can be found by formulating the potential equation in streamline coordinates which reveals the true zone of dependence in the supersonic zones. Then in these supersonic zones, the second derivatives of the potential, ϕ, included in the streamwise term are formulated with upstream or backward differences while the second derivatives included in the crossflow term are differenced centrally[29]. As shown in the final form of the following finite volume equation, the terms are formulated in such a way as to maintain the conservative form of the potential equation.

$$\begin{aligned}&\mu_{\eta\zeta}\delta_\xi(\rho hU + P) + \mu_{\zeta\xi}\delta_\eta(\rho hV + Q) + \mu_{\xi\eta}\delta_\zeta(\rho hW + R)\\ &\quad - \epsilon\left(\mu_\zeta\delta_{\xi\eta}Q_{\xi\eta} - \mu_\xi\delta_{\eta\zeta}Q_{\eta\zeta} + \mu_\eta\delta_{\zeta\xi}Q_{\zeta\xi} - \frac{\delta_{\xi\eta\zeta}Q_{\xi\eta\zeta}}{2}\right) = 0\end{aligned} \tag{2-43}$$

This numerical equation is then embedded into an artificial time dependent equation

$$\begin{aligned}&\frac{\partial}{\partial\xi}(\rho hU + P) + \frac{\partial}{\partial\eta}(\rho hV + Q) + \frac{\partial}{\partial\zeta}(\rho hW + R)\\ &\quad + \text{compensation terms} = \alpha\phi_{\xi T} + \beta\phi_{\eta T} + \gamma\phi_{\zeta T} + \delta\phi_T\end{aligned} \tag{2-44}$$

and solved via a successive line overrelaxation (SLOR) scheme which sweeps in the ξ direction along constant ζ surfaces starting at the root of the wing and implicitly solves for the potentials in the η direction. Equation (2-43) is a direct statement of the conservation of mass and should approach zero as the solution converges.

After obtaining a solution on a coarse grid, grid halving is used so that the finer grid has a better initial approximate solution, thus speeding up the convergence of the solution.

II.2 Grid Geometry

The computational grid used by the potential solver, FLO-30, is a body-fitted, curvilinear mesh which can be wrapped around a generalized wing-fuselage combination that is symmetric about the x-z plane. A body-fitted grid system is desirable in a full-potential scheme when the boundary conditions are applied at the actual surface of the airfoil. With a body-fitted grid, no interpolation is required and the boundary conditions are easily and accurately applied. Because of the shape the grid system resembles, it is called a wind-tunnel type grid. An example of this grid is portrayed in Fig. 5. The grid shown is the coarsest mesh and has 40 x 6 x 8 points in the ξ, η, and ζ directions respectively. With this grid, the wing becomes a constant η surface, and each cylindrical looking shell is a constant ζ surface. Constant ξ lines can be seen running spanwise on the wing at constant chord fractions from the leading edge. Notice also that due to the conformal transformation used[32,34] constant ξ lines are packed close to the leading edge of the wing. This clustering is an attractive feature when designing airfoil sections using the direct-inverse approach. Moreover, constant

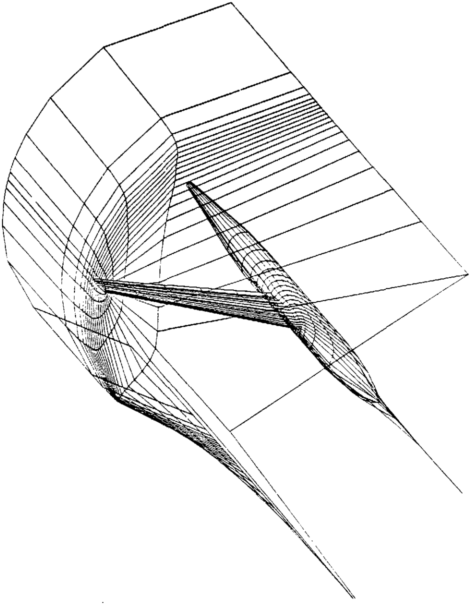

Fig. 5 Conformal grid topography

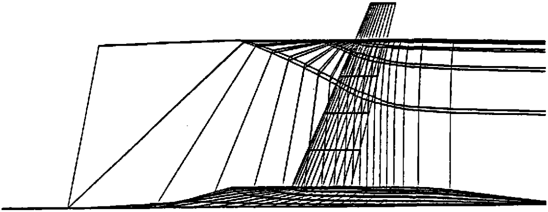

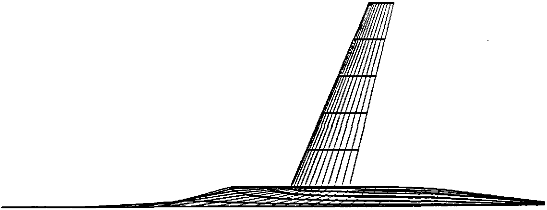

Fig. 5 Continued

ζ lines are spaced evenly on the wing and, on the finest mesh, give the designer up to 21 spanwise stations where the pressure distributions can be specified. As can be also seen from the figure, the lines of constant ξ and η are nearly orthogonal on the constant ζ surface[34] shown at the wing tip of the airplane, while lines of constant ξ and ζ on surfaces of constant η, such as the wing, are not orthogonal except, of course, for cases where the wing has no sweep or taper. The lines of constant ζ leaving the surface of the wing are nearly orthogonal to the surface; this fact will be important later on in the discussion of the wing-design methodology.

The computational grid system is created using a series of analytically-defined algebraic, conformal, and shearing transformations to transform the the wing-fuselage combination and surrounding flowfield in the physical space to a box in the computational space shown in Fig. 6. Following Caughey[34], the polar coordinates r and θ are defined in the crossflow planes as

$$r = \left(y^2 + z^2\right)^{\frac{1}{2}} \tag{2-45}$$

$$\theta = \tan^{-1}\left(\frac{y}{z}\right) \tag{2-46}$$

The fuselage surface, which is symmetric about the x-y plane, is defined by $r = R_f(x,\theta)$. All points in the flowfield are then referenced to the surface of the fuselage at the same x and θ location and normalized by the distance between radius, R_t, of the cylindrical surface passing through the wing tip and the radius of the fuselage, R_f at the given x and θ location :

$$\bar{r} = \frac{\left[r - R_f(x,\theta)\right]}{\left[R_t - R_f(x,\theta)\right]} \tag{2-47}$$

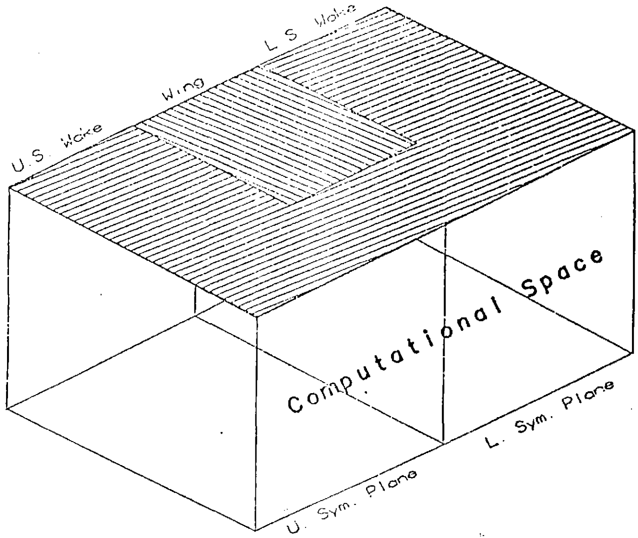

Fig. 6 The computational domain [25]

This normalization causes the lines of constant $\bar{r}$, or equivalently k, on the surface of the wing to be curved in the x-z plane so they will not coincide exactly with the chord line of the airfoil section. This procedure also maps the fuselage to a slit in the computational domain. This type of normalization allows for high, low, and mid-wing configurations.

The function $R_f(x, \theta)$ is found through a Fourier decomposition of the user-defined fuselage cross sections such that

$$R_f(x_i, \theta) = \sum_{j=1}^{m} a_{ij} \cos j(\theta + \frac{\pi}{2}) \qquad (2-48)$$

The coefficients, a_{ij}, which are assumed to be continuous functions of x, are spline fitted in the x direction for each j. The required radius of the fuselage can be found for any point on the wing, or in the flowfield, by interpolating these coefficients to the desired x.

A singular point is located at the focus of a parabola which is fit to the leading edge of each wing section with a least squares curve fit. The wing sweep, taper and dihedral are accounted for by referencing the coordinates in each surface of constant $\bar{r}$ to the location of the singular line, which is the locus of points comprising the singular points, $x_s(\bar{r})$, $\theta_s(\bar{r})$ at the leading edge of the wing.

$$\bar{x} = \frac{(x - x_s(\bar{r}))}{c(\bar{r})} + log(2) \qquad (2-49)$$

$$\bar{\theta} = 2 \left(\frac{\theta - \left(1 - 4\frac{\theta^2}{\pi^2}\theta_s(\bar{r})\right)}{\left(1 - 4\frac{\theta_s^2(\bar{r})}{\pi^2}\right)} \right) \qquad (2-50)$$

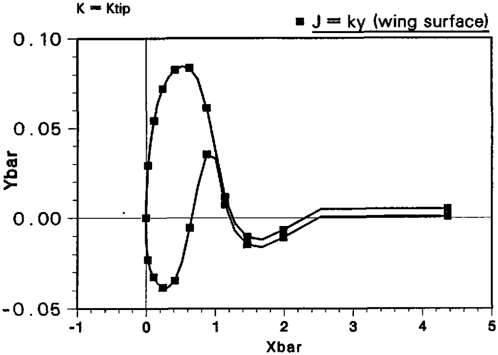

Fig. 7 Section surface and wake representation at a constant $\bar{r}$ station in the normalized plane

This normalization effectively maps the wing's planform to a rectangle in the computational space. The θ coordinates of the wing corresponding to the given $\bar{r}$ and x are found by linearly interpolating the coordinates of the airfoil sections at input stations defining the wing in the spanwise direction. Then at the intersection of a surface of constant $\bar{r}$ with the wing's surface shown in Fig. 7, the wing section and the wake is transformed into a bump in the conformally mapped plane, as shown in Fig. 8, with the inverse of the conformal transformation

$$\bar{x} + i\bar{\theta} = log\left[1 - \cosh\left(\xi' + i\eta'\right)\right] \tag{2-51}$$

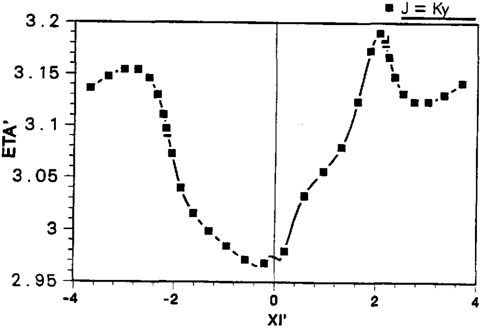

Fig. 8 Section surface and wake representation at a constant $\bar{r}$ station in the auxiliary plane

Fig. 9 reveals an entire constant $\bar{r}$ surface in the auxiliary plane. A function $S(\xi', \bar{r})$ is defined to be the η' coordinate corresponding to the wing's surface defined by the input geometry at a constant $\bar{r}$.

The η' coordinate is sheared out with a simple normalization according to

$$\xi = \xi', \quad \eta = \eta'/S(\xi', \bar{r}), \quad \zeta = \bar{r} \tag{2-52}$$

so that the wing surface lies on a coordinate line in a nearly orthogonal coordinate system of $\zeta = const.$

Next, the spacing of the coordinate points in the physical domain is controlled by introducing a Cartesian grid into the ξ, η, ζ computational domain where

$$-\xi_{lim} \leq \xi \leq \xi_{lim}, \quad 0 \leq \eta \leq 1, \quad 0 \leq \zeta \leq \zeta_{lim} \tag{2-53}$$

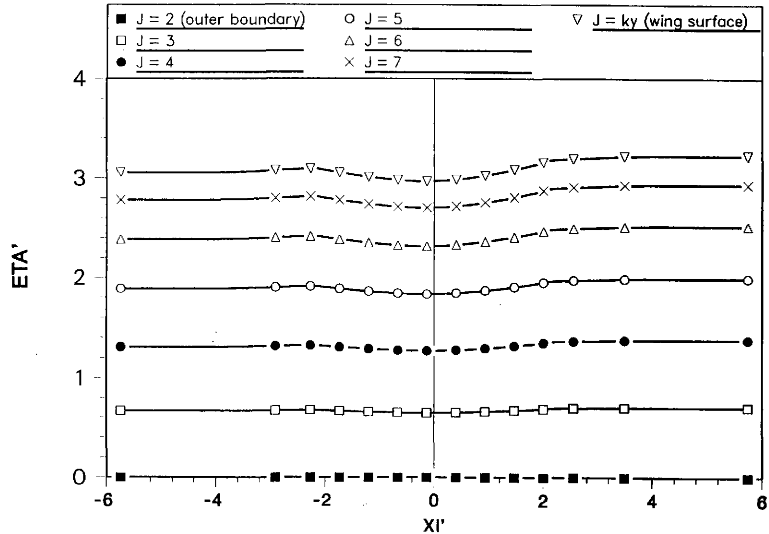

Fig. 9 Constant $\bar{r}$ surface in the auxiliary plane

Since the derivatives of the spatial coordinates needed for the transformation metrics are evaluated numerically, stretching to infinity is impossible; thus the computational domain is truncated a finite distance away from the airplane. The outer limits of ξ and ζ are chosen such that the grid stretches out far enough from the wing-fuselage so that freestream boundary conditions can be safely applied. These constants are not user specified, but rather are hard coded in Subroutine COOR of TAWFIVE, such that the distance of the outer boundary from the fuselage is about 3 wing spans. This distance is probably more than sufficient for most applications; but if a low aspect ratio wing is used, which has a large powerful potential vortex at the wing tip and significant amounts of spanwise flow, the aerodynamicist may want to increase the outer boundary distance.

The ξ, η and, ζ functions for a coarse grid (40x6x8) are shown in Figs. 10-12. Notice that distribution of ξ between grid points 8 and 24, which corresponds to the upper and lower trailing edges respectively, in this domain varies linearly and evenly on the wing and then varies quite quickly into the wake ending at a downstream location where the flowfield is assumed to be nonchanging. The ζ stretching function has the same form, but of course the outer limit at $K = 12$ determines the outer, radial boundary where the freestream conditions are imposed, which in this case, as mentioned earlier, will be about 3 wing spans. The η stretching function varies in a parabolic fashion from the wing's surface at $J = 14$. Although this stretching does seem to pack grid points close to the surface of the wing, since η is basically an angular ordinate, the grid spacing above the wing becomes greater as one proceeds

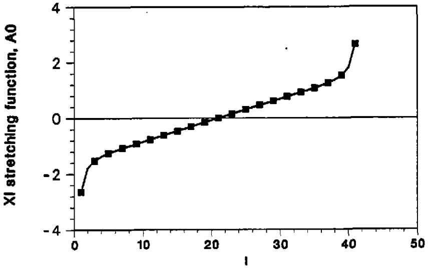

Fig. 10 Stretching function for the ξ (I) direction

towards the tip. This increase means that the resolution at the tip region is much less than that at the root, but this is countered later with a radial correction so that the grid spacing immediately above the wing is essentially constant for every spanwise station.

Once the function $S(\xi', \bar{r})$ has been linearly interpolated to the new ξ coordinates, the physical coordinates of the grid system can be found through the reverse procedure. First, ξ', η', and $\bar{r}$ are found using Eq. (2-52). Then Eq. (2-51) is used to extract $\bar{x}$ and $\bar{\theta}$. But before this operation is performed, $\bar{x}$ and $\bar{\theta}$ have to be

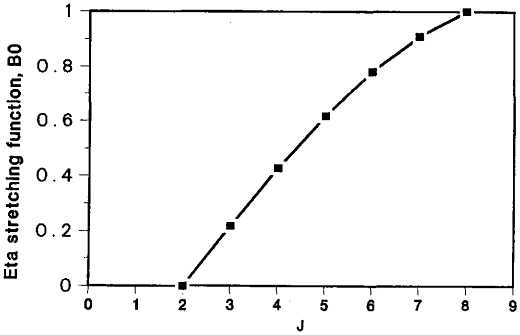

Fig. 11 Stretching function for the η (J) direction

separated in Eq. (2-51). First, both sides are exponentiated and the definition of the hyperbolic cosine is used so that Eq. (2-51) becomes

$$e^{\bar{x}}e^{i\bar{\theta}} = 1 - \frac{1}{2}\left(e^{\xi'}e^{i\eta'} + e^{-\xi'}e^{-i\eta'}\right) \quad (2-54)$$

Using Euler's identity,

$$e^{iz} = \cos(z) + i\sin(z) \quad (2-55)$$

rearranging, and separating imaginary and real parts, gives

$$e^{\bar{x}}\cos\bar{\theta} = 1 - \frac{1}{2}\cos\eta'\left(e^{\xi'} + e^{-\xi'}\right) \quad (2-56)$$

$$e^{\bar{x}}\sin\bar{\theta} = -\frac{1}{2}\sin\eta'\left(e^{\xi'} - e^{-\xi'}\right) \quad (2-57)$$

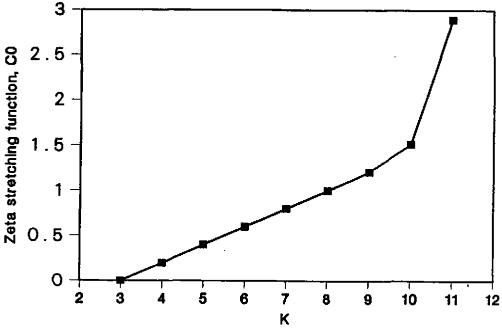

Fig. 12 Stretching function for the ζ (K) direction

Dividing these two equations by each other and solving for $\bar{\theta}$ explicitly yields

$$\bar{\theta} = \tan^{-1}\left[\frac{-\sin\eta'\sinh\xi'}{1-\cos\eta'\cosh\xi'}\right] \qquad (2-58)$$

Next $\bar{x}$ is found explicitly by first using a trigonometric identity and Eq. (2-58) to generate

$$\sin\bar{\theta} = \frac{-\sin\eta'\sinh\xi'}{\sqrt{(1-\cos\eta'\cosh\xi')^2+\sin\eta'\sinh^2\xi'}} \qquad (2-59)$$

Substituting this into Eq. (2-57) and performing some algebra gives

$$\bar{x} = ln\left(\cosh\xi' - \cos\eta'\right) \qquad (2-60)$$

So given ξ' and η' from the previous steps, the normalized coordinates $\bar{x}$ and $\bar{\theta}$ are obtained for all the grid points in the domain. At this time, two more special stretching functions are introduced. One function is used to further stretch $\bar{x}$ downstream

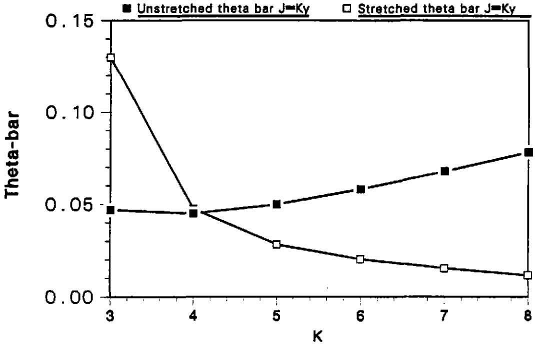

Fig. 13 Comparison between stretched and unstretched $\bar{\theta}$

of the wing and another scales $\bar{\theta}$ such that nearly constant grid spacing is achieved immediately above the wing from the root to the outer boundary. The effects of the stretching functions can be seen in Fig. 13.

Notice that this conformal transformation packs grid lines at the leading edge of the wing where the gradients are large. This clustering is an attractive feature for the inverse design procedure. However, it is paired with the disadvantage that the chordwise grid spacing is large at the trailing edge where high resolution is needed to accurately satisfy the Kutta condition and to resolve trailing edge pressures accurately especially with those generated by aft cambered airfoils.

Equations (2-49) and (2-50) are inverted to give x and θ and then Eq. (2-47) is inverted to yield r for a given x and θ. This last step requires extensive interpolation to find the radius of the fuselage, $R_f(x,\theta)$, for all of the grid points. Then Eqs. (2-45) and (2-46) are used to find the physical coordinates y and z of the grid. Finally, coordinates of the points located in 'ghost' surfaces are obtained through simple linear extrapolation of the adjacent grid points along the appropriate ξ, η or, ζ grid line.

II.3 Boundary Conditions

There are a number of boundary conditions which must be applied to the mathematical model of the physical flow about the wing-body. These include flow tangency on the wing, fuselage, and the symmetry plane; appropriate far-field boundary conditions at the finite limits of the computational domain; the Kutta condition at the trailing edge of the lifting wing; appropriate treatment of the wake; and the computational slit outboard of the wing tip.

II.3.1 Flow tangency

The flow tangency condition is easily implemented due to the curvilinear system. The fluxes above the surface need only be reflected to the ghost points beneath it so that the net out of plane component of the flux vanishes at the surface. In the case of the wing this becomes

$$\begin{aligned} \rho hU_{i,ky+\frac{1}{2},k} &= \rho hU_{i,ky-\frac{1}{2},k} \\ \rho hV_{i,ky-\frac{1}{2},k} &= -\rho hV_{i,ky-\frac{1}{2},k} \qquad \text{where: } ky = j_{wing} \qquad (2-61) \\ \rho hW_{i,ky+\frac{1}{2},k} &= \rho hW_{i,ky-\frac{1}{2},k} \end{aligned}$$

Similarly for the symmetry plane

$$\begin{aligned} \rho hU_{i,1\frac{1}{2},k} &= \rho hU_{i,2\frac{1}{2},k} \\ \rho hV_{i,1\frac{1}{2},k} &= -\rho hV_{i,2\frac{1}{2},k} \qquad \text{where: } j = 2 \text{ on the symmetry plane} \qquad (2-62) \\ \rho hW_{i,1\frac{1}{2},k} &= \rho hW_{i,2\frac{1}{2},k} \end{aligned}$$

While for the fuselage this becomes

$$\begin{aligned} \rho h U_{i,j,2\frac{1}{2}} &= \rho h U_{i,j,3\frac{1}{2}} \\ \rho h V_{i,j,2\frac{1}{2}} &= \rho h V_{i,j,3\frac{1}{2}} \qquad \text{where: } k = 3 \text{ on the fuselage} \qquad (2-63) \\ \rho h W_{i,j,2\frac{1}{2}} &= -\rho h W_{i,j,3\frac{1}{2}} \end{aligned}$$

The previously discussed compensation terms and upwinding terms are also similarly reflected in an appropriate manner.

Potentials at the ghost points located at grid points beneath the surfaces are needed for the calculation of surface velocities used in the upwinding terms and the surface pressures. These are found for the wing and fuselage by setting the appropriate contravariant velocity to zero in

$$\begin{pmatrix} U \\ V \\ W \end{pmatrix} = \left[\mathbf{H}^T\mathbf{H}\right]^{-1} \begin{pmatrix} \phi_\xi \\ \phi_\eta \\ \phi_\zeta \end{pmatrix} + \mathbf{H}^{-1} \begin{pmatrix} \cos\alpha \\ \sin\alpha \\ 0 \end{pmatrix} \qquad (2-64)$$

and using the resulting equation to solve for the unknown potential at the ghost point. In the case of the fuselage, this method of defining the ghost points is used solely when they are needed in the calculation of the upwinding terms in the residual expression. When the pressures are calculated, the ghost points are defined by assuming

$$\phi_{\zeta\zeta} = 0 \qquad (2-65)$$

so that the potential at the ghost point is, in effect, linearly extrapolated in the spanwise direction. As seen in Fig. 14, these two methods lead to quite different values. The first leads to a discontinuous spanwise variation in the potential while the second has a much smoother variation. The first approach guarantees that the flow will be tangent at the fuselage, while the second does not. However, the pressures calculated

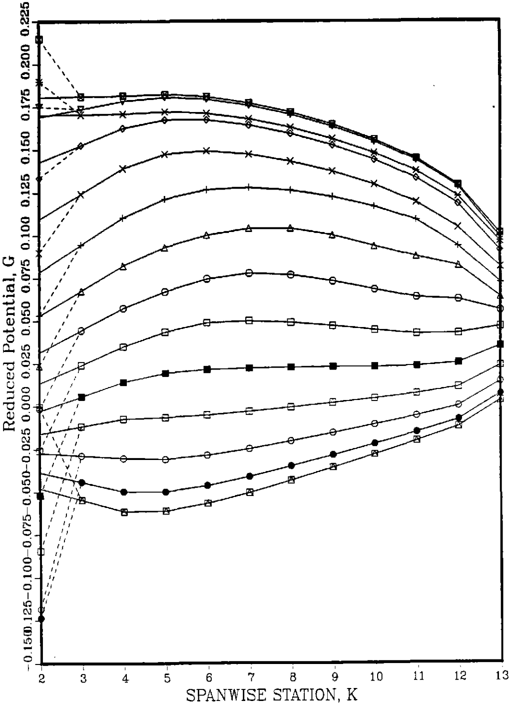

Fig. 14 Comparison between the ghost-point potentials defined with flow tangency (dashed lines) and extrapolation (solid lines)

at the root are fairly independent of the method used to define the potentials at the ghost points in the fuselage.

The potentials at the ghost points of the symmetry plane are similarly calculated by assuming

$$\phi_{\eta\eta} = 0 \qquad (2-66)$$

This process imposes an inflexion point on the pertubation velocity in the η direction at the symmetry plane since only symmetrical cases are treated. It is uncertain why ϕ_η was not set to zero instead to approximate tangency at the plane of symmetry. However, this situation is rather academic since these ghost points are used only for supersonic regions adjacent to the symmetry plane to compute the small spanwise upwinding term.

II.3.2 Far-field boundary conditions

Since the reduced potential used in the formulation of the numerical method represents a pertubation from the freestream value, they are set explicitly to zero on the radial boundary. ζ_{max}, and the upstream boundary represented by part of the minimum η surface.

At the outflow boundary, ($\xi = \xi_{min,max}$), the streamwise pertubation velocity, ϕ_ξ is set to zero. This latter condition implies that the pressure will return to its freestream value, assuming that there is not any crossflow[34].

II.3.3 Wake treatment

In the original method of FLO-30, the wake is treated as a vortex sheet which has a discontinuous jump in the tangential velocity and a continuous normal velocity through the sheet. The rolling up of the sheet is ignored and the vertical convection of the sheet is approximated by assuming that the wake lies along the constant η grid line that leaves the trailing edge smoothly and returns to the plane of the wing at the outflow boundary. The requirement that the normal velocity be continuous is enforced by setting $V_\eta = 0$ on the wake, which fixes the values of the potentials at the ghost points, and the jump in the tangential velocity is satisfied by forcing a constant jump in potentials on the the surface of the sheet along a constant ζ and η line. This jump in potential is obtained using the circulation determined at the trailing edge of the wing.

II.3.4 Outboard computational slit

Due to the C-grid type formation of the grid, there exists a computational slit outboard of the wing tip on the plane of the wing. Since physically the pressure must be continuous across this cut, the potentials on the surface and at the corresponding ghost points are defined such that the reduced velocities normal and tangential to to the surface are continuous across the slit.

II.4 Boundary Layer Scheme

II.4.1 Integral method

Streett[20] included an integral boundary layer scheme in TAWFIVE to account for the necessary viscous effects in the form of the boundary layer displacement thickness, wake curvature and wake thickness. An integral method was chosen for its computational efficiency and its relative robustness.

In an integral approach the degree of the partial differential equations is reduced by an *a priori* integration in the direction normal to the surface.[21] This reduction can be illustrated by considering the boundary layer equations governing a two dimensional incompressible flow[19]:

$$\frac{\partial u}{\partial x} + \frac{\partial v}{\partial y} = 0 \qquad (2-67)$$

$$u\frac{\partial u}{\partial x} + v\frac{\partial u}{\partial y} = \mathrm{U}\frac{d\mathrm{U}}{dx} + \nu\frac{\partial^2 u}{\partial y^2} \qquad (2-68)$$

If Eq. (2-68) is integrated with respect to y from the wall ($y = 0$) to a distance h outside the boundary layer, it becomes

$$\int_{y=0}^{h}(u\frac{\partial u}{\partial x} + v\frac{\partial u}{\partial y} - \mathrm{U}\frac{d\mathrm{U}}{dx})dy = \frac{\tau_o}{\rho} \qquad (2-69)$$

where τ_o is the shearing stress at the wall.

Using the continuity equation, Eq. (2-67), to obtain the normal velocity component, v, as

$$v = -\int_0^y(\frac{\partial u}{\partial x})dy \qquad (2-70)$$

and substituting this result into Eq. (2-69), the result is

$$\int_{y=0}^{h}(u\frac{\partial u}{\partial x} - \frac{\partial u}{\partial y}\int_0^y\frac{\partial u}{\partial x}dy - \mathrm{U}\frac{d\mathrm{U}}{dx})dy = -\frac{\tau_o}{\rho} \qquad (2-71)$$

After integrating by parts and reducing, Eq. (2-71) becomes

$$\int_0^h\frac{\partial}{\partial x}[u(\mathrm{U}-u)]\,dy + \frac{d\mathrm{U}}{dx}\int_0^h(\mathrm{U}-u)\,dy = \frac{\tau_o}{\rho} \qquad (2-72)$$

Now, taking $h \to \infty$ and defining a displacement thickness, δ_1^*, and a momentum thickness, θ as

$$\begin{aligned}\delta_1^*\mathrm{U} &= \int_{y=0}^{\infty}(\mathrm{U}-u)dy \\ \theta\mathrm{U}^2 &= \int_{y=0}^{\infty}u(\mathrm{U}-u)dy\end{aligned} \qquad (2-73)$$

and substituting them into Eq. 2-72, it becomes

$$\frac{d}{dx}(\mathrm{U}^2\theta) + \delta_1^*\mathrm{U}\frac{d\mathrm{U}}{dx} = \frac{\tau_o}{\rho} \qquad (2-74)$$

In this reduction process, two partial differential equations have been replaced by one ordinary differential equation. Since only the integrated quantities, δ^* and θ, are really the only quantities required of the boundary routine to model the weak viscous interaction, the fact that the solution to this equation does not provide the exact local variation of primitive flow properties across the boundary layer is not of consequence. The required functional form of the variation in u across the boundary layer is assumed *a priori*–by a polynomial for instance.

II.4.2 Laminar scheme

In three-dimensional, compressible, laminar flow the same integration procedure is implemented using two bounday-layer momentum equations and their corresponding moment of momentum relations to yield a system of four coupled partial-differential equations.[20] In the formulation of these equations, it is assumed that the streamwise velocity profile is of the Faulker-Skan (F-S) family of similarity profiles and that the cross flow profile is a linear combination of the F-S family of profiles. These incompressible profiles are extended to compressible flow by the scaling of the normal coordinate with the Stewartson transformation.

II.4.3 Turbulent scheme

The formulation of the turbulent scheme is similar to the laminar, but the streamwise velocity is assumed to have a simple power-law profile which is a function of the streamwise shape factor and the transformed boundary layer thickness and normal coordinate; and, the cross flow profile has the form of

$$\frac{v}{U} = \frac{u}{U}(1 - \frac{Z}{\Delta})^2 \tan\beta \qquad (2-75)$$

where Z is the transformed normal coordinate, Δ is the transformed boundary layer displacement thickness, and β is the angle between the external streamline of the potential flow and the wall shear direction. In the turbulent scheme, the final three governing equations are two momentum integral equations derived from the continuity and boundary layer momentum equations and one entrainment equation. The latter equation accounts for the addition of mass into the boundary layer from the surrounding flow as the boundary layer grows.

II.4.4 Lag entrainment

Originally, in the work by Smith[21], the relationship between the entrainment coefficient and the shape factor required in the previous scheme was formulated empirically with a simple algebraic equation. Later Green found a relationship for the required quantities through the use of the turbulent kinetic energy equation which explicitly represents the balance between production, advection, diffusion and dissipation of turbulent energy in the boundary layer. He referred to this as the Lag-Entrainment method[27].

Also, in Green's method the desired momentum and displacement thickness of the wake is determined by simply continuing the integration of the three governing equations past the trailing edge on either side of the wake. It is assumed that aft of the trailing edge that the skin friction coefficient is zero and that the dissipation length scale is twice that on the wing. Once the integration is performed on either side of the wake, the required integral properties are simply the sum of those calculated on both sides.

II.4.5 Solution of the governing equations

The resulting governing equations are solved through an explicit type integration scheme in the x (or chordwise direction) along constant span stations. In this scheme, the domain of dependence is conservatively assumed to lie between the external streamline of the potential flow and the shear angle of the boundary layer. To account for this dependency, the spanwise derivatives found in the governing equations are backward differenced if the external streamline and the wall shear line lie on the outboard side of the chordline and central differenced if the streamline and the shear line lie on opposite sides of the chordline.

Boundary conditions are required at all inflow boundaries. At the root, a plane of symmetry is assumed. Here, the cross flow velocity is set to zero, as are all all spanwise derivatives. At the wing tip, all spanwise derivatives are also set equal to zero. And finally, an attachment line approach[38] is used to determine the initial conditions at the leading edge.

II.4.6 Wake curvature

When the flow leaves the wing at the trailing edge, it initially follows a curved path and then soon aligns itself with the freestream downstream of the wing. This large curvature of the flow near the trailing edge can have a measurable effect on the overall lift of the wing. In fact, Streett found that in one instance the sectional lift coefficient near the tip of the wing was decreased by about four percent when the curvature of the wake was taken into account. Usually, if only first order effects are considered, the pressures at the trailing edge would be equal on the upper and lower surface. But, if the wake is considered to have an effective thickness of $\delta^* + \theta$ due to viscous effects and curvature, the pressures on either side of the wake will not be equal except at the centerline of the wake. Since the flowfield about the wing and the wake with the displacement thickness added to it is modeled inviscidly, the trick is to calculate a pressure difference across the wake at the trailing edge in the inviscid flow which will yield a zero pressure difference at the centerline of the wake in the real viscous flow[39]. It has been shown that the appropriate pressure jump across the wake with a thickness of δ^* can be written as a function of the curvature, κ_w, of the centerline of the actual wake, the mean tangential velocity, u_w, and the mean density, ρ_w, in the wake as

$$\Delta p = p_{top} - p_{bottom} = \kappa \rho_w {u^2}_w \theta_w \qquad (2-76)$$

Given that the pressure difference is small, this can be related to the circulation, Γ, by

$$\int_{x_{te}}^{x_\infty} d\Gamma_w = -\int_{x_{te}}^{x_\infty} \theta_w \kappa_w dS_w \qquad (2-77)$$

where S_w is the arc distance along the wake. The circulation at the trailing edge is calculated by the difference in the potentials at the trailing edge in the inviscid solution and Eq. (2-77) is numerically integrated from the trailing edge to one grid point upstream of the downstream boundary. The circulation at the downstream boundary is then matched to the circulation obtained from the integration.

Since the wake effects are relatively small,[39] it is only important to know the approximate location of the wake centerline. This simplifies the problem since the actual wake location would have to be found by tracking the streamline of the inviscid solution leaving the trailing edge and then a new grid would have to be created about the new wake so that the boundary conditions on the wake could be applied. Alternatively, the approximate shape of the wake can be found by assuming that the streamline leaves the trailing edge smoothly at the average of the local trailing edge angles and that then the angle between the wake centerline surface and the freestream decays logarithmically, similar to that of a point vortex in a uniform freestream at a given angle of attack[20]. The circulation, Γ, of this point vortex located at the quarter chord point could be determined by forcing flow tangency at the trailing edge of the wing section. The ordinate of the centerline of the wake would then have a form similar to

$$y_{wake} = y_{te} + \tan\alpha(d - \frac{3}{4}c) - \frac{3}{4}c\tan(\alpha) ln\frac{d}{\frac{3}{4}c}/d \qquad (2-78)$$

where d is the x distance from the quarter chord point of the wing section.

The curvature of the flow, κ, can be determined by calculating the rate of change of the flow angle at the approximated wake location.

II.4.7 Wake thickness

The thickness of the wake is accounted for by simply adding the displacement thicknesses obtained from the boundary layer solver to either side of the predefined wake location. The ghost points in the wake are then redefined such that strict flow tangency is enforced along this new surface.

II.5 Comparison to Experiment

TAWFIVE was used to analyze RAE Wing-A wing-body at a Mach number of .8, an angle of attack of 2 degrees, and a Reynolds number of 2.66 million based on the root chord. The pressure obtained from this analysis are compared to some experimental data at two convenient stations in Fig. 15. Even though no attempt was made to try and match lift coefficients by changing Mach number or angle of attack, the comparison between the experimental and predicted pressures is fairly good up to the trailing edge. There TAWFIVE predicts slightly higher pressures. This characteristic behavior has been attributed to the improper modeling of the the strong viscous-interaction region at the trailing edge[20] but may also be due to a combination of the coarseness of the grid at the trailing edge and wind tunnel interference errors.

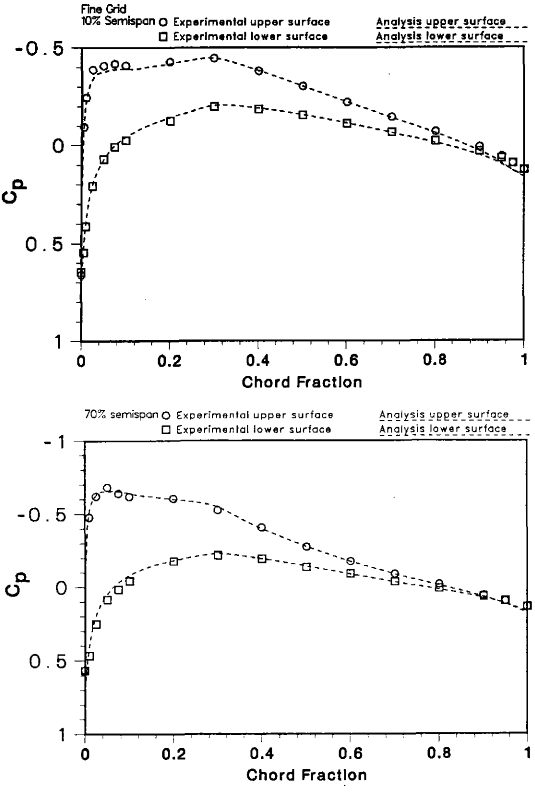

Fig. 15 Comparison of experimental and analytical pressures for RAE Wing-A

CHAPTER III

INVERSE DESIGN METHOD

III.1 Inverse Boundary Condition

As stated earlier, in the direct-inverse method a pressure boundary condition is enforced rather than flow tangency aft of the portions of the wing which are to be designed. Following Gally,[13-15] the input pressure coefficient can be written in terms of the Mach number, M, and the freestream speed, q, as

$$C_p = \frac{2}{\gamma {M^2}_\infty}\left[\left[1 + \frac{\gamma - 1}{2} {M_\infty}^2 \left(1 - \frac{q^2}{q_\infty^2}\right)\right]^{\frac{\gamma}{\gamma-1}} - 1\right] \qquad (3-1)$$

where $q^2 = \left(u^2 + v^2 + w^2\right) {q^2}_\infty$.

Solving for u in Eq. (3-1) yields

$$u = \left[\frac{1 - \frac{2}{(\gamma-1){M^2}_\infty}\left[\left(1 + \frac{\gamma {M^2}_\infty C_p}{2}\right)^{\frac{\gamma-1}{\gamma}} - 1\right]}{1 + \left(\frac{v}{u}\right)^2 + \left(\frac{w}{u}\right)^2}\right]^{\frac{1}{2}} \qquad (3-2)$$

This form of the equation seems to have been chosen over the more obvious form of

$$u = \left[1 - \frac{2}{(\gamma - 1)M_\infty^2}\left[\left(1 + \frac{\gamma {M^2}_\infty C_p}{2}\right)^{\frac{\gamma-1}{\gamma}} - 1\right] - v^2 - w^2\right]^{\frac{1}{2}} \qquad (3-3)$$

since it is less likely that its radicand would be negative. Equating Eq. (3-2) and the first row of Eq. (2-38) results in

$$J_{11}\phi_\xi + J_{12}\phi_\eta + J_{13}\phi_\zeta = \left[\frac{1 - \frac{2}{(\gamma-1){M^2}_\infty}\left[\left(1 + \frac{\gamma {M^2}_\infty C_p}{2}\right)^{\frac{\gamma-1}{\gamma}} - 1\right]}{1 + \left(\frac{v}{u}\right)^2 + \left(\frac{w}{u}\right)^2}\right]^{\frac{1}{2}} - \cos\alpha \qquad (3-4)$$

where $J_{i,j}$ are the elements of $\left(\mathbf{H}^T\right)^{-1}$. A potential, $(\phi_{i,j,k})$, can be formulated in terms of the pressure coefficient by expanding about the grid point location $\left(i-\frac{1}{2},j,k\right)$, and then using central differences in the ξ and ζ direction and second order backward differences in the normal direction, η, yielding

$$
\begin{aligned}
& J_{11}\left(\phi^{n+1}_{i,j,k}-\phi^{n}_{i-1,j,k}\right) \\
& \quad + J_{12}[3\left(\phi^{n+1}_{i,j,k}+\phi^{n}_{i-1,j,k}\right)-4\left(\phi^{n}_{i,j-1,k}+\phi^{n}_{i-1,j-1,k}\right) \\
& \qquad + \phi^{n}_{i,j-2,k}+\phi^{n}_{i,1,j-2,k}]/4 \\
& \quad + J_{13}\left(\phi^{n}_{i,j,k+1}+\phi^{n}_{i-1,j,k+1}-\phi^{n}_{i,j,k-1}-\phi^{n}_{i-1,j,k-1}\right)/4 \\
& \qquad = F\left(C_{p,i-\frac{1}{2},k}\right)
\end{aligned}
\tag{3-5}
$$

where ϕ^n are the potentials at the current time level and ϕ^{n+1} are the updated potentials.

Solving for the ϕ to be specified, Eq. (3-5) becomes

$$
\begin{aligned}
\phi^{n+1}_{i,ky,k} = \frac{1}{J_{11}+\frac{3}{4}J_{12}} & \Big\{ J_{11}\phi^{n}_{i-1,ky,k} \\
& - J_{12}\Big[3\phi^{n}_{i-1,ky,k}-4\left(\phi^{n}_{i,ky-1,k}+\phi^{n}_{i-1,ky-1,k}\right) \\
& + \phi^{n}_{i,ky-2,k}-\phi^{n}_{i-1,ky-2,k}\Big]/4 \\
- J_{13}\left(\phi^{n}_{i,ky,k+1}+\phi^{n}_{i-1,ky,k-1}-\phi^{n}_{i,ky,k-1}-\phi^{n}_{i-1,ky,k-1}\right)/4 & \\
& + F\left(C_{p\ i-\frac{1}{2},k}\right)\Big\}
\end{aligned}
\tag{3-6}
$$

where $F\left(C_{p\ i-\frac{1}{2},k}\right)$ is the right hand side of Eq. (2-72) and $j = ky$ on the wing surface. Also, the η grid lines are numbered such that $ky-1$ is the location of the grid point immediately above the wing's surface. Pressures are specified at half grid point locations in the ξ direction to eliminate the chance of the solution decoupling on 'odd' and 'even' grid points. Since the actual sectional shape of the final wing is unknown initially, the potentials are specified on the wing's surface at the present time level.

III.2 Integration of the Flow Tangency Boundary Condition

Since the grid is boundary conforming, the wing sections in the design region must be updated every so often by integrating the flow tangency condition written in curvilinear coordinates. After Gally, the curvilinear form of the equation can be found by first considering the flow tangency condition for Cartesian coordinates

$$\mathbf{U}^T \nabla F = 0 \qquad \text{with } F(x,y,z) = 0 \tag{3-7}$$

where $\mathbf{U}$ is the physical velocities and F is the function describing the surface of the wing.

The physical velocities can be related to the contravariant velocities using the aforementioned relations, which are repeated here for convenience.

$$[\mathbf{U}] = \begin{pmatrix} x_\xi & x_\eta & x_\zeta \\ y_\xi & y_\eta & y_\zeta \\ z_\xi & z_\eta & z_\zeta \end{pmatrix} \begin{pmatrix} U \\ V \\ W \end{pmatrix} = [\mathbf{H}][\mathbf{V}] = \mathbf{HV} \tag{3-8}$$

By using the chain rule in the same manner in which the above expression was derived, the gradient, ∇, of the surface function, F, with respect to the physical coordinates, x, y, z can be related to the gradient, ∇', of the surface function $S(\xi, \eta, \zeta)$ by

$$[\nabla F] = \begin{pmatrix} \xi_x & \eta_x & \zeta_x \\ \xi_y & \eta_y & \zeta_y \\ \xi_z & \eta_z & \zeta_z \end{pmatrix} \begin{pmatrix} \frac{\partial S}{\partial \xi} \\ \frac{\partial S}{\partial \eta} \\ \frac{\partial S}{\partial \zeta} \end{pmatrix} = (\mathbf{H}^{-1})^T \nabla' S \tag{3-9}$$

Substituting these two into the tangency equation gives

$$(\mathbf{HV})^T (\mathbf{H}^{-1})^T \nabla' S = 0 \tag{3-10}$$

Using the identity from linear algebra,

$$[\mathbf{A}\ \mathbf{B}]^T = \mathbf{B}^T\mathbf{A}^T \tag{3-11}$$

Eq. (3-10) becomes

$$\mathbf{V}^T\left[\mathbf{H}^{-1}\mathbf{H}\right]^T \nabla' S = 0 \tag{3-12}$$

which is reduced to the desired form of the flow tangency condition for curvilinear coordinates :

$$\mathbf{V}^T \cdot \nabla' S = 0 \tag{3-13}$$

A more convenient form is obtained by expanding this to

$$U\frac{\partial S}{\partial \xi} + V\frac{\partial S}{\partial \eta} + W\frac{\partial S}{\partial \zeta} = 0 \tag{3-14}$$

Since the wing is a surface of constant η , where

$$\begin{aligned}
S(\xi,\eta,\zeta) =& \eta(\xi,\zeta)_{ky} - \eta = 0 \\
\frac{\partial S}{\partial \xi} =& \frac{\partial \eta(\xi,\zeta)_{ky}}{\partial \xi} \\
\frac{\partial S}{\partial \eta} =& -1 \\
\frac{\partial S}{\partial \zeta} =& \frac{\partial \eta(\xi,\zeta)_{ky}}{\partial \zeta}
\end{aligned} \tag{3-15}$$

Eq. (3-14) reduces to

$$\left(\frac{\partial \eta}{\partial \xi}\right)_{i,ky,k} = \frac{V}{U} - \frac{W}{U}\left(\frac{\partial \eta}{\partial \zeta}\right)_{i,ky,k} \tag{3-16}$$

The integration of this equation can be handled in two different ways. If the spanwise term, $\frac{\partial \eta}{\partial \zeta}$, is lagged one global iteration, it will always be zero since upon the creation of a new grid, all derivatives of η with respect to the ξ or ζ direction vanish on the wing's surface; and, Eq. (3-16) reduces to

$$\left(\frac{\partial\eta}{\partial\xi}\right)_{i,ky,k} = \left(\frac{V}{U}\right)_{i,ky,k} \tag{3-17}$$

The other approach would be to integrate Eq. (3-16) iteratively. If the contravariant velocities are frozen at their current values, and the spanwise terms are initially assumed to be zero, Eq. (3-17) can be integrated to find the approximate inverse changes $\Delta\eta$. These can be used to find approximations to the spatial spanwise derivative, $\frac{\partial\eta}{\partial\zeta}$, which can then be included in Eq. (3-16) to provide a better approximation to the flow tangency equation. The process can then be repeated using Eq. (3-16) until the spatial derivatives converge. Numerical experiments reveal that the spanwise terms are at least two orders of magnitude smaller than the chordwise terms prior to the creation of the new grid. Hence, the spanwise terms can normally be neglected. Equation (3-17) was integrated using the trapezoidal rule

$$\begin{aligned} &\eta_{i,k} = \frac{II}{2}\left(\left(\frac{V}{U}\right)_{i,k} + \left(\frac{V}{U}\right)_{i-II,k}\right) + (\eta)_{i-II,k} \\ &II = -1 \qquad \text{upper surface} \\ &II = +1 \qquad \text{lower surface} \end{aligned} \tag{3-18}$$

For comparison purposes the fourth order scheme

$$\begin{aligned} \eta_{i,k} =& \frac{II}{24}\left(9\left(\frac{V}{U}\right)_{i,k} + 19\left(\frac{V}{U}\right)_{i-II,k} - 5\left(\frac{V}{U}\right)_{i-2II,k} - \left(\frac{V}{U}\right)_{i-3II,k}\right) \\ &+ (\eta)_{i-II,k} \end{aligned} \tag{3-19}$$

was also used. With the fourth order scheme the trapezoidal rule was used for the first two integration steps. This higher order integration scheme had little effect on the final answers, except for coarse grids in regions of high curvature such as the cove region of a supercritical airfoil.

Since Gally found that calculating V using strictly finite differences was not accurate enough, he instead, using an approach similar to that in Ref. (60), discovered that V was most accurately obtained from the residual expression. First, assume that

$$\frac{V}{U} \approx \frac{\rho hV}{\rho hU} = \frac{\mu_{\xi\eta\zeta}(\rho hV)}{\mu_{\xi\eta\zeta}(\rho hU)} \tag{3-20}$$

and then combine the previously defined averaging and differencing operators

$$\mu_{\eta}(\rho hV)_{i,ky,k} = \frac{1}{2}\left((\rho hV)_{i,ky+\frac{1}{2},k} + (\rho hV)_{i,ky-\frac{1}{2},k}\right) \tag{3-21}$$

$$\delta_{\eta}(\rho hV)_{i,ky,k} = \left((\rho hV)_{i,ky-\frac{1}{2},k} - (\rho hV)_{i,ky-\frac{1}{2},k}\right) \tag{3-22}$$

to generate

$$\delta_{\eta}(\rho hV)_{i,ky,k} = 2(\rho hV)_{i,ky-\frac{1}{2},k} - 2\mu_{\eta}(\rho hV)_{i,ky,k} \tag{3-23}$$

Substituting this result into the residual expression, Eq. (2-43), and solving for the out of plane flux, ρhV, on the wing surface gives

$$\begin{aligned} 2\mu_{\xi\eta\zeta}(\rho hV)_{i,ky,k} = {} & \mu_{\eta\zeta}\delta_{\xi}(\rho hU)_{i,ky,k} + 2\mu_{\xi\zeta}\left(\rho hV_{i,ky-\frac{1}{2},k}\right) + \\ & \mu_{\xi\eta}\delta_{\zeta}\left(\rho hW_{i,ky,k}\right) - \textit{compensation and upwinding terms} \end{aligned} \tag{3-24}$$

Since at convergence the flow should also be tangent to the designed surface, the tangency condition is enforced in the residual expression, Eq. (2-43), by setting

$$(\rho hV)_{i,ky+\frac{1}{2},k} = -(\rho hV)_{i,ky-\frac{1}{2},k} \tag{3-25}$$

The resulting expression is identical the RHS of Eq. (3-24), and the expression for the normal flux becomes

$$\mu_{\xi\eta\zeta}(\rho hV)_{i,ky,k} = \frac{Residual}{2.0} \qquad (3-26)$$

Note that since the residual is not zero in the design region due to the inverse boundary condition, this expression reveals that there will be a mass flux of fluid from the boundary[23-37] during the iterative design process. No attempt was made to account for this transient flux, since at convergence it would be zero.

Upon substitution of Eq. (3-26) into Eq. (3-20) and using the cell averaged flux, ρhU, on the surface the boundary condition becomes

$$\frac{\partial\eta}{\partial\xi} = \frac{V}{U} \approx \frac{\mu_{\xi\eta\zeta}(\rho hV)}{\mu_{\xi\eta\zeta}(\rho hU)} = \frac{Residual}{2\mu_{\xi\eta\zeta}(\rho hU)} \qquad (3-27)$$

The changes normal to the surface at each spanwise station are obtained by integrating from the beginning of the inverse region to the trailing edge using the trapezoidal rule.

Assuming that the grid line leaving the wing in the η direction is normal to the wing, these changes, $\Delta\eta$, are then converted from computational to physical units by scaling by transformation metrics such that

$$\Delta l = \Delta\eta\sqrt{\frac{\partial x}{\partial\xi}^2 + \frac{\partial y}{\partial\eta}^2} \qquad (3-28)$$

After subtracting the boundary layer displacement thickness from the inverse changes, Δl's, which are linearly interpolated to the user defined input stations, the resulting displacements are added to the initial airfoil sections yielding the new wing surface for the current time level.

III.3 Relofting

Many times the trailing edge thickness may be too large if the leading edge curvature is too small or may be 'fish-tailed' if the leading edge curvature is too large. These undesirable situations can be remedied by a procedure called relofting where the designed surface is rotated about the leading edge to meet a specified trailing edge ordinate or trailing edge thickness.[6–8,23,24]

This relofting procedure can be accomplished in two separate ways.[13,14] In the first method, assuming both the upper and lower surfaces of the wing are being designed, the user specified trailing edge ordinate,

$$y_{t_{\frac{upper}{lower}}} = y_{avg} \pm \frac{\Delta_t}{2} \qquad (3-29)$$

is subtracted from the ordinate of the displaced surface,

$$y_{design} = y_{initial_{\frac{upper}{lower}}} \pm \Delta_{\frac{upper}{lower}} \qquad (3-30)$$

to yield a correction of

$$\delta_{r_{te}} = y_t - y_{design} \qquad (3-31)$$

where Δ_t is the user specified trailing edge thickness, $\Delta_{\frac{upper}{lower}}$ is the initial inverse change, $y_{initial}$ is the trailing edge ordinate of the original airfoil section, and y_{avg} is the average of the trailing edge ordinates of the input geometry.

This correction,

$$\delta_r(x) = \delta_{r_{te}} \times \left(\frac{x - x_{le}}{chord}\right) \qquad (3-32)$$

is proportionally added to the initial inverse displacements which amounts to a rotation of the displaced surface about the leading edge to meet the trailing edge ordinate.

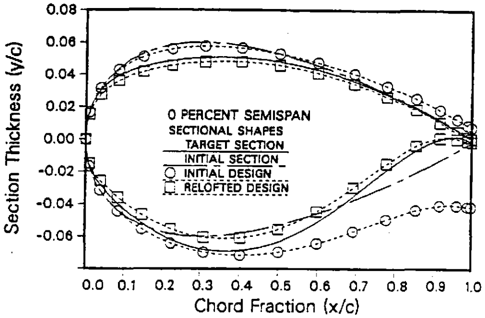

Fig. 16 The effect of relofting on the design in the initial stages of convergence

To illustrate this relofting procedure, the first global iteration of a typical design before and after relofting is revealed in Fig. 16.

If only the trailing edge thickness is specified, allowing the trailing edge ordinate the freedom to vary, the correction instead becomes

$$\delta_{r_{te}} = \left(\frac{\Delta_t}{2} - \frac{\Delta_u + \Delta_l}{2}\right)\left(\frac{x - x_{le}}{chord}\right) \qquad (3-33)$$

where Δ_u and Δ_l are the initial inverse changes on the upper and lower surfaces respectively. It should be noted that the inverse displacements are positive when they cause an increase in thickness.

The second relofting scheme determines the displacements aft of the direct-inverse junction of the design region in the same way, but the leading edge ordinates are thinned to meet the displaced surface at the beginning of the design region. This insures that the leading edge shapes remain in the same family of airfoils.

$$y^{n+1}(x) = y^{n}(x)\left(\frac{{y_{idle}}^{n+1}}{{y_{idle}}^{n}}\right) \tag{3-34}$$

where y_{idle} is the airfoil thickness at the direct-inverse interface in the chordwise direction.

In order afford the designer extra flexibility, one more relofting scheme was devised where a portion of the trailing edge region is user specified instead of just the trailing edge ordinate. Using the same rational as with the rotation scheme, the correction added to the displaced surface to meet the specified ordinate at the aft direct-inverse junction located at x_{idte}, is

$$\delta_r(x) = \delta_r(x_{idte}) \times \left(\frac{x - x_{le}}{x_{idte} - x_{le}}\right) \tag{3-35}$$

CHAPTER IV

REMEDYING SPANWISE INSTABILITIES

IV.1 Spanwise Oscillations

In the original work by Gally[13,14], the pressure distributions applied at the computational grid stations of constant ζ lines on the wing in the design region were obtained by spanwise, linear interpolation of the pressures input by the user at design stations to every grid station delimited. This meant that the inverse boundary condition was enforced at every constant ζ grid station in the design region, and that every sectional shape was determined relatively independent of the others. Unfortunately, an annoying divergent spanwise oscillation problem sometimes occurred when designing a wing which required extensive relofting, especially when the initial section was thinner than the target. This oscillation led to sections which were too thick or too thin at adjacent constant ζ grid station. (see Fig. 17). This problem was more pronounced when the sweep was increased or the aspect ratio was decreased and was usually divergent except for very high aspect-ratio wings (AR=10) with no sweep.

Early in the research, it was discovered that the problem could be circumvented by specifying the C_p distribution at at least every other constant ζ grid station and then linearly interpolating the inverse displacements calculated at those grid stations to the other grid stations included in the design region. The regions in the middle of the design region were simply analyzed using the original flow-tangency boundary

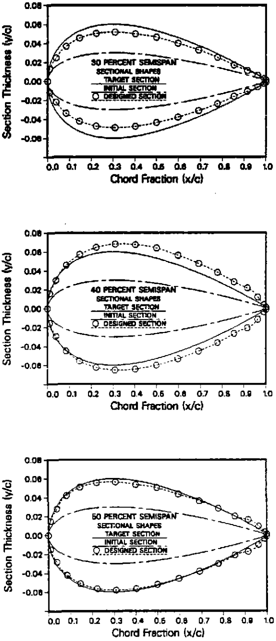

Fig. 17 Alternating thick-thin sections for a divergent medium grid case

condition. The resulting sections, interpolated to the geometry input stations, were all relofted as usual to satisfy the trailing edge ordinate condition. This procedure led to a convergent solution most of the time, except when designing wings with significant sweep or with low aspect ratios, such as Lockheed Wing-B and Wing-C.

It was later discovered that a similar procedure was briefly discussed in Ref. 40 to overcome a decoupling of the solution in the chordwise and spanwise direction leading to a numerical instability when using an inverse panel-method code. In this case, the ordinates of the 'odd' points along the chord were obtained by quadratic interpolation using the ordinates of adjacent 'even' chordwise points while the ordinates of each 'odd' spanwise grid station were generated using linear interpolation between the contiguous 'even' spanwise stations. This procedure effectively eliminated half of the unknowns. The similarities of the decoupling problem in this scheme and our direct-inverse method are quite evident, even though the design schemes are quite different in methodology.

Although this somewhat heuristic cure to the problem seemed to work for the most part, the fundamental cause for this problem was not well understood, hence the oscillation problem was investigated in much greater depth. Initially, it was thought that either the inverse boundary condition or the relofting scheme was solely to blame, which led at first to a series of reformulations; while none of these were successful, they did create great insight into the problem.

Since the oscillation problem seemed to stem from the uncoupling of the solution in the spanwise direction, the original inverse boundary condition in Eq. (3-5) was rewritten as

$$
\begin{aligned}
\phi^{n+1}_{i,ky,k-1} - \frac{4J_{11}+3J_{12}}{J_{13}}\phi^{n+1}_{i,ky,k} - \phi^{n+1}_{i,ky,k+1} = \\
\frac{-4}{J_{13}}\Big\{ & J_{11}\phi^{n}_{i-1,ky,k} \\
& - J_{12}\Big[3\phi^{n}_{i-1,ky,k} - 4\left(\phi^{n}_{i,ky-1,k} + \phi^{n}_{i-1,ky-1,k}\right) \\
& + \phi^{n}_{i,ky-2,k} + \phi^{n}_{i-1,ky-2,k}\Big]/4 + F\left(C_{p\ i-\frac{1}{2},k}\right)\Big\} \\
& + \phi^{n}_{i-1,ky,k+1} - \phi^{n}_{i-1,ky,k-1}
\end{aligned} \tag{4-1}
$$

such that the $\phi's$ could be obtained implicitly in the spanwise direction. Although this would seem to strongly couple the potential field in the spanwise direction, it did not deter the solution from oscillating in the slightest regard.

One form of Eq. (3-4) was tried using one-sided differences for the spanwise derivatives, and yet another which specified the C_p at $(i-\frac{1}{2}, ky, k-\frac{1}{2})$ grid locations; but they did not cure the problem either.

The idea of devising a conservative formulation of the inverse boundary condition using a control volume approach more in keeping with the spirit of the finite volume scheme used in FLO-30 or the approach used in Ref. (41) was conceived, but the details necessary to implement this approach were never pursued.

Attention was then directed towards the methods used to integrate the flow tangency equation and the relofting of the resulting shapes. Since the problem seemed to stem from the lack of spanwise information, the spanwise terms in Eq. (3-16) were included during the surface update process. The ratio $\frac{W}{U}$ was obtained from Eq. (2-39) and the potentials at the present time level. An approximation of the spanwise derivatives, $\frac{\partial\eta}{\partial\zeta}$, was calculated using central spanwise differences of the initial displacements which were calculated using Eq. (3-17). Then Eq. (3-16) was solved iteratively until there was no appreciable change in the displacements. In case the relofting adversely affected the results, this process was also tried after the inverse displacements were changed with relofting. However, the inclusion of these terms had very little effect on the displacements calculated since, in both cases, they were at least an order of magnitude smaller and did not help the divergence problem in the slightest regard.

Spanwise smoothing of the displacements was also tried. Although this technique did provide a smoothly varying distribution of sectional thicknesses, the divergence was merely slowed. Sometimes the solution would reach a settling point where it would not converge further, but the resulting section shapes were not satisfactorily accurate.

In the midst of the search for a cure for the oscillation problem, it was discovered that if the potentials obtained from a converged solution of the target section were specified on the wing using a different initial geometry, the design solution would converge without oscillating. This result appeared to condemn the inverse boundary condition and redeem the integration and relofting schemes. On the other hand, if the inverse boundary condition was applied at <u>every</u> grid station, and displacements were calculated only at <u>every other</u> spanwise grid station and were interpolated to the stations in between, the solution also converged, which seemed to indicate that the inverse boundary condition was not the sole origin of the problem. Thus, it appeared that the problem was stemmed from a combination of causes.

IV.2 Success

After the many failed attempts of remedying the oscillation problem by reformulating the inverse boundary condition and the integration and relofting shemes, attention was directed towards the residual and the terms composing it. The residual is directly affected by the inverse boundary condition; moreover, the residual directly influences the section shapes through the integration of the flow tangency boundary condition. Consequently, the residual was broken into its major components and plotted in the spanwise direction after each surface update of a known divergent case. This case happened to be a medium-grid design of Lockheed Wing-A with the initial section being a NACA 0006 section over the entire wing and the target being a NACA 0012 section. The design region extended from 30% to 70% semispan. Sample plots for this divergent case are shown at four different time levels in Fig. 18. where the total residual also includes the upwinding terms. As can be seen, the compensation terms, which include spanwise derivatives of ϕ. at first are very small compared to the rest of the terms but later tend to dominate and amplify the oscillation. This oscillation starts at the direct-inverse interface or, in other words, at the first spanwise station from the root in the design region and propagates spanwise as a damped oscillation with a period of two grid spacings.

The oscillation problem seems to be driven by a combination of events which build upon each other causing a divergence. It is believed that the initial mismatch in the potentials at the direct-inverse interface in the spanwise direction is amplified by the compensation terms which include spanwise derivatives of the potential function.

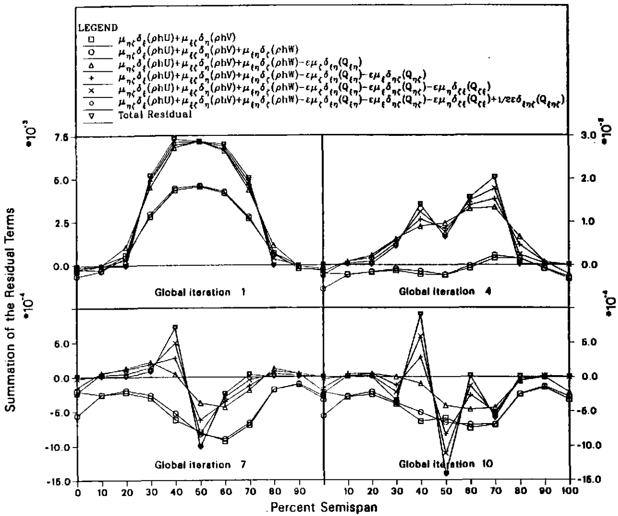

Fig. 18 The time history of the residual and the terms composing it at the upper trailing edge for a typical divergent solution. (The design region extends from 30-70% semispan)

The residual is then undershot and overshot on alternating spanwise stations. This oscillation is further magnified by relofting, which creates a section that is too thin when the slopes defined in Eq. (3-27), which of course are directly proportional to the residual, are too large and vice-versa. Since more or less fluid has to be ejected from the section that is too thin or thick, respectively, to give a streamline approximately corresponding to the correct target section, the potential field shown in Fig. 19 at each design station is forced further away from the adjacent fields by the inverse boundary condition which in turn forces an even further undershoot or overshoot of the residual, resulting in a growing spanwise oscillation. With the aid of other numerical experiments, it has been found that it is only necessary to have two adjacent design stations to drive this oscillation to divergence. It is of interest that when the wavy wing surface resulting from a divergent solution was analyzed with TAWFIVE, the potential field varied more smoothly in the spanwise direction than did the potential field obtained from the design solution. In light of the previous discussion, this result verifies that the inverse boundary condition was, in fact, forcing the adjacent potential fields away from each other.

It should be noted that this problem is not due solely to the implementation of the direct-inverse technique since this oscillation has not been observed with the ZEBRA design code. Rather, it seems to be unique to the coupling of the method with the analysis code, FLO-30. Seemingly, two pertinent differences between the two codes exit. Firstly, the ZEBRA code, which uses a sheared Cartesian coordinate system aligned with the wing, applies the boundary conditions at the mean plane of

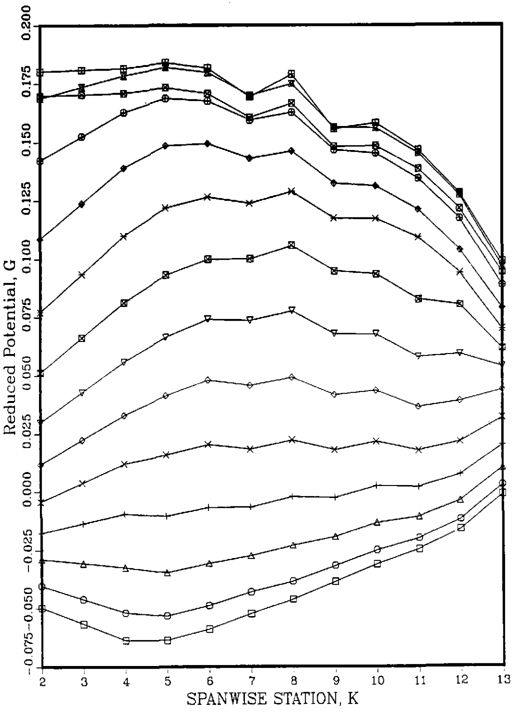

Fig. 19 The potential field on the wing's surface for a diverging design solution

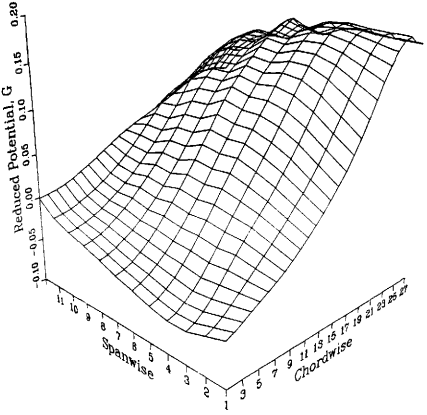

Fig. 19 Continued

the wing. This first difference is important, since the actual thickness of the wing may have less of an impact on the flowfield computed by the ZEBRA scheme due to the fact that the point of application of the boundary condition is not changing with time. Secondly, its full potential, fully conservative numerical scheme uses a mid-segment type of finite difference approach rather than a finite-volume scheme with fourth derivative type compensation terms[16] that seem to be amplifying the errors in the design solution.

Nevertheless, after exploring many alternatives to counter this oscillation problem, four methods based on the previous observations have been devised to damp out the spanwise oscillation:

A) Specify the inverse boundary condition at at least every other spanwise station and linearly interpolate the inverse displacements to the stations lying in between. This has been named the Type II-2 method.

B) Specify the inverse boundary condition at every station, but again only calculate inverse changes at every other station and linearly interpolate the inverse changes to the stations in between. This will be referred to as the Type II method.

C) Immediately prior to every surface update, calculate all spanwise derivatives of the potential in the residual based upon a potential function smoothed in the spanwise direction. This smoothing is accomplished by first defining the operator σ_ζ as

$$\sigma_\zeta f = \frac{\varepsilon}{4} f_{k-1} + \left(1 - \frac{\varepsilon}{2}\right) f_k + \frac{\varepsilon}{4} f_{k+1}, \qquad 0 \leq \epsilon \leq 1 \qquad (4-2)$$

where ε determines the amount of smoothing. Then using σ in the spanwise differentiation of ϕ with the maximum amount of smoothing (i.e., $\varepsilon = 1$)

$$\left(\frac{\partial \phi}{\partial \zeta}\right)_{i,j,k+\frac{1}{2}} = \sigma_\zeta \delta_\zeta \phi \qquad (4-3)$$

the smoothed spanwise derivative of ϕ becomes

$$(\phi_\zeta)_{i,j,k+\frac{1}{2}} = \frac{(\phi_{i,j,k+2} - \phi_{i,j,k} + \phi_{i,j,k+1} - \phi_{i,j,k-1})}{4.0} \qquad (4-4)$$

D) Smooth the slopes, $\frac{\rho hV}{\rho hU}$, in the spanwise direction in the design region in the same manner as with method C. It should be noted that, as stated earlier, smoothing the integrated slopes, i.e the inverse corrections, did not suppress the oscillation but only slowed the rate of divergence.

Three different cases were studied in order to test the effectiveness of each method at suppressing the oscillation and in reproducing the known target section. All three cases used Lockheed Wing-A at a Mach number of .8 and at an angle of attack of 2^o. The first case utilized a NACA 0012 airfoil as the initial section and the original supercritical wing sections accompanying Wing-A as the target section. The design region stretched from 30-70% semispan of the wing and began 5% aft of the leading edge and extended to the trailing edge. Since a medium grid (80x12x16) was employed, there was a constant ζ grid station at every 10% semispan. Results are shown in Fig. 20 for the four different approaches.

Although all four approaches worked well for this case, by using the RMS of the errors between the target section and the section designed as a measure of accuracy, methods A and C produced the best results for this case in the interior as well as at the edges of the design region. For the same number of flowfield iterations, the technique D produced the most unsatisfactory results when compared to the target sections.

The effect of each approach on the residual at the trailing edge after 10 surface updates can be seen in Fig. 21. The discontinuities in the residual for method A is due to the fact that the inverse boundary condition is applied only at the 30, 50 and 70% semispan locations. All four approaches have a characteristic jump in the residual at the first spanwise design station at 30% semispan. This jump is probably due to the previously discussed spanwise mismatch problem with the potentials at the direct-inverse interface, which manifests itself in the compensation terms. The Type II method had the largest jump at this interface, while the Type II-2 method had the smallest jump. Notice that the spanwise distributions of the residual for the two smoothing approaches are quite similar in the design region.

Since only small differences existed between the methods for the previous test case, a more severe test was conducted by designing an entire wing using NACA 0006 sections as the initial airfoils and NACA 0012 sections as the targets. These sections were chosen due to the fact that most of the problems in the past were amplified by beginning with a thin section and targeting a thicker section. Furthermore, a

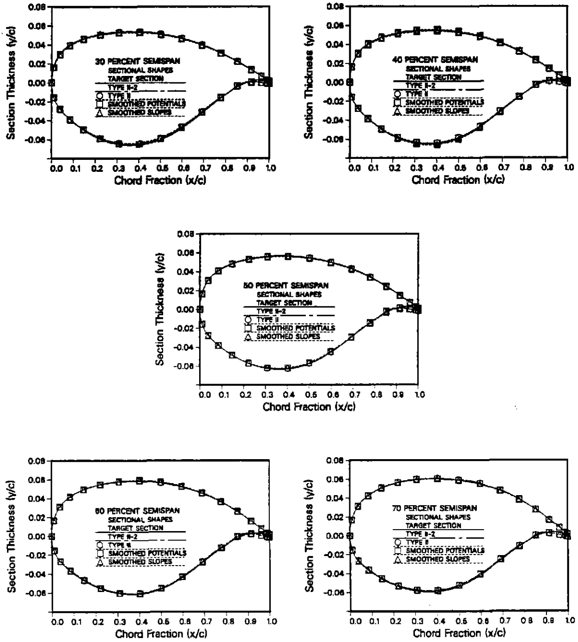

Fig. 20 Comparison of airfoil sections designed using the four spanwise oscillation remedies on a medium grid from 30% to 70% semispan.

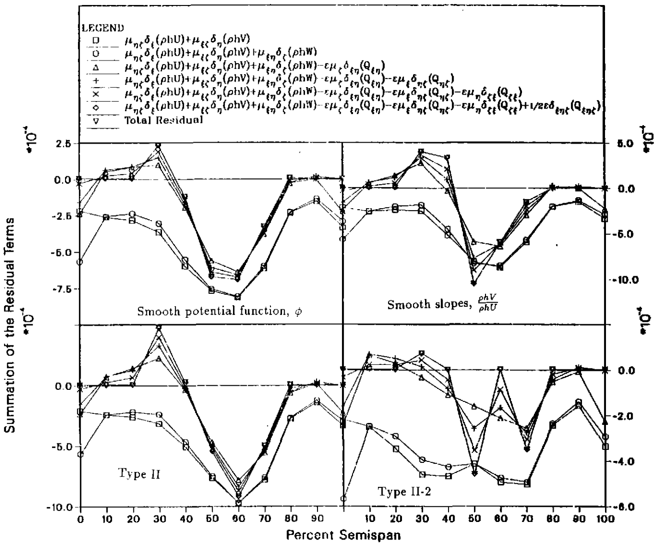

Fig. 21 Breakdown of the Residual at the trailing edge on the upper surface for the four spanwise oscillation remedies after 10 global iterations

full wing design would reveal whether the accuracy of each method depended on the spanwise location of the wing.

When an attempt was made to compute these cases, it was discovered that when using the smoothing two smoothing techniques, (methods C and D), it was necessary to use zero order extrapolation of the displacements from the adjacent grid station to the root section. The root section tended to lag in the convergence process in comparison to the rest of the grid stations. This behavior is possibly due to a slowly converging flowfield at the the wing-fuselage juncture. Since all of the sections started out too thin, this lagging of the root section forced the adjacent grid station to quickly become too thick, which led to divergence at the root in both cases. Zero order extrapolation of the nondimensionalized displacements forced the root section to converge at a rate which was more in compliance with the rest of the grid stations at the expense of degrading the accuracy of the root section. Since the root section has been successfully designed independently, presumably, this problem might be circumvented by simply allowing the flowfield solution to converge further before each relofting, although such a procedure would probably be a less efficient approach.

Also, no smoothing of the potentials or the residuals was used at the tip. Since both the residual and the potentials are quickly varying in the spanwise direction in the tip region, smoothing leads to large errors in the residuals and hence the section shapes. In fact, better results can be obtained for the smoothed potential approach by using a zero order extrapolation of the normalized displacements from the grid station inboard of the tip to the tip. Overall though, the inboard sections of the wing slowly became thicker, while those outboard responded more quickly, initially causing these outboard sections to actually become too thick.

The resulting sectional shapes for the four different methods are compared in Fig. 22. As can be seen in the figure, method C works well when designing in the interior of the wing, but did not give satisfactory results at the tip of the wing where smoothing the quickly varying potential led to large errors in the section shapes. Since the residuals also varied quickly at the tip, the slopes at the tip were not smoothed with method D. Since there were not any slopes defined at the fuselage ghost point location, $(i,\ ky,\ 2)$, the slopes were not smoothed at the root either. This method produced the most accurate results while still managing to suppress the oscillation problem. In contrast, the Type II and Type II-2 methods worked well on the entire wing surface, and nothing special needed to be done at the root or tip.

The same case was executed on the fine grid (160x24x32) to study any effect of grid size on the accuracy and effectiveness of the methods. This grid allowed 21 design stations which were located a distance of 5% semispans from each other. When using the Type II and Type II-2 methods, the lagging of the root section actually forced the section located at 10% semispan, two grid stations outboard, to become too thick, which led again to a divergent solution. Thus, for this fine grid case, it was necessary to use zero order extrapolation of the the normalized displacements from the adjacent station to the root when using all four remedies. Cases which do not require such large changes in thickness at the root have not required this procedure using the Type II and Type II-2 methods. In addition, because of the aforementioned

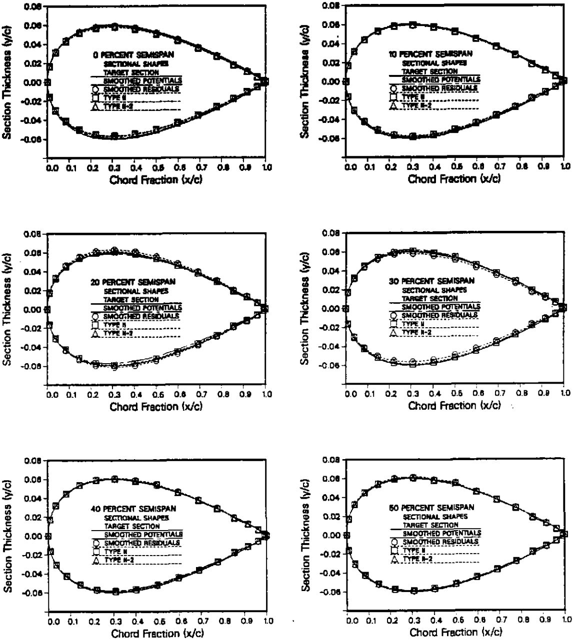

Fig. 22 Comparison of airfoil sections designed using the four spanwise oscillation remedies on a medium grid from 0% to 100% semispan.

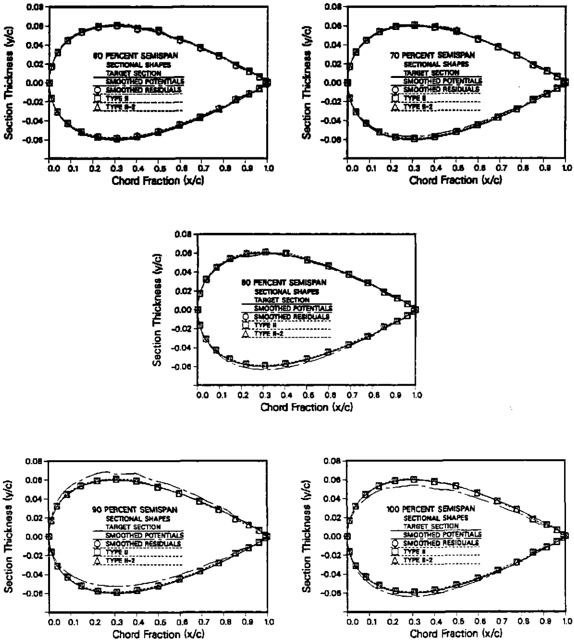

Fig. 22 Continued

problems with the smoothing approaches at the tip, no smoothing was used at the tip section.

The results for this case are shown in Fig. 23. For this case, the smoothing approaches yielded satisfactory sections on the region of the wing spanning from about 30% to 85%. Elsewhere, the sectional shapes vary significantly from the target section. Thus, the smoothing approaches work well when designing in the interior of the wing, but they do not give satisfactory results near the root and tip of the wing.

An objective measurement of the accuracy of the sections in relation to the target can be obtained using a coefficient of determination, r, defined as[42] :

$$r = \sqrt{1 - \frac{\sigma_{y,x}^2}{\sigma_y^2}} \qquad (4-5)$$

where σ_y is the standard deviation of the ordinates of the target section defined as

$$\sigma_y = \left[\frac{\sum_{i=1}^{n}(y_i - y_{mean})^2}{n-1}\right] \qquad (4-6)$$

and

$$\sigma_{y,x} = \left[\frac{\sum_{i=1}^{n}(y_i - y_{design})^2}{n-2}\right] \qquad (4-7)$$

is the deviation of the design from the target for the same x values. This quantity varies from 0 to 1, one being perfect.

Moreover, to further clarify which method produced the least amount of oscillation, the average error variation in the spanwise direction for each method should be compared. The spanwise variation of the coefficient of determination and average percent error are shown in Figs. 24–29. The Type II and Type II-2 methods

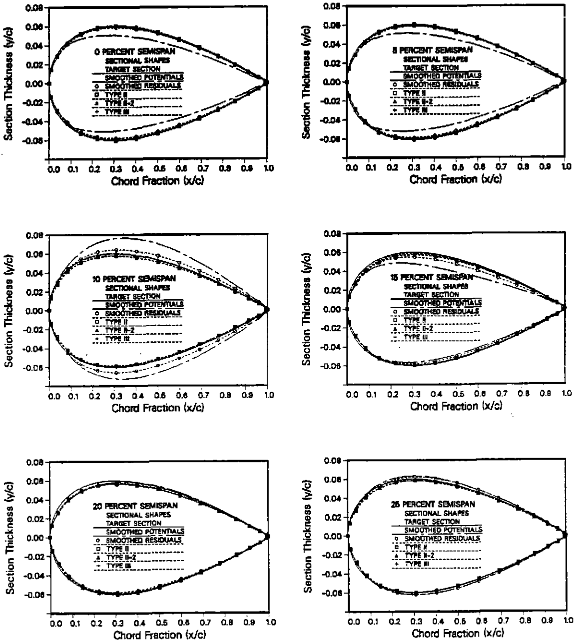

Fig. 23 Comparison of airfoil sections designed using the four spanwise oscillation remedies on a fine grid from 0% to 100% semispan.

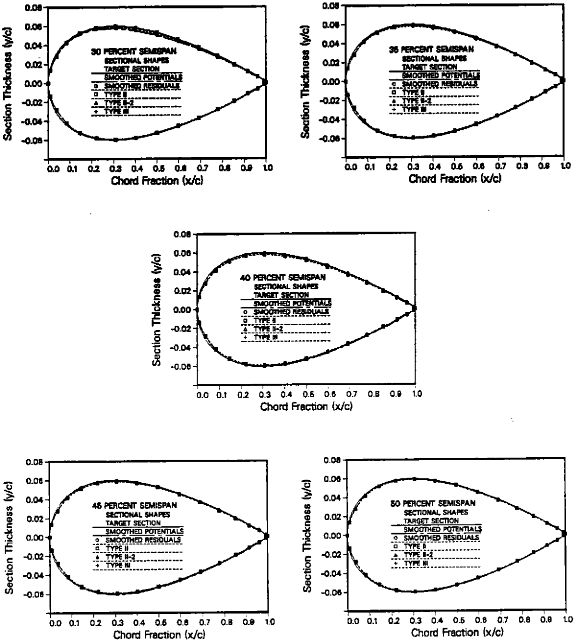

Fig. 23 Continued

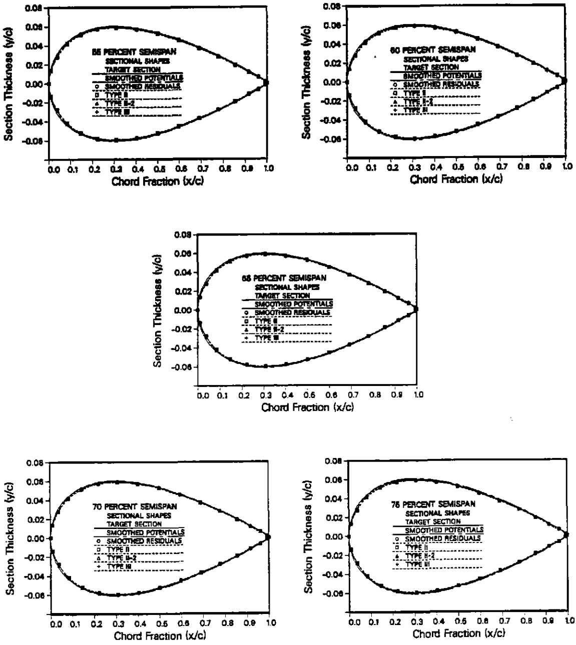

Fig. 23 Continued

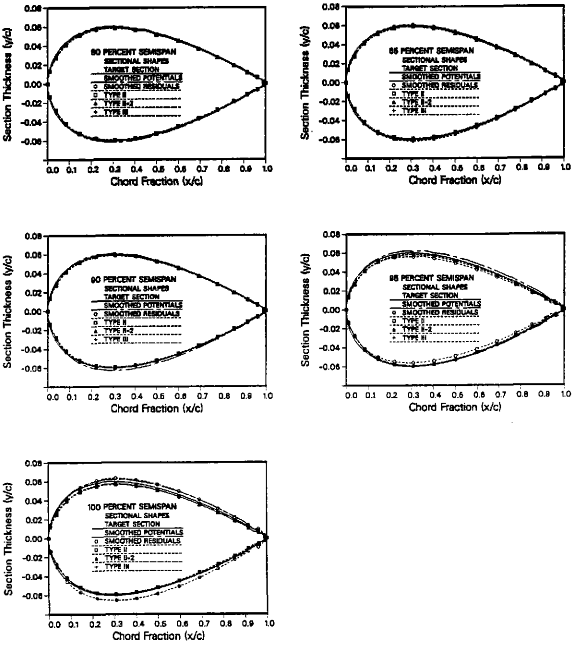

Fig. 23 Continued

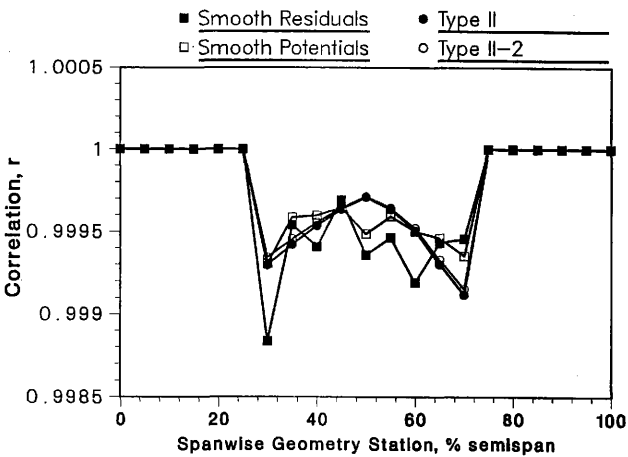

Fig. 24 The effect of the four spanwise oscillation remedies on the coefficient of determination for the medium-grid, partial-wing design

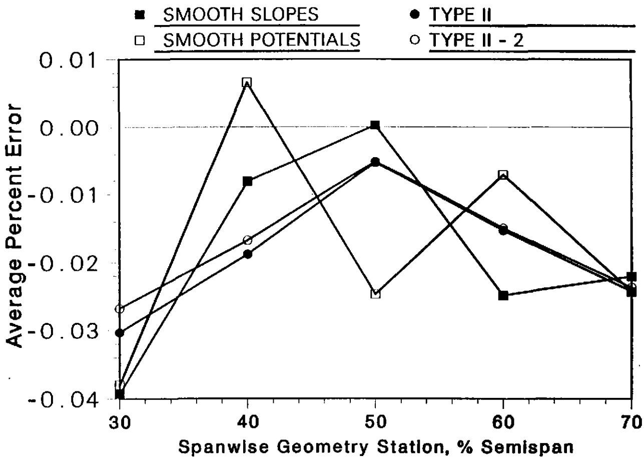

Fig. 25 The effect of the four spanwise oscillation remedies on the average percent error between the target and the design sections for the medium-grid, partial-wing design

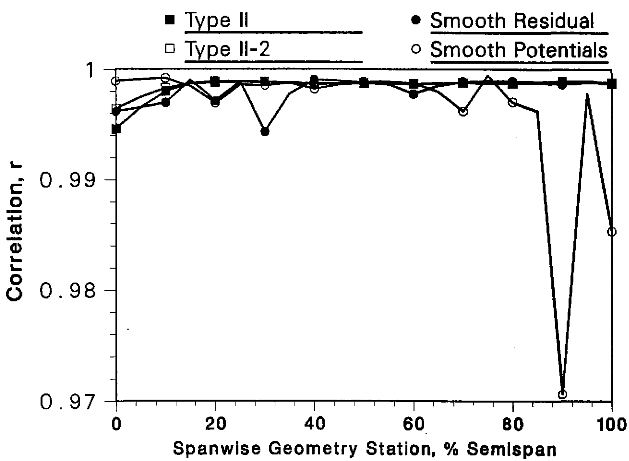

Fig. 26 The effect of the four spanwise oscillation remedies on the coefficient of determination for the medium-grid, full-wing design

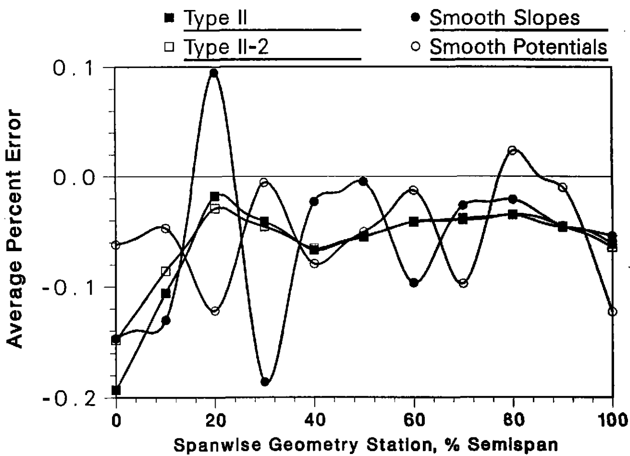

Fig. 27 The effect of the four spanwise oscillation remedies on the average percent error between the target and the design sections for the medium-grid, full-wing design

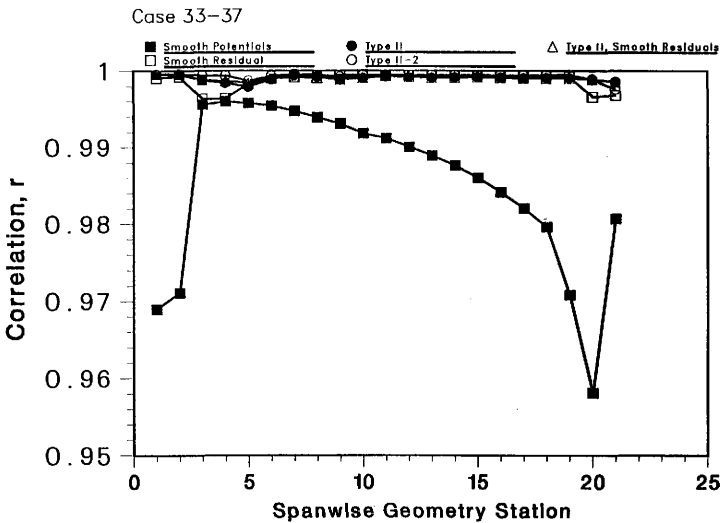

Fig. 28 The effect of the four spanwise oscillation remedies on the coefficient of determination for the fine grid, full wing design

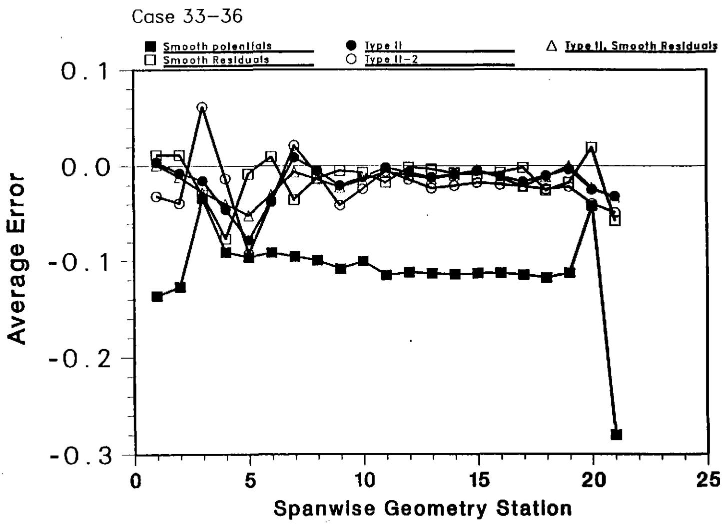

Fig. 29 The effect of the four spanwise oscillation remedies on the average percent error between the target and the design sections for the fine-grid, full-wing design

produced the least amount of oscillation, while smoothing the potentials produced the most amount of oscillation in the error.

There is still some doubt by this investigator whether only secondary aberrations have been observed and not the true, fundamental cause of the oscillation. In light of this, another effect that should be investigated is that of the addition of mass into the flowfield by the inverse boundary condition. Some other investigators[23,43] have included a source correction in the far field and in the near field[43]. In this research, this source correction was neglected since this addition of mass would be driven to zero at convergence. But, its effect on the unconverged solution is not clear. In order to see if this had a significant effect on the solution. a quick, numerical experiment was performed in which the distance to the outer boundary was doubled. (See Fig. 30) Presumably, if the addition of mass was adversely affecting the boundary condition in that region for a given distance, it would have less of an effect if the distance were increased since the additional mass flux arriving at the boundary would be less and the outer boundary boundary condition would be better satisfied. When this computation was completed, however, the solution seemed to be completely unaffected, diverging at the same point in the iteration history. This was only a simple attempt at proving that the sources on the wing were not the fundamental motivation for the oscillation. A thorough analysis must consider the effect of this mass addition on the downstream boundary and the near field. The downstream boundary could be stretched further downstream, and appropriate source correction terms, using the flux ejected from the inverse regions of the wing as the source strength, could be added to the reduced potential in the entire flowfield.

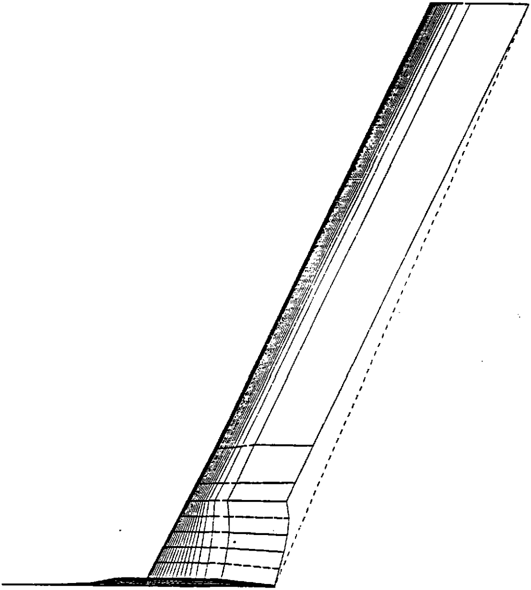

Fig. 30 Grid System at the wing-body's surface with a radial boundary stretched twice as far as the original grid system

Another possible cause could be the assumption of flow tangency used in the residual expression in the integration of the flow tangency equation. When this assumption is made, not only are the fluxes reflected about the current wing boundary, but so are the compensation terms. This procedure in effect doubles the amplitude of the $\delta_{\eta\zeta}$ and the $\delta_{\xi\eta}$ type compensation terms. Since the flow is not generally tangent to the current shape when designing a new airfoil section, reflecting the compensation terms may be initially incorrect. An alternative formulation may be needed.

In retrospect, a few comments about the advantages of each method in different design situations are warranted. For instance, methods C and D give the designer the most flexibility; the desired pressure distributions can be imposed at every spanwise grid station, and the section shapes corresponding to each grid station can be calculated relatively independently of the adjacent stations. On the other hand, because of the interpolation required in the first two methods, the section shapes at 'odd' stations are directly dependent upon the shapes at 'even' stations; so although the designer loses a little flexibility, he gains a smoother spanwise distribution of section thicknesses in the spanwise direction. From a designer's standpoint of course, method A is the most restrictive of the four, but it yields the smoothest designs in the spanwise direction, and converges the quickest. Therefore, method A (i.e., the Type II-2 method) would most probably be the best to use with wings of moderate to high aspect ratios. But, Method B (i.e., the Type II method) would most probably be necessary for wings with aspect ratios of the same order as Lockheed Wing-B.

CHAPTER V

RESULTS AND DISCUSSION

Since the versatility of the method in designing multiple, overlapping regions of the wing has already been well demonstrated by Gally[44,13], most of the test cases presented, herein, were chosen instead to exhibit some of the constraints and limitations of the current inverse design procedure. The cases were chosen to reveal the approximate limits imposed on the aspect ratio and sweep of the wing; and the significance of grid skewness, viscous interaction, grid refinement, and the initial airfoil on the final airfoil section design. Some questions about the compatibility of Mach number and pressure distribution will be answered by designing a wing at one Mach number using pressures obtained from a wing analysis at a different Mach number. Finally, preliminary results will be presented for a partial wing design beginning aft of the leading edge and terminating forward of the trailing edge.

V.1 Boundary Layer and Wake Effects

One of the objectives of this study was to determine the significance of various viscous effect in the design of transonic wings[9]. The wing chosen for this study was a typical transport type wing, Lockheed Wing-A. This wing has an aspect ratio of 8.0, a leading edge sweep of 27^o, a taper ratio of .41, a twist of 2.28^o at the root and -2.04^o at the tip, and 1.5^o of dihedral.

An input pressure distribution was obtained by analyzing Lockheed Wing-A using full viscous effects ; these included boundary layer displacement thickness, wake thickness, and wake curvature. The flight Mach number of .8, angle of attack of two degrees, and Reynolds number, Re, of 25 million used in the analysis were thought to represent flight conditions for a typical, average-sized transport; and the distribution was considered to be typical of that which would be available to and desired by a designer. All computations were performed on a fine (160x24x32) grid. The resulting pressure distributions obtained from the analysis were used in two separate design cases, each composed of five and three subcases, respectively. The first series of cases was a full wing design using the target section as the initial section. By using the target section, any effect of the initial section on the final outcome would presumably be eliminated. The type II design method was used and the inverse boundary condition was enforced from 5% aft of the leading edge to the trailing edge. Furthermore, relofting was not initially done at all. The results for the partially converged cases were plotted and then further converged allowing relofting to take place. In this way, the effect of relofting on the final design could be determined. The iteration history of each case was kept the same, even though by doing this the absolute level of convergence could very well be different since changes of various magnitudes were associated with each case. The large amount of computational time required for these cases dictated this type procedure and for comparison purposes this approach is acceptable. Fortunately, it turned out that the sectional shapes in every case were varying quite slowly by the end of the design run, indicating that the sections were near convergence.

In each case, viscous options were 'turned off' one at a time to assess their effect. In the first case, the wing was designed with all viscous effects. In the second, the lag entrainment was turned off. The third case did not use wake curvature, while the fourth neglected both wake curvature and wake thickness. Finally, in the fifth case the wing was designed inviscidly. The resulting unrelofted designs for each case are compared in Fig. 31. As expected, the inviscidly designed sections are slightly thicker at the root where the normalized boundary layer displacements are thinnest (see Fig. 32) and become increasingly thicker towards the tip in accordance with the thickening boundary layer.

Neglecting lag entrainment, wake curvature and thickness had very little effect on the designed sectional shapes overall. But, if the trailing edge region is examined closely for cases with the wake effects neglected, the trailing edges sometimes cross.

Upon converging these shapes further and enforcing a trailing edge ordinate requirement with relofting, significantly different results were obtained. As shown in Fig. 33, the inviscidly designed shapes are now thinner on the upper surface and slightly thicker on the lower surface, especially in the cove region where viscous effects are large. Also, because of the relofting involved, the leading edge radius has become smaller. The rest of the cases produced sections which did not deviate much from the target, except near the tip. However, neglecting both wake effects produced sections that were actually thicker than the target. This change was due to the relofting that was necessary to uncross the trailing edges, which produced larger leading edge radii and hence thicker sections.

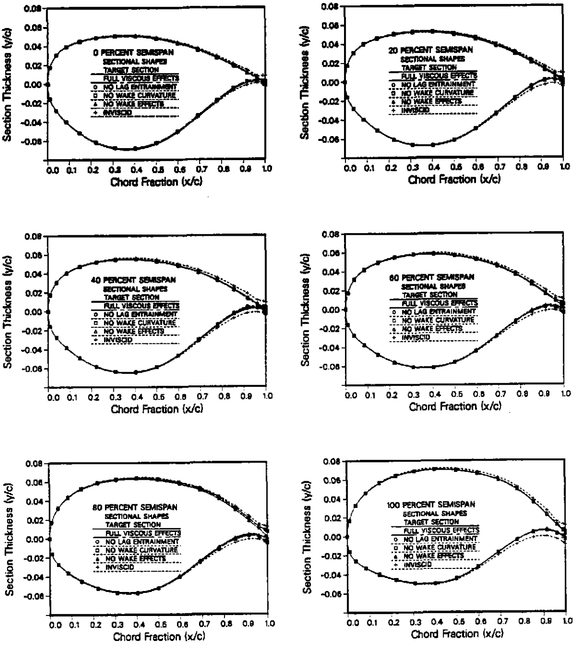

Fig. 31 Comparison of the unrelofted sectional shapes designed using different viscous interaction assumptions with a pressure distribution obtained from a fully viscous analysis of Lockheed Wing-A at a $Re = 24 \times 10^6, M = .8$, and an $\alpha = 2^o$

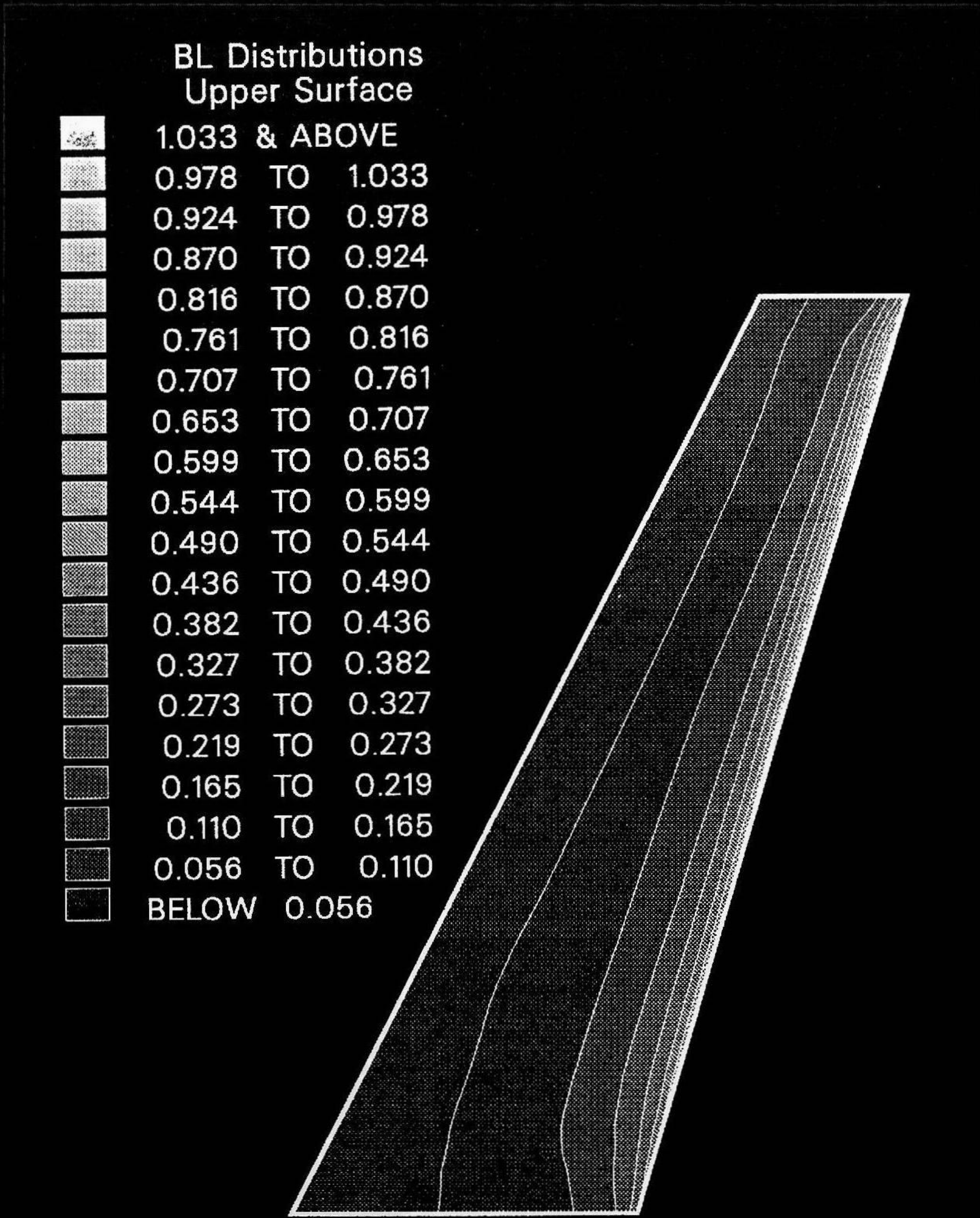

Fig. 32 Distribution of normalized boundary layer displacement thicknesses on the upper and lower surfaces of Wing-A

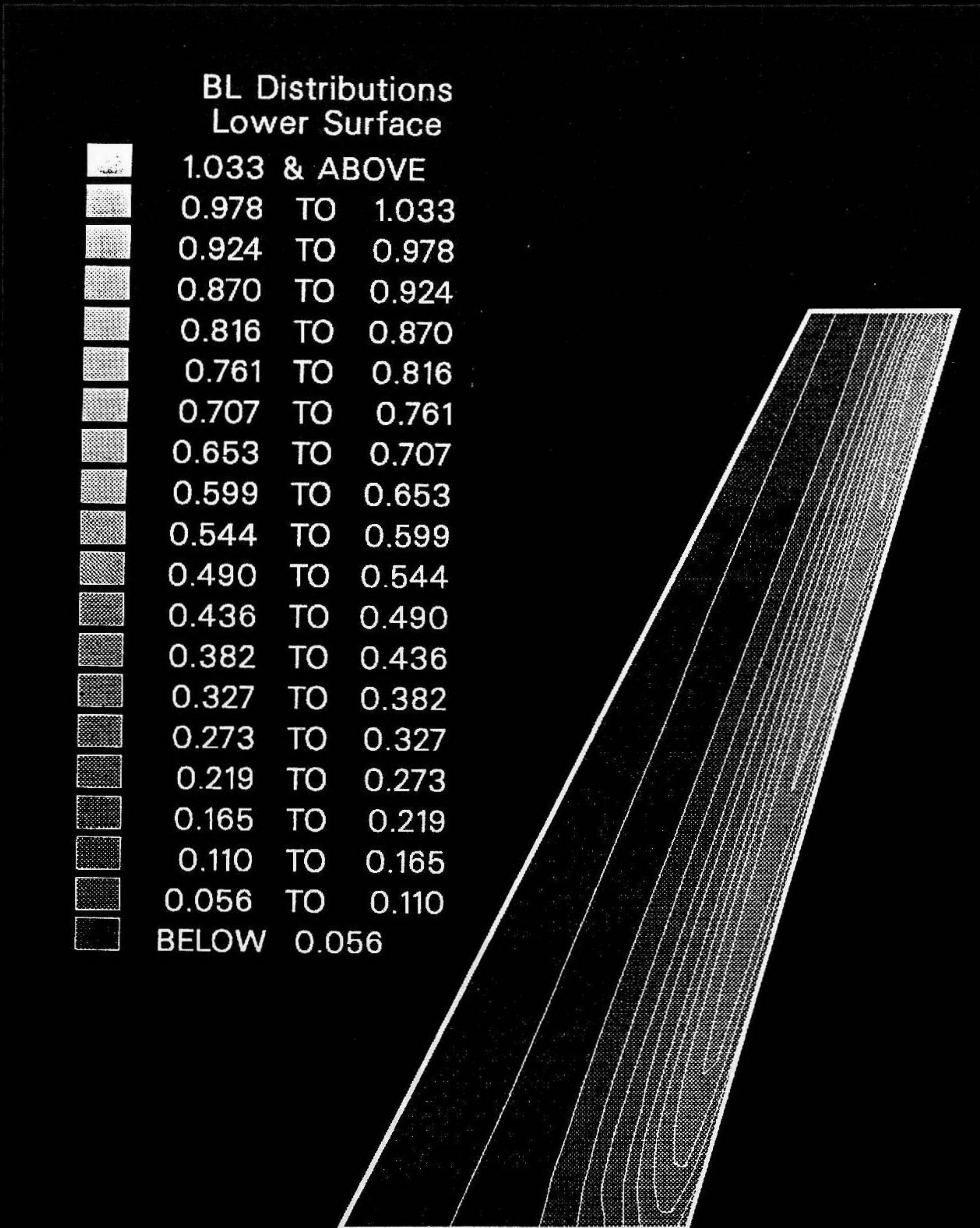

Fig. 32 Continued

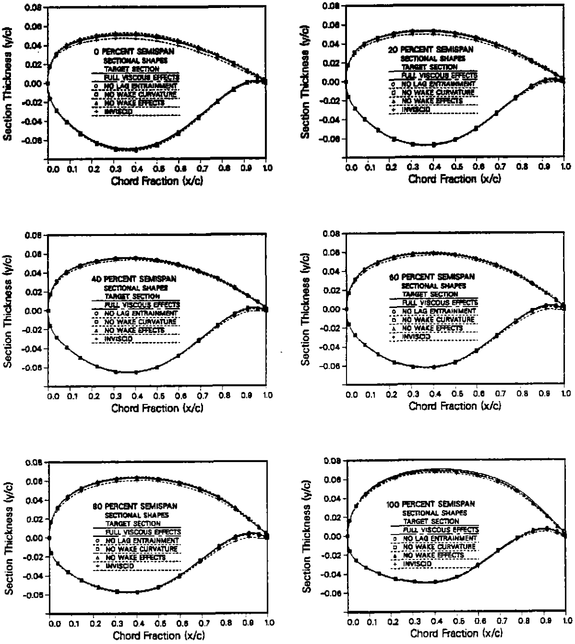

Fig. 33 Comparison of the relofted sectional shapes designed using different viscous interaction assumptions with a pressure distribution obtained from a fully viscous analysis of Lockheed Wing-A at a Re = $24\text{x}10^6$, M = .8, and an $\alpha = 2^o$

Table 1. Results from the analysis of the wings designed with different viscous interaction assumptions at a M = .8 and a Re = 24×10^6

Case	Wing C_L	Wing +Fuselage C_L	C_D
Target	.4745	.5347	.0197
Full Viscous	.4636	.5226	.0195
No Lag Entrainment	.4719	.5316	.0197
No Wake Curvature	.4636	.5226	.0195
No Wake Effects	.4605	.5194	.0193
Inviscid	.4060	.4598	.0169

The resulting wing for each case was analyzed using full viscous effects and the same iteration history. Table 1 gives a comparison of the lift and drag coefficients resulting from the analyses of these designed wings.

As can be seen from the pressure distributions shown in Fig. 34 and Table 1, the inviscidly designed wing produced 15% less lift than did the target wing. The lift usually obtained in the cove region was diminished, in this case, by the decambering of the aft portion of the wing. The thinning of the top in conjunction with the thickening of the bottom of the inviscidly designed airfoils also caused a decambering of each section, which explains the large decrement in lift produced. As shown in Fig. 35, the reason the top was thinner is because the boundary layer displacement thicknesses which are 'built' into the imposed pressure distribution were not subtracted from the inverse displacements in the inviscid design. In order to meet the trailing edge

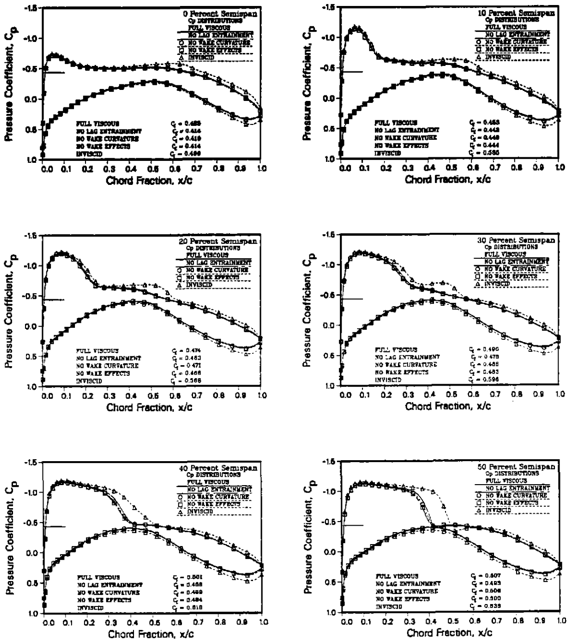

Fig. 34 Comparison of pressure distributions obtained from a viscous analysis of the Lockheed Wing-A using three different viscous interaction assumptions with a M = .8, $\alpha = 2^o$, Re = $24x10^6$

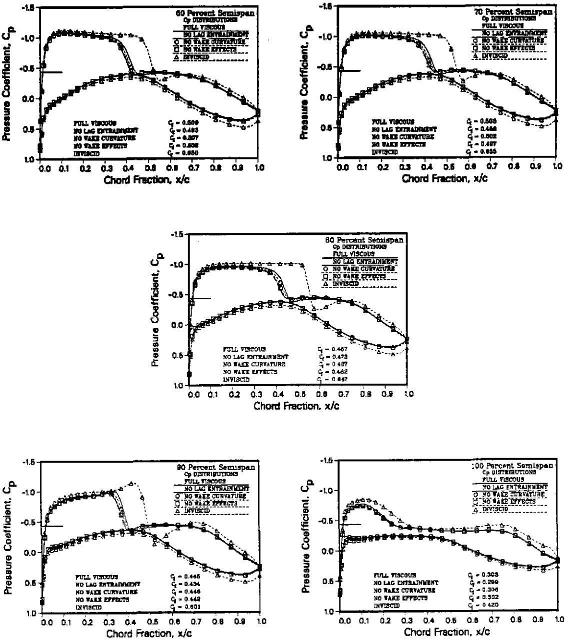

Fig. 34 Continued

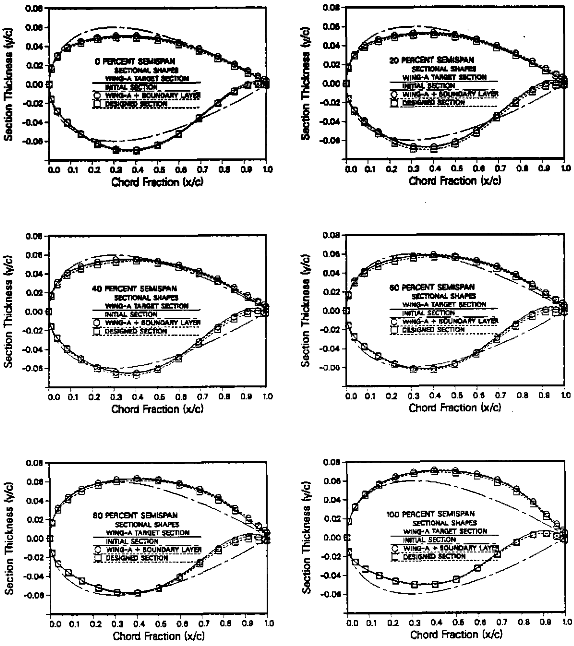

Fig. 35 Comparison of an inviscidly designed section using viscous pressures with the target and the target plus the associated boundary layer displacement thicknesses

ordinate requirement, the resulting section had to be relofted more to compensate, thus leading to a thinner section on top.

The wing lift coefficients obtained from the analyses indicate that by not using lag entrainment, a design correlating closely with the target can be better accomplished for the given sequence and number of flowfield iterations. It is suspected displacements and hence the inverse displacements may take longer to converge to the correct value as compared to excluding lag entrainment. By ignoring wake curvature and using all the other available viscous options, wings with identically slightly lower lift coefficients as compared to the targets were produced. Furthermore, wake thickness influenced the design in a slightly more profound way than did wake curvature by producing a wing with 3% less lift than the target.

As an after thought, the original wing was analyzed with each viscous option to assess its effect. The analysis results of the designed wings, shown in Fig. 36, reveal that wake curvature effects were practically negligible. This result may be due to the relatively high freestream Reynolds number of 25 million used in the comparisons. Since this Re would lead to low values of δ^* and θ, the curvature effects would also be expected to be low; Streett's case[20] used a much lower Reynolds number of 6 million. On the other hand, neglecting wake thickness and lag entrainment effects both had a decremental effect on the wing's lift, which was probably due to the forward shifting of the shock location.

The second set of design cases involved a partial wing design which extended from 30-70% semispan and began 10% aft of the leading edge of the airfoil, but the

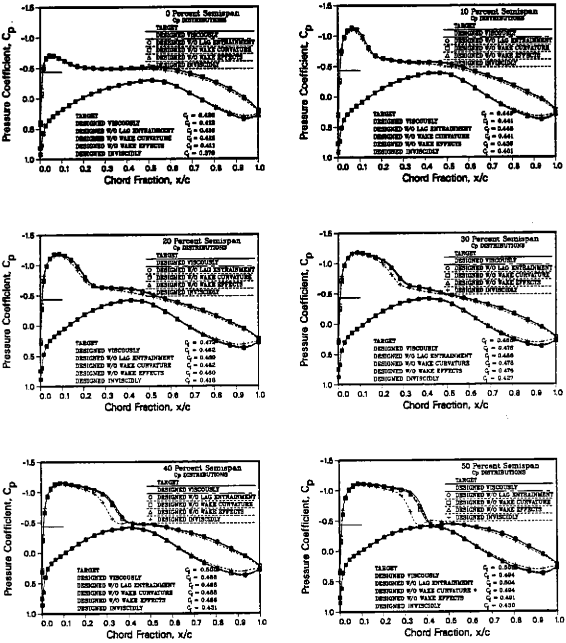

Fig. 36 Comparison of pressure distributions obtained by fully viscous analyses of the wings designed using different viscous interaction assumptions for a $M = .8$, $\alpha = 2^o$, $Re = 24x10^6$

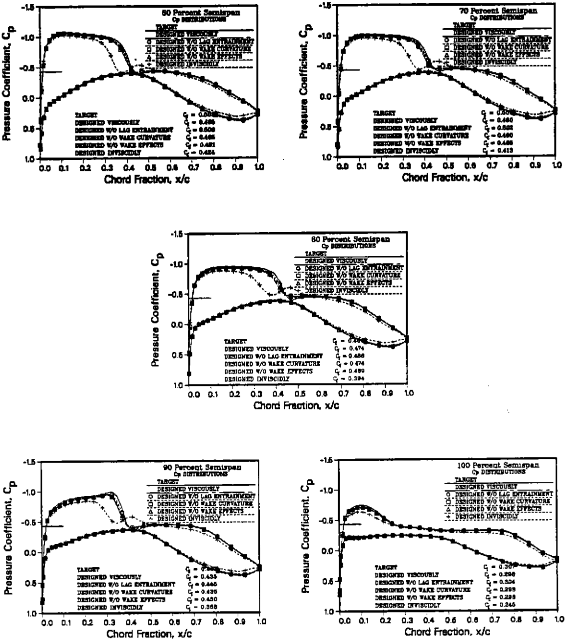

Fig. 36 Continued

inverse boundary condition was only enforced at the 30, 50 and 70% semispan station and the displacements were linearly interpolated to the stations in between. The initial airfoil section at 50% semispan was formed by thinning the supercritical target section by 6% and removing the cove region. The initial sections at the edges of the design region were the same as the target sections, while the remaining sections were obtained through linear interpolation. The results for these cases are presented in Fig. 37. For the Reynold's number chosen, neglecting wake effects seems to have had a small effect on the resulting design. The sections are a little thicker than the sections designed with full viscous effects. As noted earlier, the wake effects had relatively little effect on the pressure distributions obtained from the analysis of the target wing; but, when the boundary layer displacement thicknesses obtained were investigated, it was discovered that neglecting wake effects in the analysis produced boundary layer displacement thicknesses that were on the average 3.5% thicker at the trailing edge than those obtained from a full viscous analysis. Since the boundary layer displacement thicknesses are subtracted from the initial inverse changes to yield the hard airfoil, these larger displacement thicknesses would produce a section that was initially thinner than the target; but, after relofting the airfoil section, it would actually be thicker than the target.

The wing sections designed inviscidly are profoundly different at 30 and 70% semispan, but only slightly different at 50% semispan. The thinning of the top surface in complement with the thickening of the lower surface significantly decambered these sections. The large differences at the inboard and outboard design stations are due to

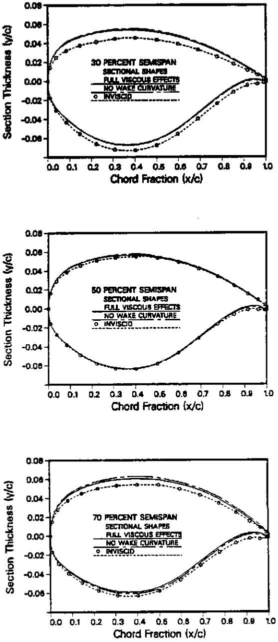

Fig. 37 Comparison of the relofted sectional shapes designed using different viscous interaction assumptions with a pressure distribution obtained from a fully viscous analysis of Lockheed Wing-A at a Re $= 24 \times 10^6$, M $= .8$, and an $\alpha = 2^o$. The design region extended from 30%-70% semispan.

the influence of the inviscid pressures outside the design region; and, the remarkable agreement in the middle of the design region, except in the cove region where the boundary layer is thick, is due to the influence of the viscous boundary condition at the edges of the design region. This observation can be verified by reviewing the previous case and noticing that the airfoils sections varied smoothly in the spanwise direction at all spanwise stations.

After the wings were designed, all three were then analyzed with full viscous effects to assess the significance of the changes made to the wing on the pressure distributions and to see how well these pressures matched the target pressures. Knowing that the wing designed with full viscous effects is correct, it is quite obvious from Fig. 38 and Table 2 that the wing designed inviscidly is quite unsatisfactory. The shock is not far enough aft and the lift produced is sometimes 20% smaller than that desired.

Based on the results of this study, it can be concluded that for the Reynold's number and Mach number chosen, wake curvature and wake thickness and lag entrainment have a very small effect on the designed airfoil sections. However, the boundary layer displacement effect has a profound effect on the section shapes and hence must be included in the design process to yield a wing which will produce the desired lift in a viscous environment.

V.2 Spanwise Grid Skewness

In the course of the present research, it was discovered that the skewness of the constant ξ grid lines leaving the tip of the wing (Fig. 39) can have a dramatic effect on

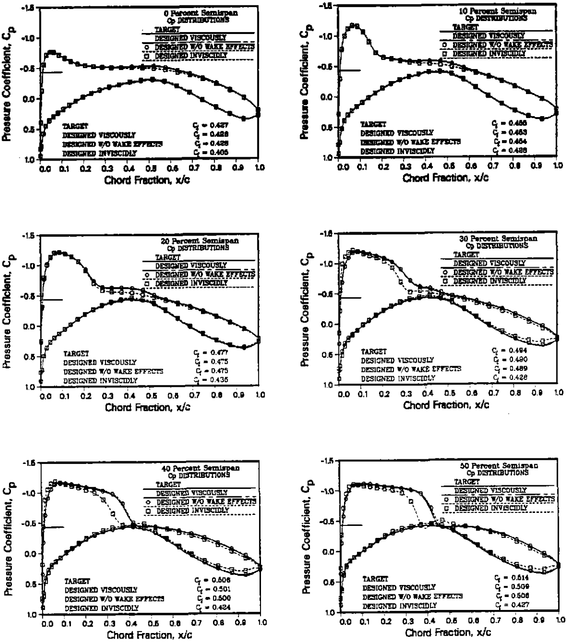

Fig. 38 Comparison of pressure distributions obtained from a viscous analysis of the Lockheed Wing-A using three different viscous interaction assumptions with a M = .8, $\alpha = 2^o$, Re = 24×10^6

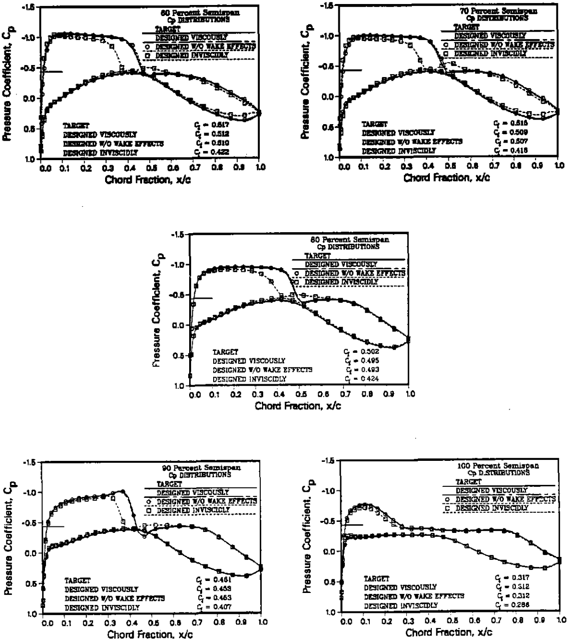

Fig. 38 Continued

Table 2. **Comparison of the total and wing lift coefficient obtained from a fully viscous analysis of the wings designed using different viscous interaction assumptions at a M = .8 and a Re = 24 $\times$ 10^6**

Lift Coefficient	Target	Full Viscous	No Wake Design	Inviscid Design
C_L	.514	.509	.506	.427
Wing C_L	.483	.478	.477	.419

the design of the sections near the wing tip. As can be seen in Fig. 40, if the grid was significantly skewed and the input pressures were calculated on an nonskewed grid, it was impossible to obtain the correct airfoil shapes in the tip region. This difficulty is due to the large differences in pressures between the skewed and nonskewed grid. These pressure profile differences are shown in Fig. 41. As shown in the figure, the grid skewness has caused the shock location to move further aft. Although the skewness of the grid was quite extreme in this case, these results affirm the need for smoothly varying grids in wing design, at least in the spanwise direction. It should be noted though, that if the input pressures were obtained on a skewed grid and used in the design process with a skewed grid then the tip sections were well resolved. In summary then, if the pressures calculated on an nonskewed grid are correct or closer to real pressures encountered in flight, then it would be wise to ensure that the grid is smoothly varying.

V.3 Wing Planform Effects

Three cases were attempted to roughly delimit the applicable range of aspect ratios and leading edge sweep angles for which good results could be obtained with

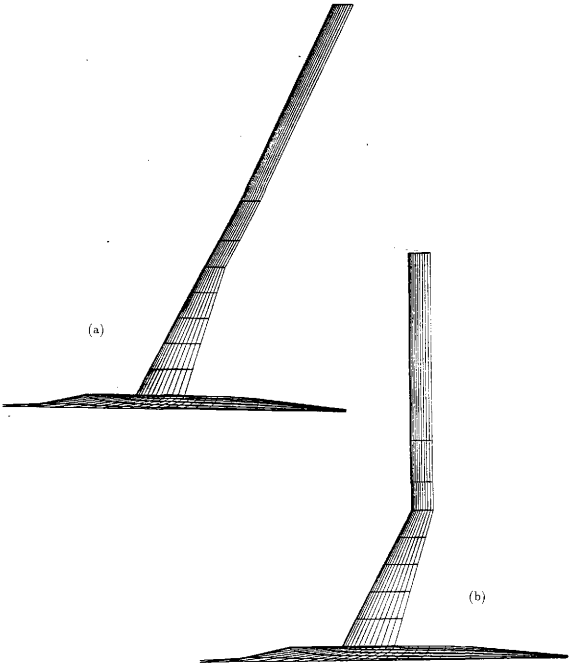

Fig. 39 Comparison between a fairly nonskewed (a) and skewed grid (b)

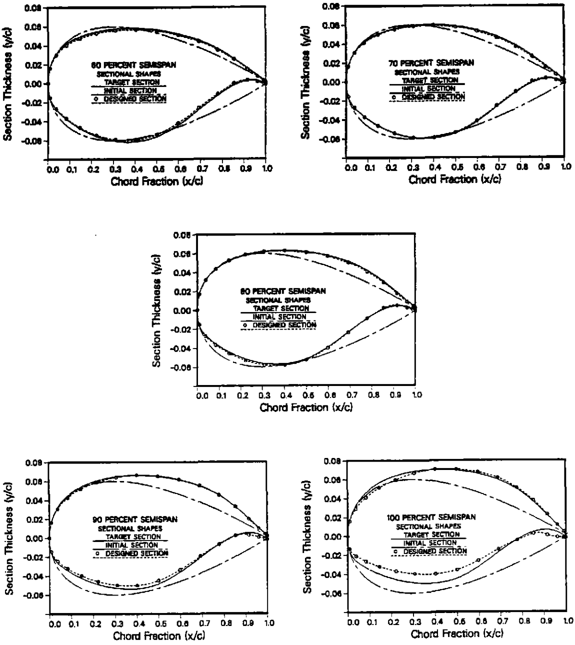

Fig. 40 Sections designed with a skewed grid using pressures obtained from an analysis on a nonskewed grid

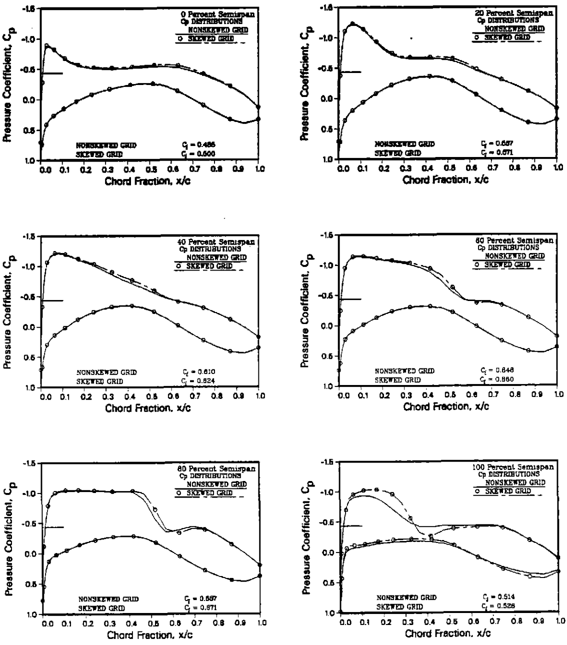

Fig. 41 Comparison of a pressure distribution obtained from an analysis of a skewed grid with one obtained from an analysis of a nonskewed grid

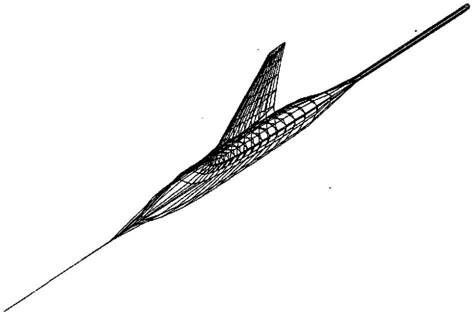

Fig. 42 Grid generated about Wing-C with an incompatible root section and fuselage cross section

the present design method. These included Lockheed Wings A, B and C. These wings have aspect ratios of 8, 3.8, and 2.6, leading edge sweep angles of 27, 35, and 45 degrees and taper ratios of .4, .4, and .3 respectively. The target pressure distributions were obtained by a direct analysis of the target wings in an inviscid environment. The initial section for Wing-A was a NACA 0012, while a NACA 0006 was used for Wing-B. The original section was used with Wing-C due to the difficulty of the case. Also for Wing-C, as opposed to the circular cross-section, an elliptical cross section of the fuselage was used to provide a flatter surface for the grid generation package. The circular cross-section combined with the large relative thickness of the root section compared with the width of the fuselage played havoc on the grid at the root, as can be seen in Fig. 42

In order to better understand the flow about each wing, the corresponding velocity vectors on the surface of each wing were plotted, as shown in Figs. 43–45. As should be expected, the spanwise component of the flow increases as the aspect ratio decreases and sweep increases. It is also interesting that there seems to be an inboard component of the flow for all three cases on the upper surfaces aft of the leading edge. This inboard flow may be attributed to the effect of the fuselage and the wing tip vortex. These effects can be seen most readily by viewing a cross section of the flow just aft of the wing tip shown in Fig. 46. The vortex near the tip of the wing is quite evident, and flow tangency at the fuselage also contributes to the spanwise component of the flow. The momentum of the air over the tip must dominate the flow, since, as seen in Figs. 47–49, the spanwise pressure gradients appear to encourage the air to move outboard. However, in order to determine whether the flow actually traveled in the inboard direction, it would be necessary to plot the actual streamlines of the flow over the surface of the wing.

The design region for Wing-A and Wing-B extended from 10-100% semispan and began 5% and 2.5% aft of the leading edge, respectively. Computations were performed on a fine grid. Results for Wing-A are shown in Fig. 50, while results for Wing-B are shown in Fig. 51. As can be seen the designed and target sections for both wings are in excellent agreement in the interior of the design region and closely match at the edges of the design region.

In the case of Wing-C, the section shapes should not have changed with the application of the inverse boundary condition. But, because of the large amount

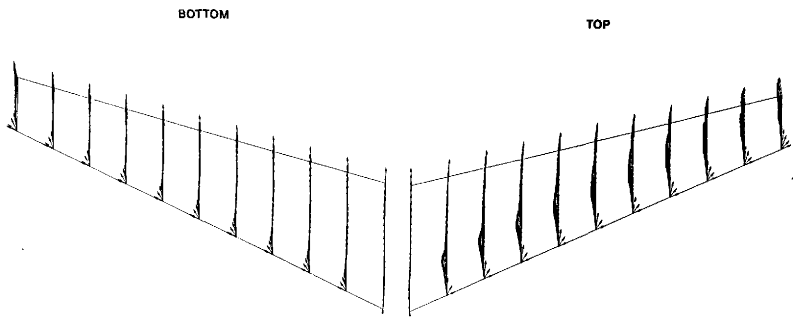

Fig. 43 Surface velocity vectors for Lockheed Wing-A on the upper and lower surface

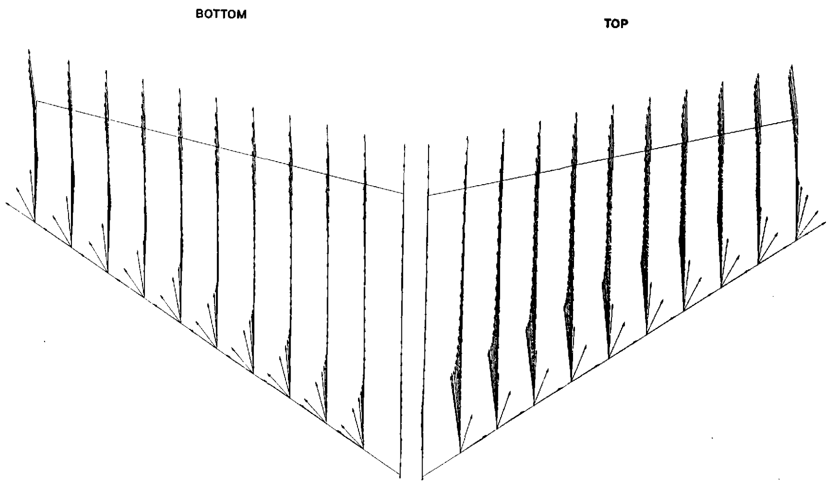

Fig. 44 Surface velocity vectors for Lockheed Wing-B on the upper and lower surface

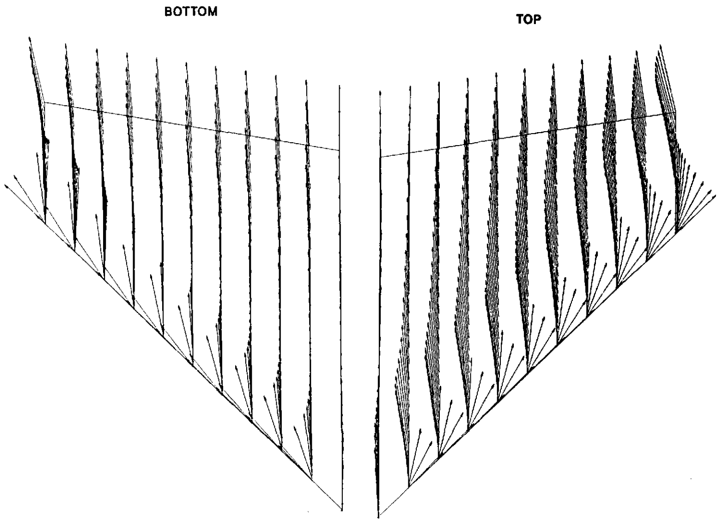

Fig. 45 Surface velocity vectors for Lockheed Wing-C on the upper and lower surface

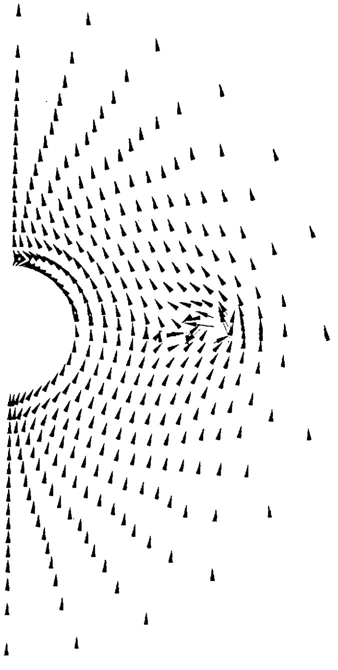

Fig. 46 Cross-section of the flow in the x-y plane for Lockheed Wing-C

Fig. 47 Pressure contour plot for Lockheed Wing-A $M = .8$, $\alpha = 2^o$

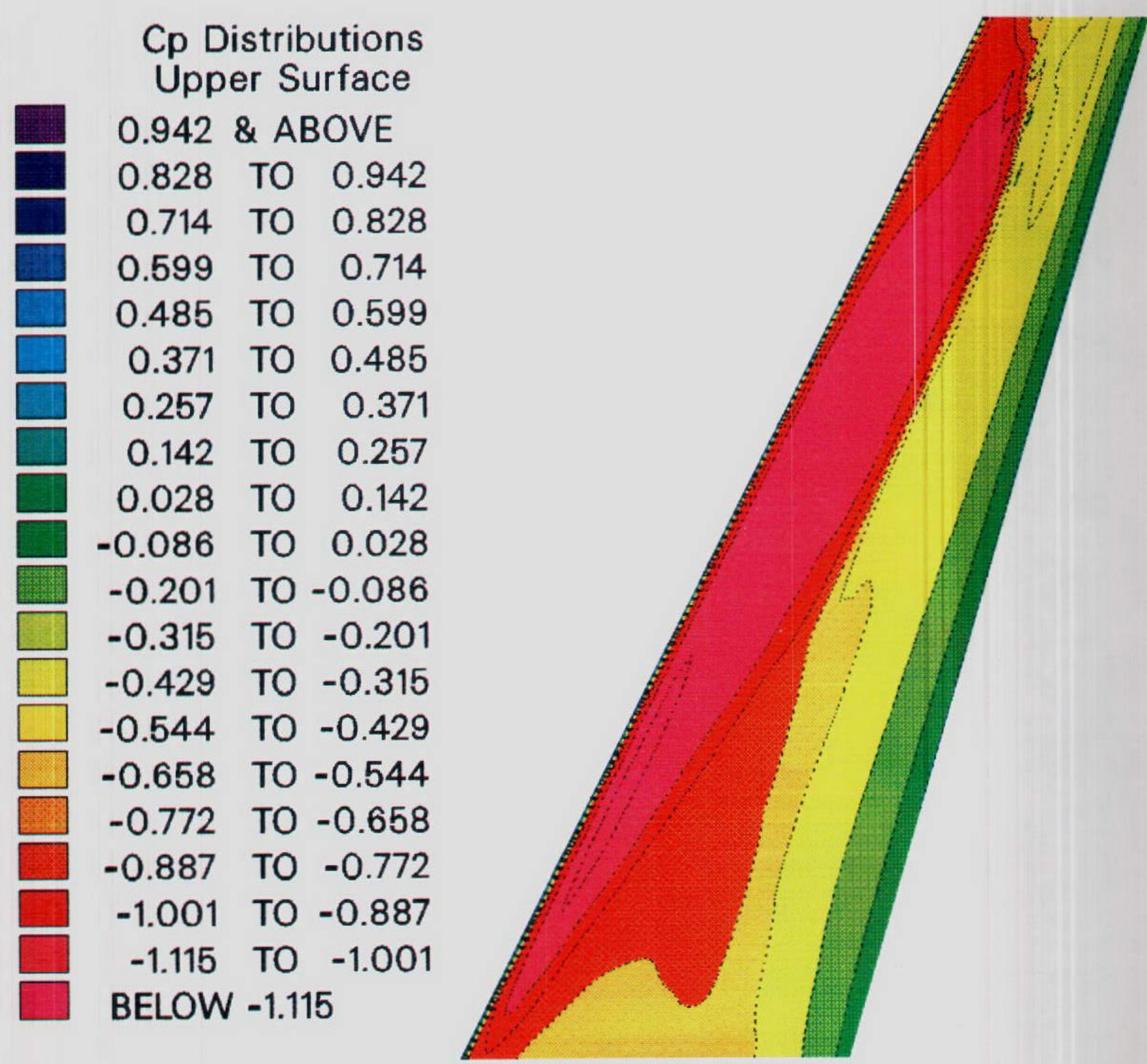
Cp Distributions
Upper Surface
0.942 & ABOVE
0.828 TO 0.942
0.714 TO 0.828
0.599 TO 0.714
0.485 TO 0.599
0.371 TO 0.485
0.257 TO 0.371
0.142 TO 0.257
0.028 TO 0.142
-0.086 TO 0.028
-0.201 TO -0.086
-0.315 TO -0.201
-0.429 TO -0.315
-0.544 TO -0.429
-0.658 TO -0.544
-0.772 TO -0.658
-0.887 TO -0.772
-1.001 TO -0.887
-1.115 TO -1.001
BELOW -1.115

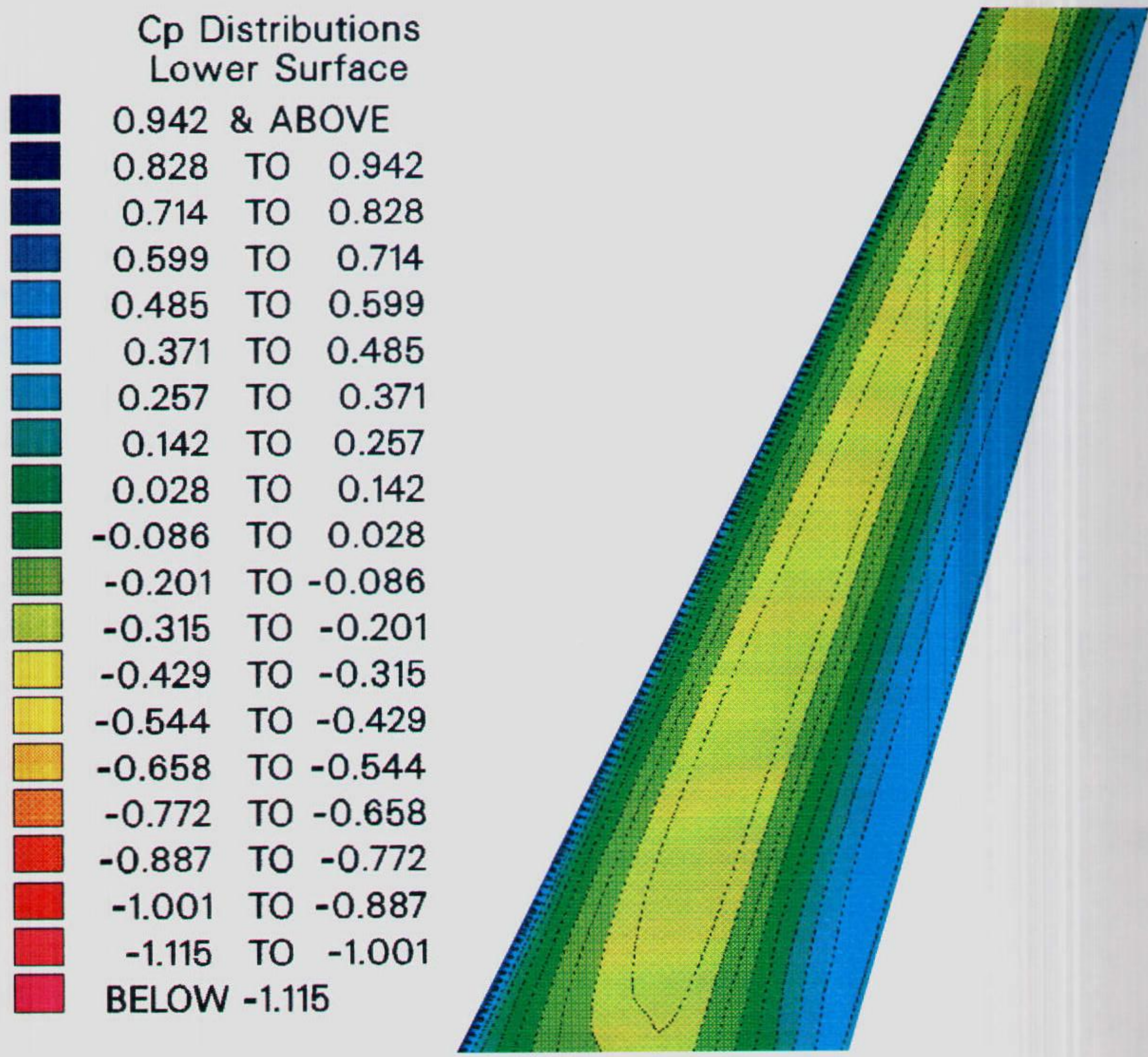

Cp Distributions
Lower Surface
0.942 & ABOVE
0.828 TO 0.942
0.714 TO 0.828
0.599 TO 0.714
0.485 TO 0.599
0.371 TO 0.485
0.257 TO 0.371
0.142 TO 0.257
0.028 TO 0.142
-0.086 TO 0.028
-0.201 TO -0.086
-0.315 TO -0.201
-0.429 TO -0.315
-0.544 TO -0.429
-0.658 TO -0.544
-0.772 TO -0.658
-0.887 TO -0.772
-1.001 TO -0.887
-1.115 TO -1.001
BELOW -1.115

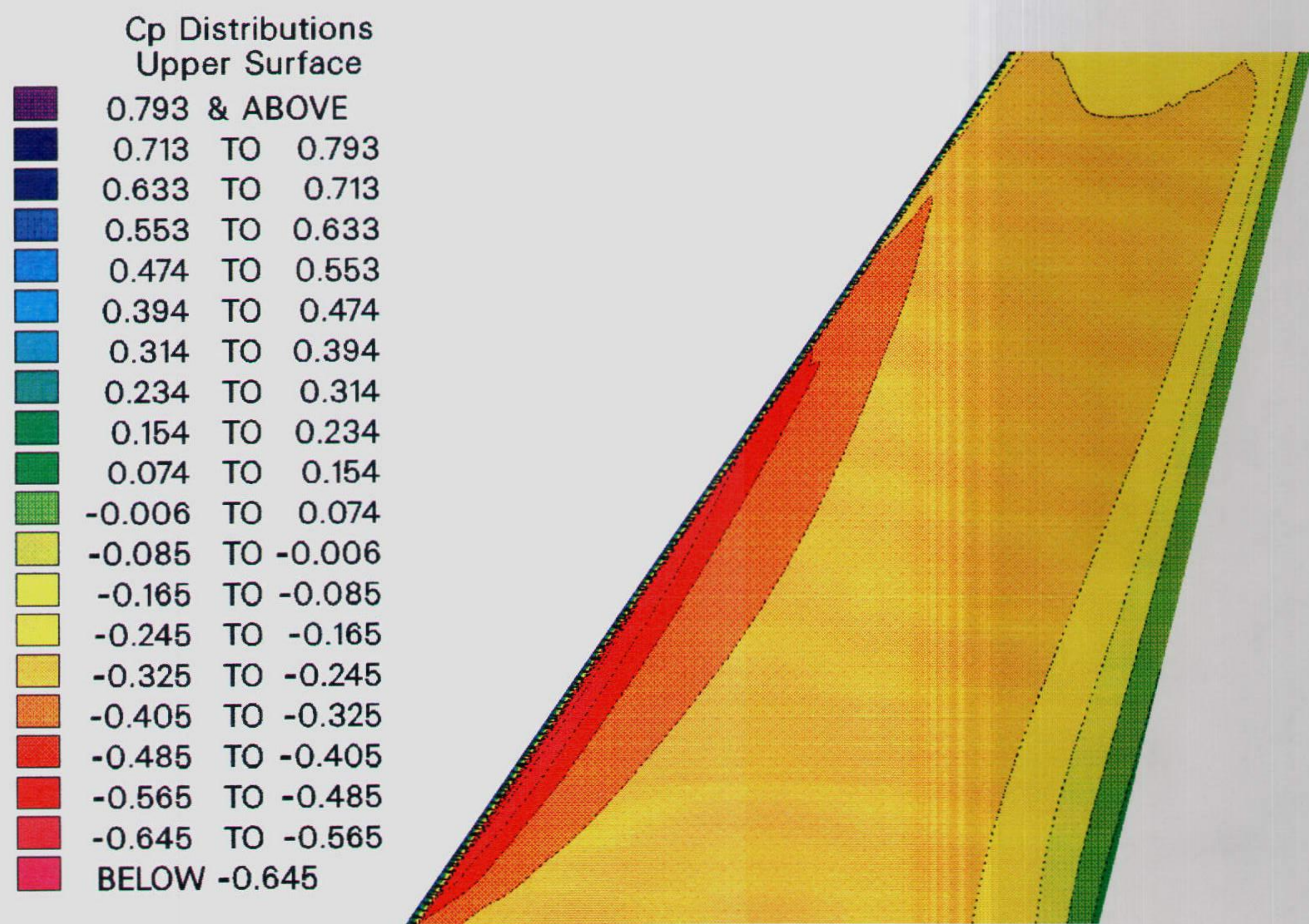
Cp Distributions
Upper Surface
0.793 & ABOVE
0.713 TO 0.793
0.633 TO 0.713
0.553 TO 0.633
0.474 TO 0.553
0.394 TO 0.474
0.314 TO 0.394
0.234 TO 0.314
0.154 TO 0.234
0.074 TO 0.154
-0.006 TO 0.074
-0.085 TO -0.006
-0.165 TO -0.085
-0.245 TO -0.165
-0.325 TO -0.245
-0.405 TO -0.325
-0.485 TO -0.405
-0.565 TO -0.485
-0.645 TO -0.565
BELOW -0.645

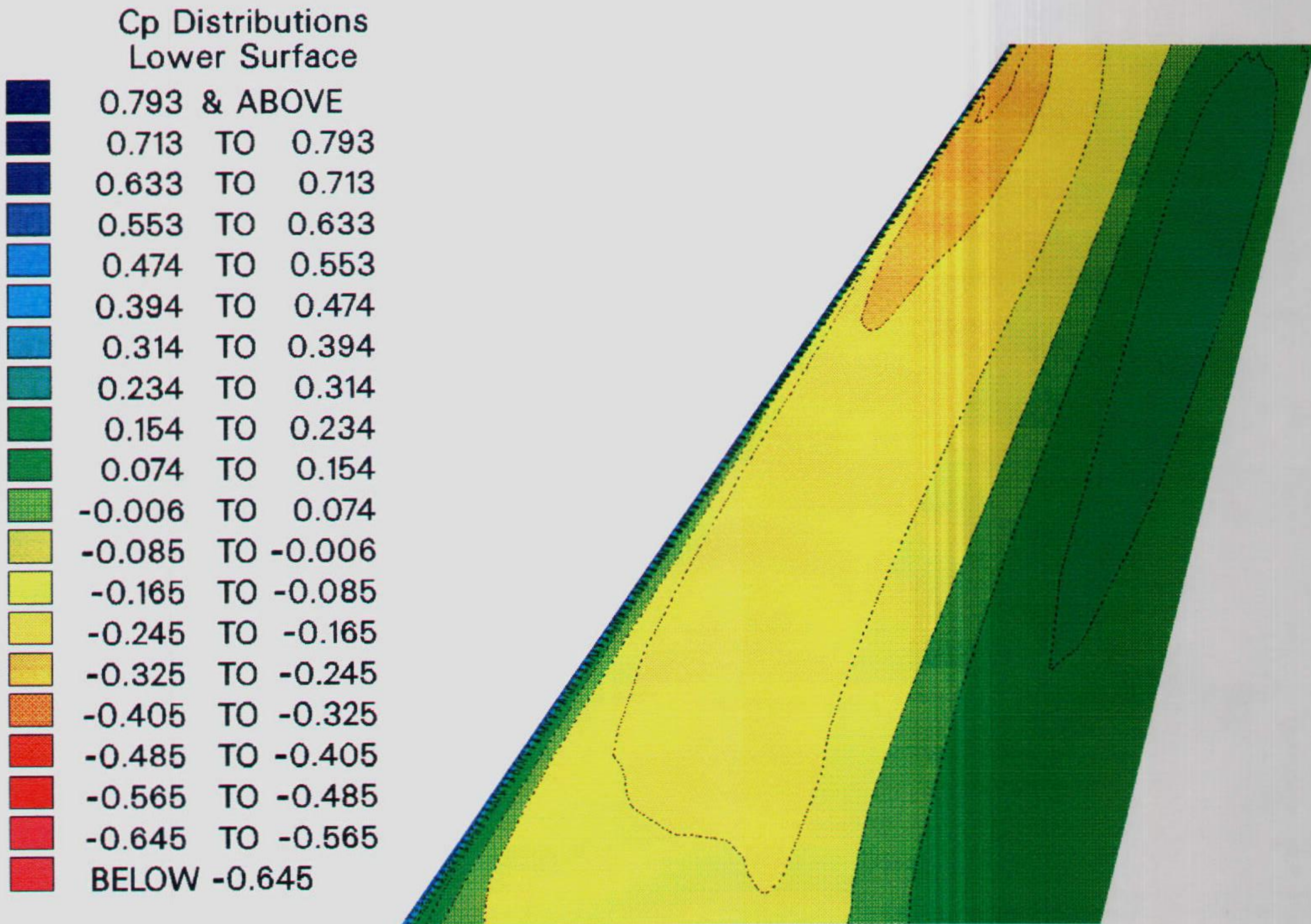
Cp Distributions
Lower Surface
0.793 & ABOVE
0.713 TO 0.793
0.633 TO 0.713
0.553 TO 0.633
0.474 TO 0.553
0.394 TO 0.474
0.314 TO 0.394
0.234 TO 0.314
0.154 TO 0.234
0.074 TO 0.154
-0.006 TO 0.074
-0.085 TO -0.006
-0.165 TO -0.085
-0.245 TO -0.165
-0.325 TO -0.245
-0.405 TO -0.325
-0.485 TO -0.405
-0.565 TO -0.485
-0.645 TO -0.565
BELOW -0.645

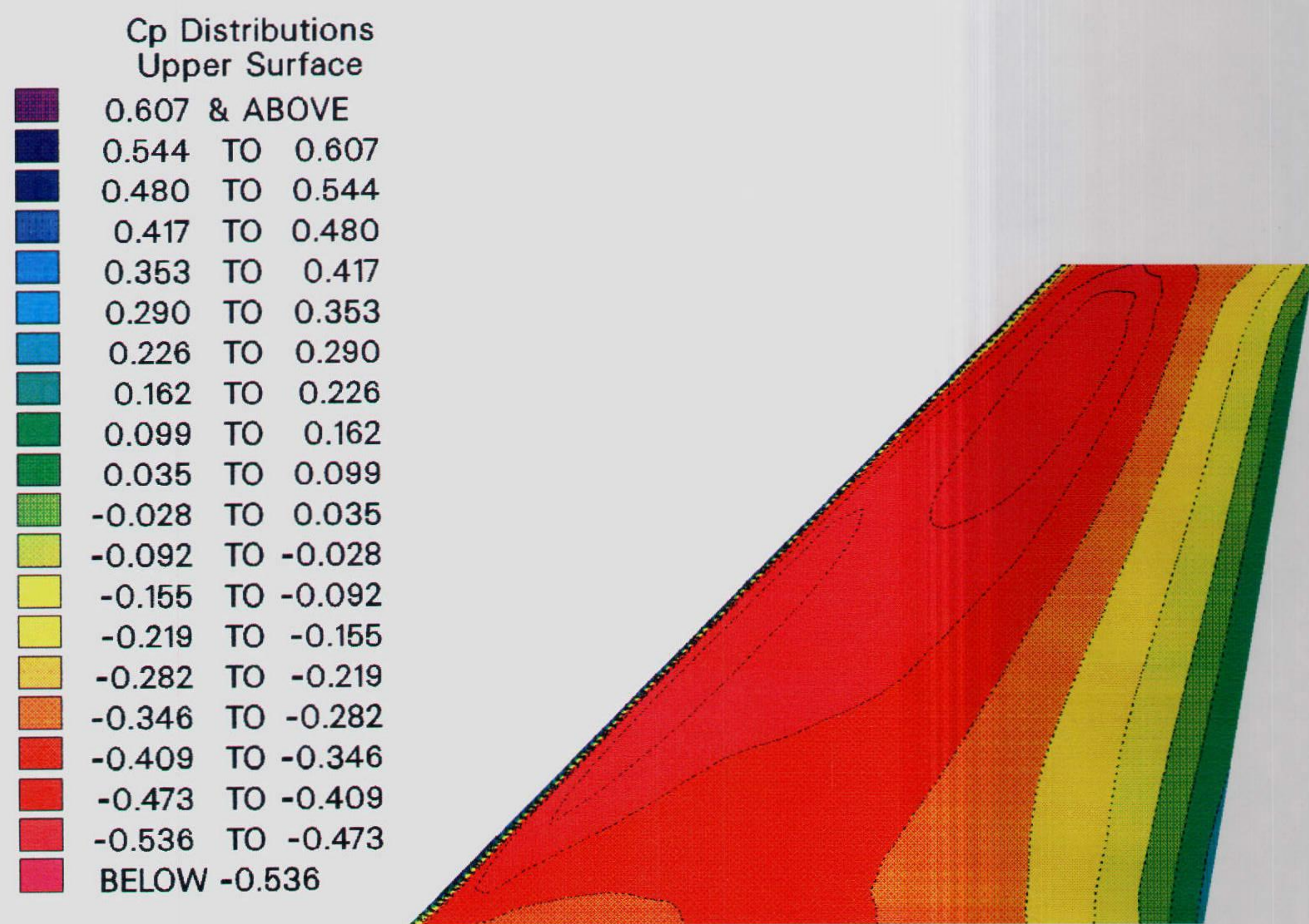

Cp Distributions
Upper Surface
0.607 & ABOVE
0.544 TO 0.607
0.480 TO 0.544
0.417 TO 0.480
0.353 TO 0.417
0.290 TO 0.353
0.226 TO 0.290
0.162 TO 0.226
0.099 TO 0.162
0.035 TO 0.099
-0.028 TO 0.035
-0.092 TO -0.028
-0.155 TO -0.092
-0.219 TO -0.155
-0.282 TO -0.219
-0.346 TO -0.282
-0.409 TO -0.346
-0.473 TO -0.409
-0.536 TO -0.473
BELOW -0.536

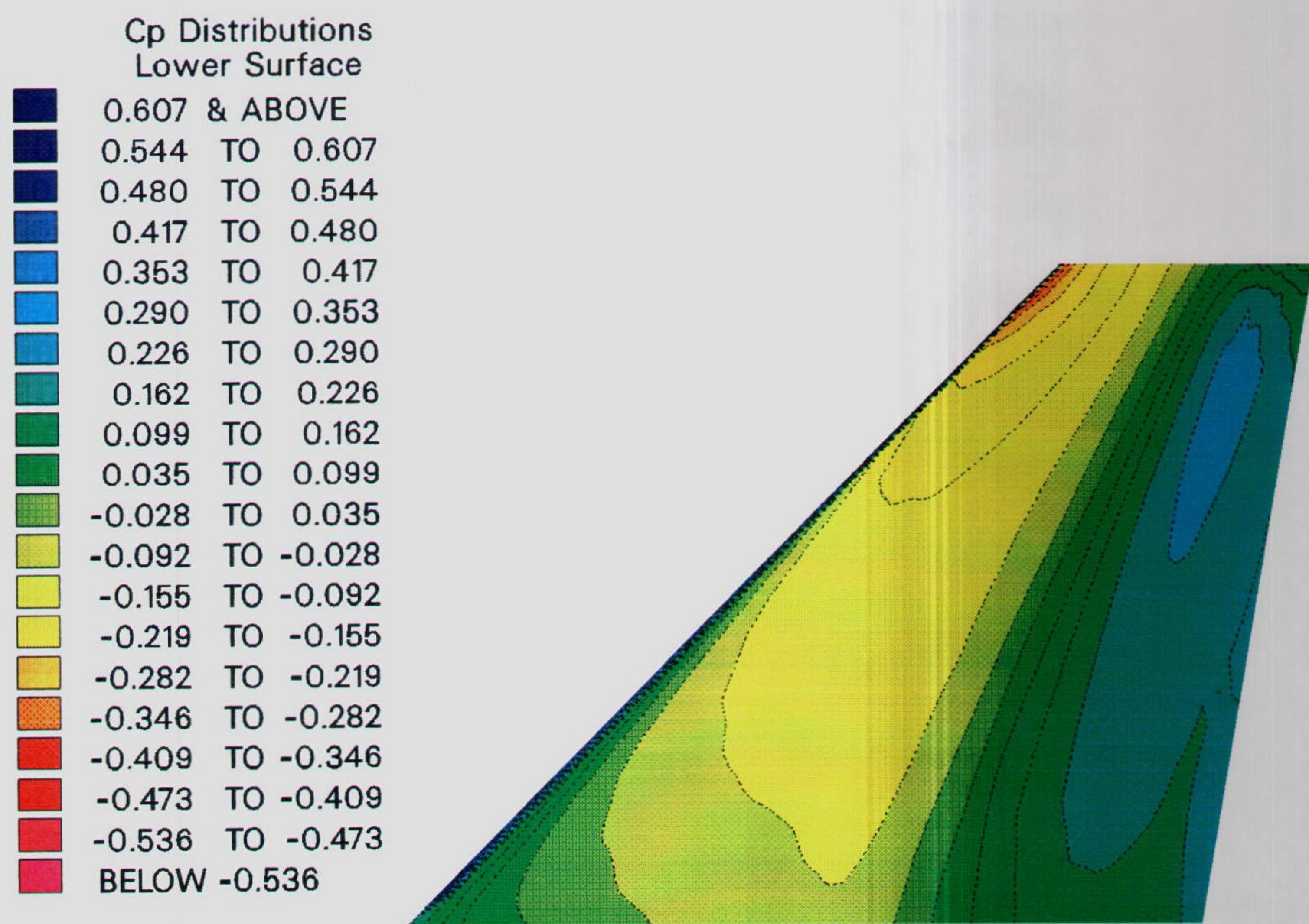
Cp Distributions
Lower Surface
0.607 & ABOVE
0.544 TO 0.607
0.480 TO 0.544
0.417 TO 0.480
0.353 TO 0.417
0.290 TO 0.353
0.226 TO 0.290
0.162 TO 0.226
0.099 TO 0.162
0.035 TO 0.099
-0.028 TO 0.035
-0.092 TO -0.028
-0.155 TO -0.092
-0.219 TO -0.155
-0.282 TO -0.219
-0.346 TO -0.282
-0.409 TO -0.346
-0.473 TO -0.409
-0.536 TO -0.473
BELOW -0.536

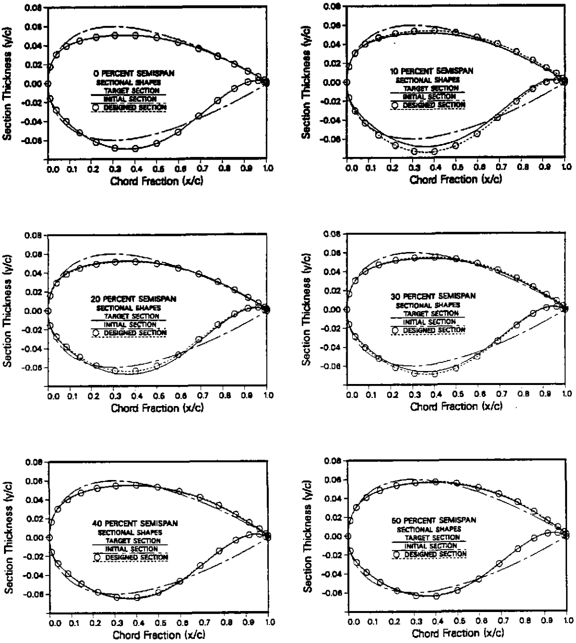

Fig. 50 Comparison of the designed sections with the targets and the initial sections for a fine grid case using Lockheed Wing-A

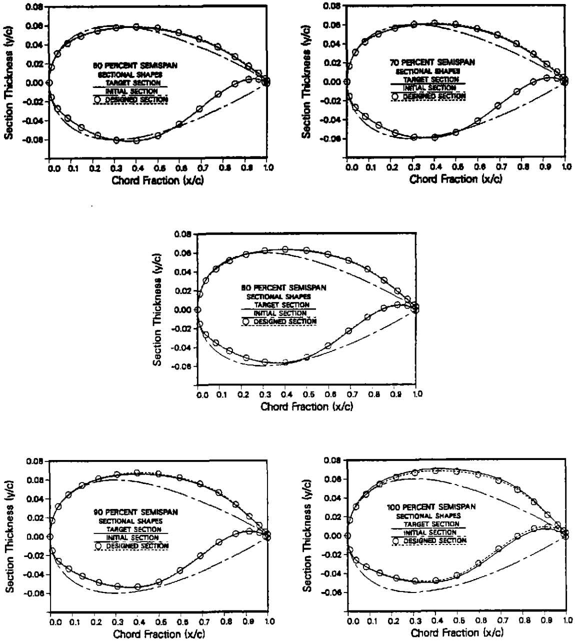

Fig. 50 Continued

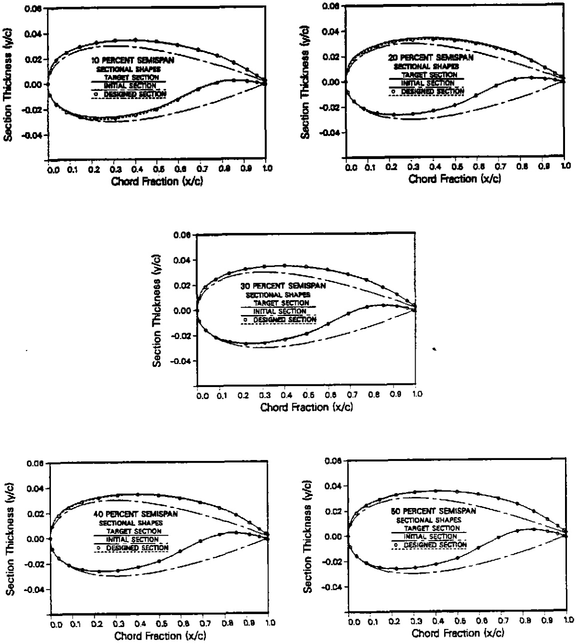

Fig. 51 Comparison of the designed sections with the targets and the initial sections for a fine grid case using Lockheed Wing-B and a design region beginning at 2.5% aft of the leading edge

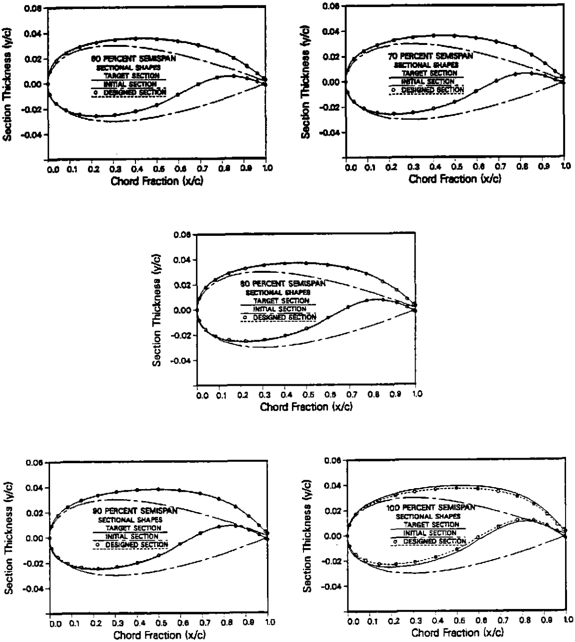

Fig. 51 Continued

of spanwise flow and the associated spanwise gradients for Wing-C, the spanwise oscillation effect could not be overcome with any of the present remedies. Further information about this case was obtained by using the Type II method and not relofting the section shapes. The results for such a converging fine grid case are shown in Fig. 52. The first design station at 18% semispan is too thick on the upper surface as compared to the target. This discrepancy is again due to the over prediction of the residual at the first station due to the initial mismatch in the potentials in the spanwise direction, and, hence, to large spanwise gradients of the potential. The errors diminish as the tip is approached, but are always relatively large in the trailing edge region due to the difficulty in accurately imposing the inverse boundary condition near the trailing edge for this case. If an attempt were made to converge this case further by continuously relofting the shapes to meet the trailing edge ordinate, the same spanwise oscillation problem would again occur. However, non-relofted results such as in Fig. 52 would be very useful for preliminary design studies.

V.4 Initial Profile Effects

One of the disadvantages of the direct-inverse method is that *a priori* knowledge about the correct shape of the leading edge must be known to achieve suitable airfoil shapes and desired trailing edge thickness. Relofting does alleviate this disadvantage to a large degree; but it will not, in general, produce a leading edge that will yield the desired pressure distribution at the leading edge if the inverse boundary condition is by necessity applied too far aft. It was thought that because FLO-30's grid package

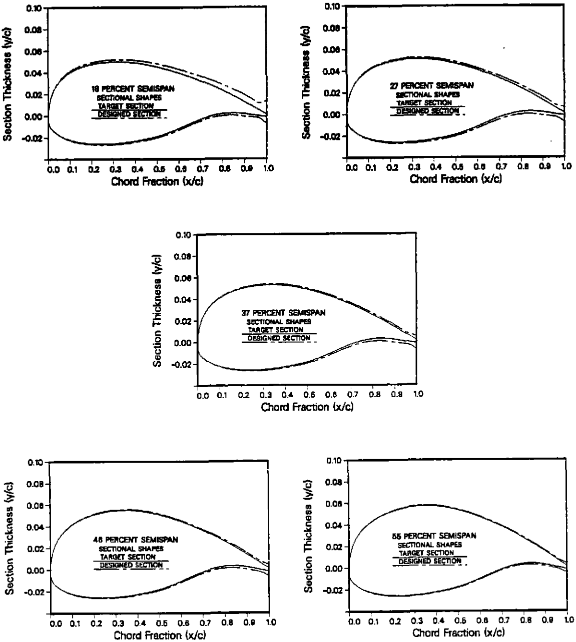

Fig. 52 Comparison of the designed section with the target for an unrelofted fine grid case using Lockheed Wing-C

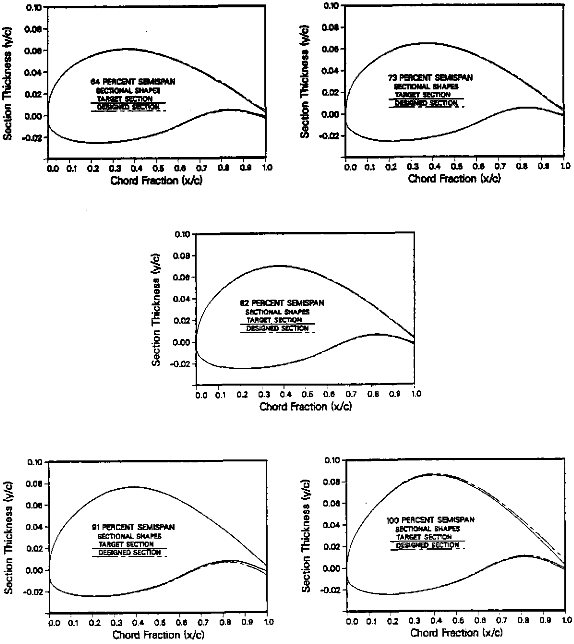

Fig. 52 Continued

clusters grid lines close to the leading edge of the airfoil, that the design could be started quite close to the leading edge, thus relieving the designer of the difficulty of choosing a correct nose shape. Two test cases were conducted to investigate the dependence of the final design on the initial airfoil section. Both used Lockheed Wing-A at the same conditions mentioned earlier for the viscous study. For the first case, the initial airfoils were the same as those in the viscous study. These airfoils all had leading edges which were in the same family as the target section. The design began 10% aft of the leading edge. In the second case, NACA 0012 sections were used at all the design stations; here, the leading edge of these sections were not in the same family as the target airfoil sections. For this case, the pressure boundary condition began 4% aft of the leading edge. Referring to Fig. 53, it can be seen that although slightly better results were obtained near the leading edge for the first case, that the airfoils designed were fairly insensitive to the initial section.

V.4.1 Direct-inverse interface proximity to leading edge

Since experience with the method has shown that the closer the inverse boundary condition is applied to the leading edge, the longer it takes for the solution to converge, it was of interest to determine how the location of the direct-inverse interface affected the final design and the resulting pressure distributions. This study was accomplished with the aid of the previously discussed Wing-B case, whose design region began at 2.5% chord, and an inviscid design of Wing-B also with NACA 0006 sections as the initial geometry. With the second case, the design was started at 5% chord from the leading edge; and, the input pressures were obtained from an inviscid

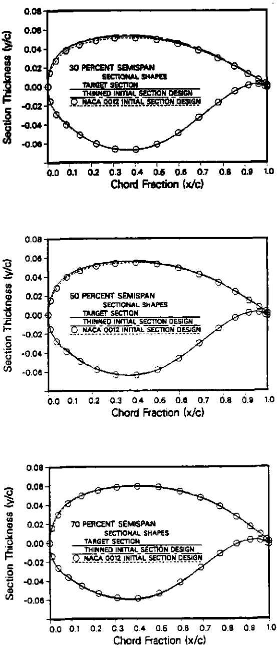

Fig. 53 Comparison of sections designed using two different initial sections

analysis of Wing-B. Since the design pressure distributions were consistent in both of these cases, the fact that one was a viscous design and the other an inviscid design is not important here.

Some representative samples of the resulting section shapes for the second case are shown in Fig. 54. The resulting wings were analyzed under the same conditions that the original input pressure distributions were obtained. Representative samples of the resulting pressure distributions are compared to their respective target distributions in Figs. 55,56. As can be seen, the wing whose design began 2.5% aft captured the suction peek at the leading edge, while the other case, which began at 5% aft of the leading edge, did not.

When designing near (less than 5%) the leading edge, the solution sometimes began to slightly diverge or ceased converging. Usually the design could be converged to the point where there was only a maximum change in the surface of .1-.2% chord. This was more a problem on the fine grid than on the medium. If it was necessary to converge it further, the beginning of the design region was moved aft. This observation is important because if it is necessary to begin the design close to the leading edge to properly determine the shape of the nose, a successful design may be accomplished by beginning the design as close to the leading edge as desired or is possible, then moving the beginning of the design region aft as the solution approaches the last stages of convergence. This method not only frees the designer from the task of choosing the correct leading edge shape, but it should also accelerate the convergence of the design considerably.

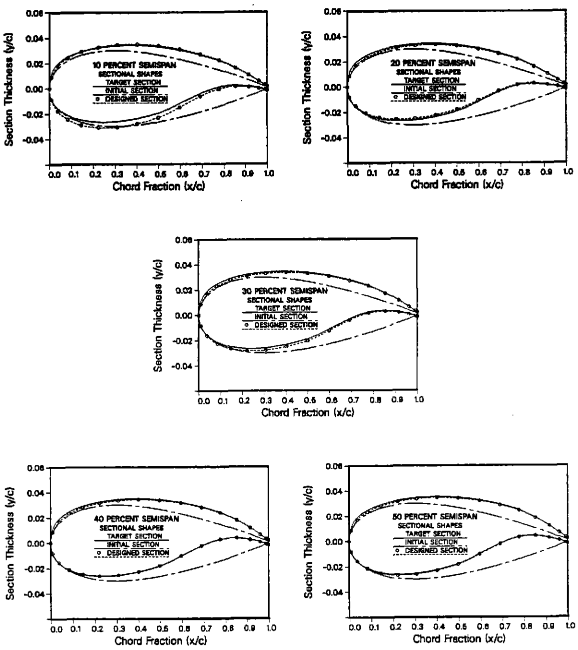

Fig. 54 Comparison of the designed sections with the targets and the initial sections for a fine grid case using Lockheed Wing-B and a design region beginning at 5.0% aft of the leading edge.

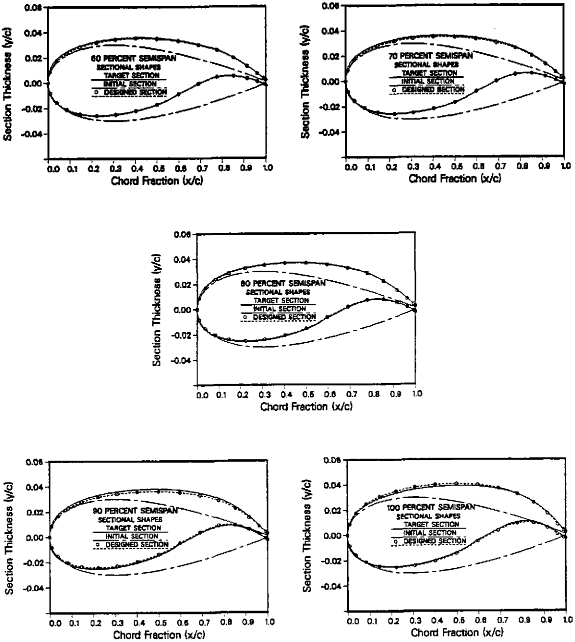

Fig. 54 Continued

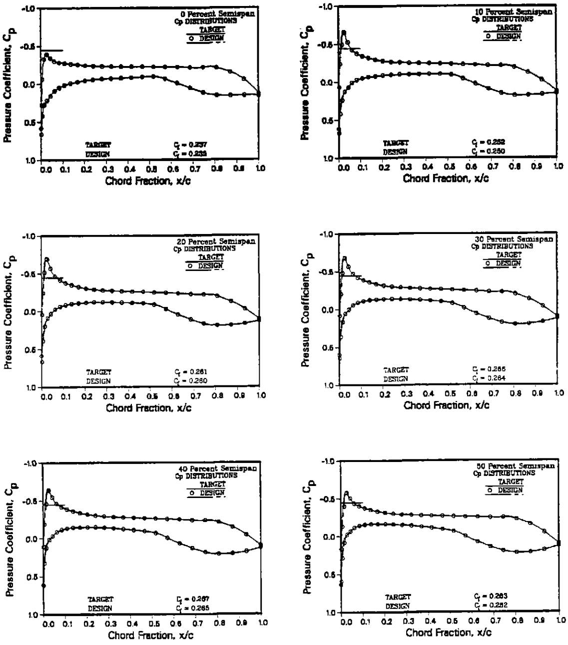

Fig. 55 Comparison of the pressure distributions obtained from an analysis of the Wing-B design, which had a design region that began 2.5% aft of the leading edge, with the target pressure distributions

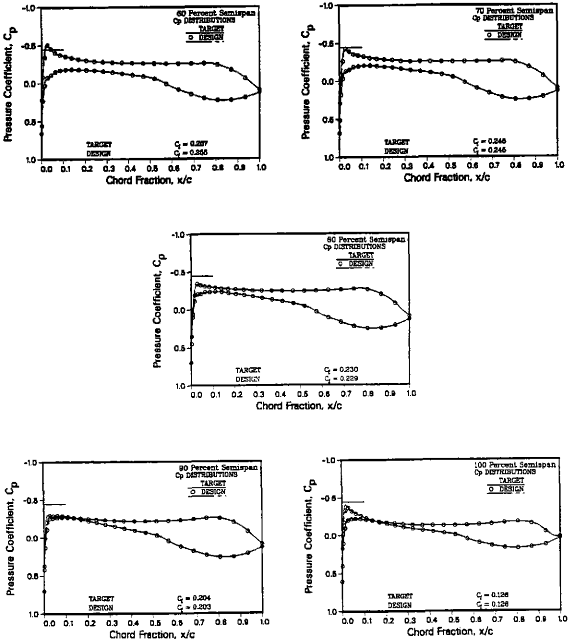

Fig. 55 Continued

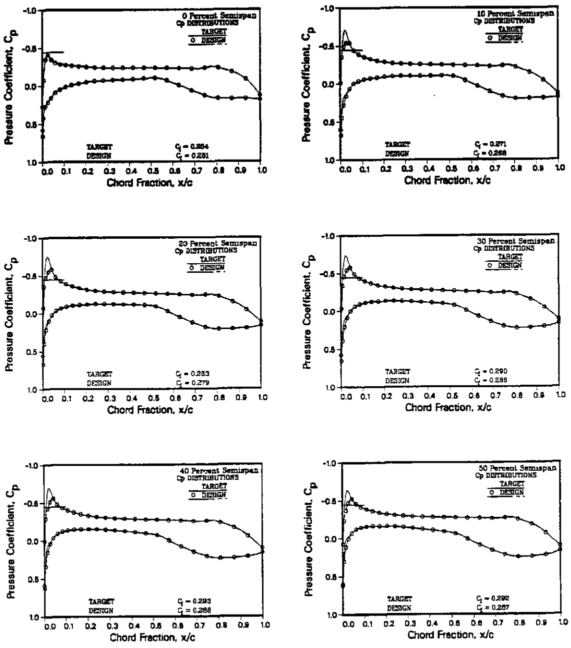

Fig. 56 Comparison of the pressure distributions obtained from an analysis of the Wing-B design, which had a design region that began 5.0% aft of the leading edge, with the target pressure distributions

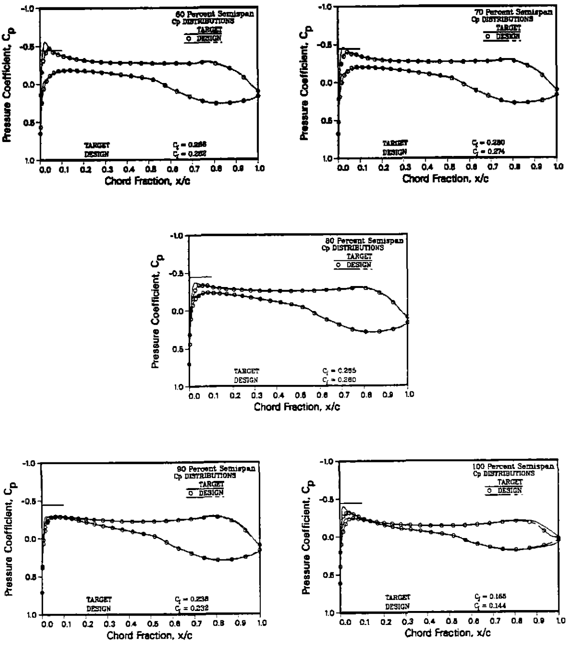

Fig. 56 Continued

Because of the leading edge clustering of grid points in TAW5D, successful designs have been accomplished on the medium grid with the chordwise direct-inverse junction beginning just aft of the stagnation point on the lower surface. If the pressure boundary condition is applied upstream of the stagnation point, major difficulties arise when an attempt is made to integrate past this point of singularity, since the slope, $\frac{V}{U}$, is indeterminate there.

For the case shown in Fig. 57 , the design was begun 1% aft of the leading edge, but in retrospect, it could have begun close to .3% aft of the leading edge since the converged stagnation point was located about .2% aft. Notice how precisely the designed surfaces can be computed when compared to the targets outboard of the first design station. This case effectively demonstrates that since the design region can be extended extremely close to the leading edge with TAW5D, the fact that the pressure boundary condition can only be applied aft of the leading edge is a very small shortcoming of this direct-inverse method.

V.5 Pressure Distribution Compatibility

Since a designer might not readily have available an input pressure distribution compatible with the design freestream Mach number, the effect of designing a wing at one Mach number using a pressure distribution obtained from an analysis of the wing at a different Mach number was investigated. The Wing-A planform was used throughout this portion of the study. NACA 0012 sections were used as the targets and NACA 0006 sections were used as the initial sections in the design. The entire

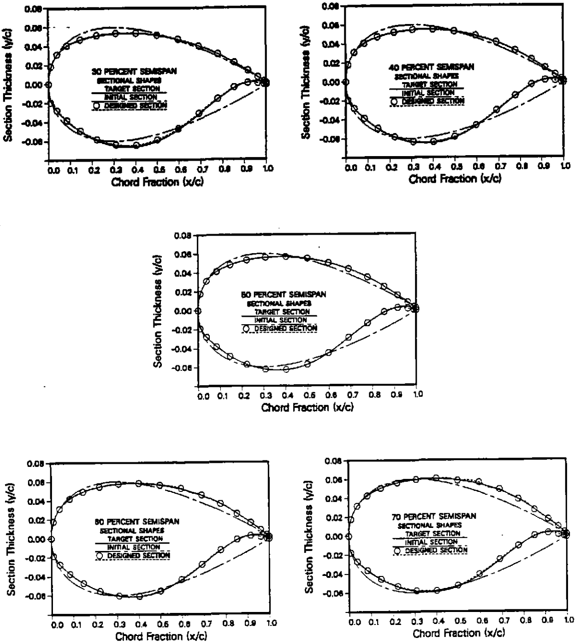

Fig. 57 Comparison of the designed sections with the targets for a case whose design region began 1% aft of the leading edge

wing was designed on from root to tip, and the design region started 10% aft of the leading edge of the wing.

Two separate tests were performed. The first involved a fine design at a nearly incompressible Mach number of .2 using a pressure distribution obtained from an analysis of the target at a Mach number of .1. As can be seen from Fig. 58, thinner section shapes were obtained at the higher Mach number. This thinning is in agreement with the 2-D Prandtl-Glauert similarity rule[45]

$$\frac{\tau_1}{\tau_2} = \frac{\sqrt{1 - M_1^2}}{\sqrt{1 - M_2^2}} \qquad (5-1)$$

which states that the C_p will be invariant with Mach number if the thickness, τ, is reduced as the Mach number is increased for linearized flow. For this case, Eq. (5-1) would predict that a 1.54% decrease in thickness would be necessary to have the same pressure distribution at the higher Mach number. The design code for this 3-D case produced a section which was on the average 1.6% thinner than the NACA 0012 section.

The second case involved a medium grid design at a Mach number of .85 using a pressure distribution obtained at a Mach number of .80. Referring to Fig. 59, the section shapes produced are again thinner than the initial section. The top surface, though, required a sudden thinning of the surface at the shock location. Surprisingly, upon analyzing this wing, the pressure distributions shown in Fig. 60 match quite well with the target everywhere except in the tip region of the wing. So, given the constraints of the problems, it appears that the only way the boundary conditions could be met was to have these dips in the airfoil surface. Since these dips might

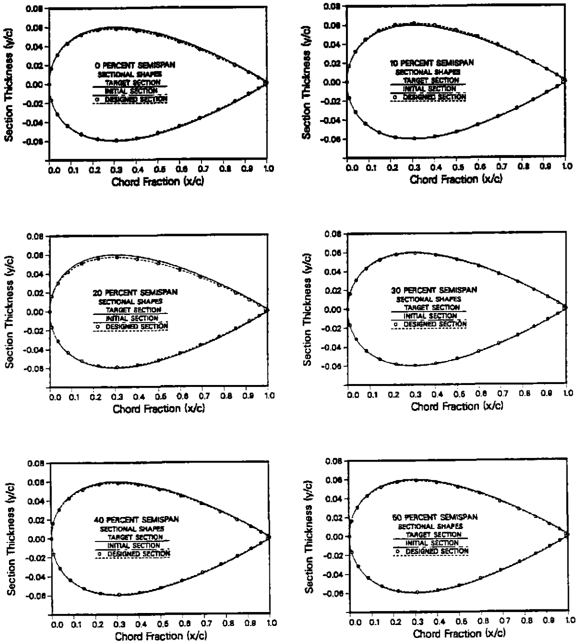

Fig. 58 Comparison of the section designed at a M = .2, using input pressure distributions obtained from an analysis at a M = .1, with the original NACA 0012 sections

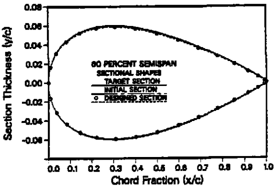

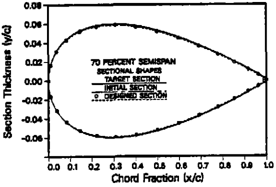

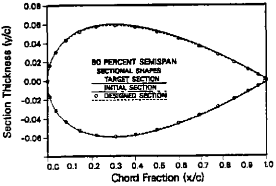

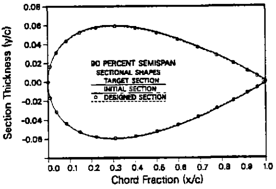

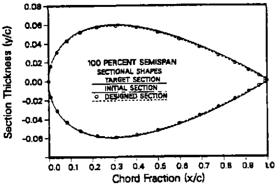

Fig. 58 Continued

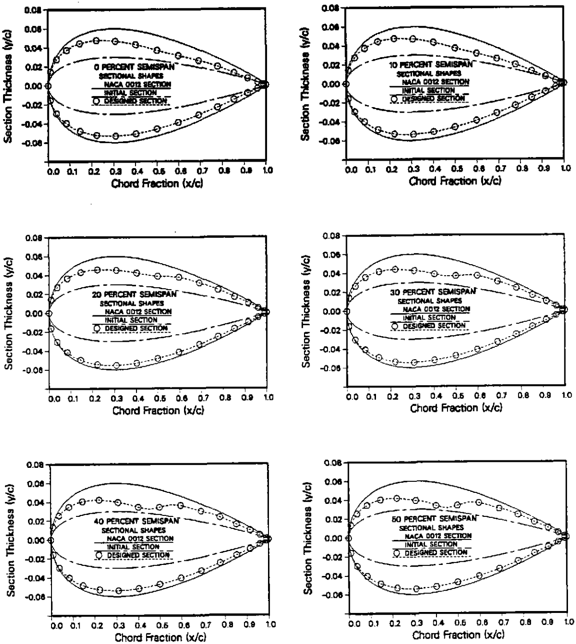

Fig. 59 Comparison of the sections designed at a $M = .85$, using input pressure distributions obtained from an analysis of Lockheed Wing-A with NACA 0012 airfoils at a $M = .8$, with the original NACA 0012 sections and initial NACA 0006 sections

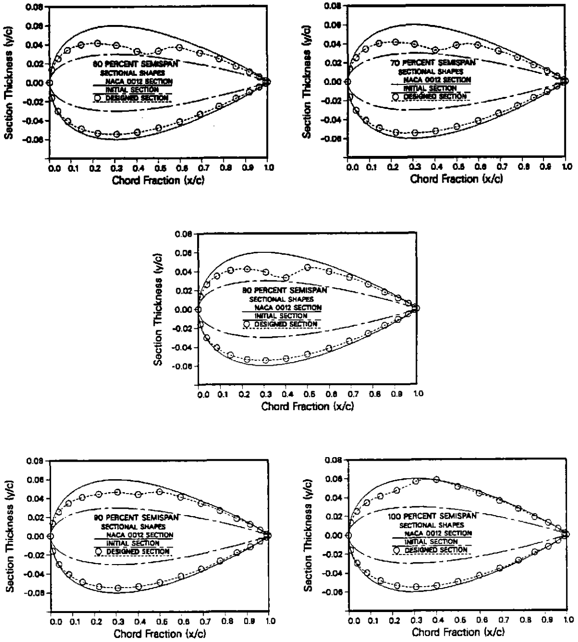

Fig. 59 Continued

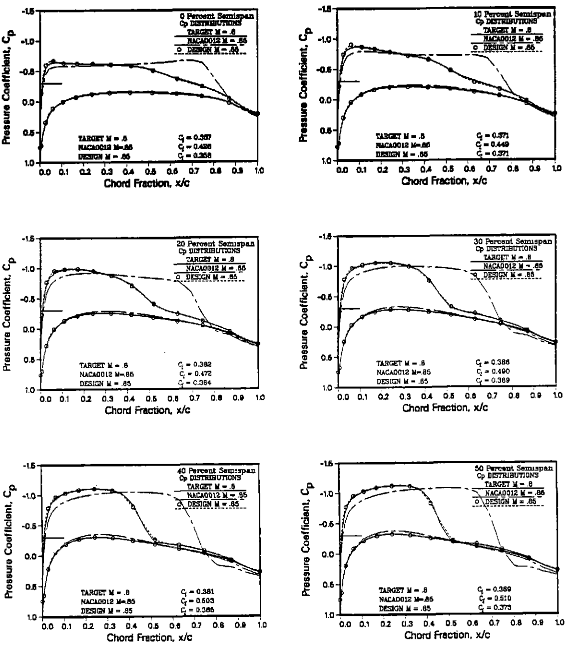

Fig. 60 Comparison of the pressure distributions obtained from an analysis at a M = .85 of the Lockheed Wing-A which was designed at a M = .85 using input pressure distributions obtained from an analysis at a M = .8, with the input pressure distributions

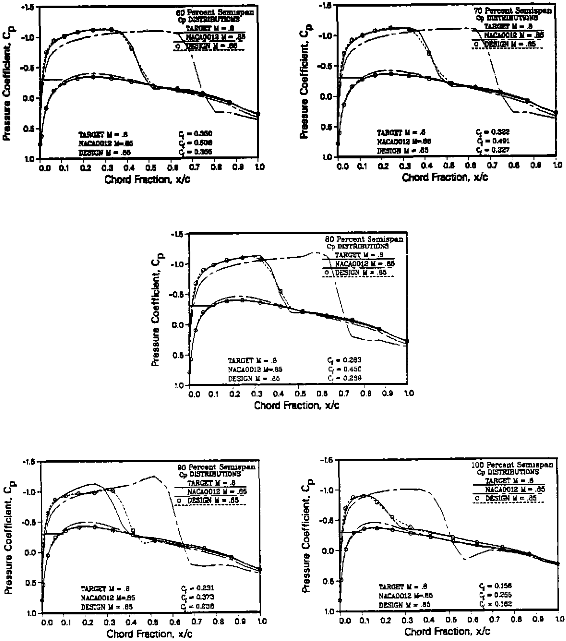

Fig. 60 Continued

lead to boundary layer difficulties, it would probably behoove the designer to vary the Mach number or alter the pressure distribution to eliminate the necessity of these dips.

V.6 Grid Refinement Effects

Since the computational time required for a design on the medium grid is about an eighth of that required on a fine grid, it may be tempting to try to design on the medium grid using fine grid or real pressures. In order to assess the practicality of this approach, a transonic design on a medium grid using fine grid pressures was carried out. The case was performed at a Mach number of .8 and an angle of attack of two degrees. The original supercritical sections for Wing-A were used as the initial, as well as, the target sections. The results are shown in Fig. 61. The only place where the designs came close to the target was near the middle of the wing. A slight wave appears in the upper surfaces of the designed sections near the shock location. This pertubation is due to the smearing of the shock on the medium grid. The section designed at the wing tip deviated considerably from the target. The fact that at the wing tip the fine grid C_l is lower than the medium grid C_l most probably led to the decambering of the sections at the wing tip.

No attempt was made to match the C_L's of the fine grid and medium grid analyses by varying the Mach number or angle of attack, but a comparison of the medium grid pressures at various Mach numbers and angles of attack with the target fine grid pressures for the supercritical wing shown in Fig. 62 reveal that it would probably be necessary to alter the twist of the wing to closely match the C_l's at all

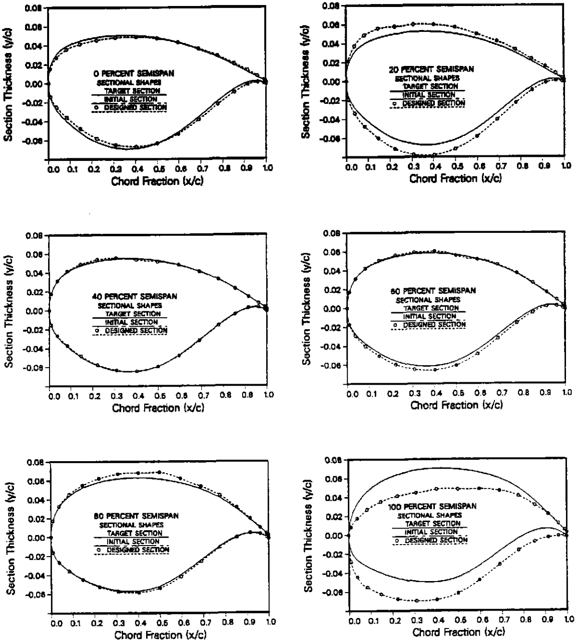

Fig. 61 Comparison of the sections obtained from a medium grid design at M = .8 using input pressure distributions obtained from a fine grid analysis of Lockheed Wing-A with the target sections

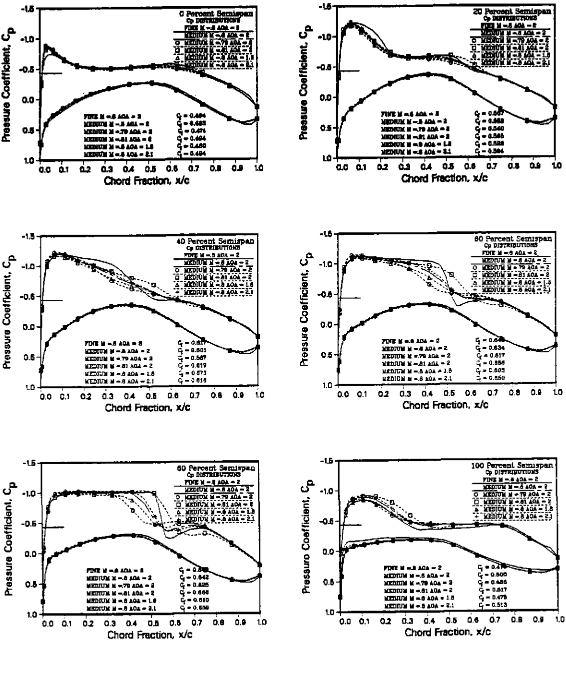

Fig. 62 Comparison of fine grid pressure distributions with medium grid pressure distributions obtained from an analysis of Lockheed Wing-A at various angles of attack and Mach numbers

of the design stations. It also shows that increasing the angle of attack to 2.1° would have produced closer matching C_l's and hence perhaps better designs. In retrospect, though, given that the fine grid pressures are correct or more realistic, it would be necessary, unless appropriate corrections can be found, to use the fine grid to properly design the correct airfoil sections.

V.7 Fixed Trailing Edge Design

This case was investigated to verify that a fixed trailing edge design could be accomplished with the present version of the code. The case chosen utilized Lockheed Wing-A at a Mach number of .8 and an angle of attack of 2°. A NACA 0012 section was used as the initial geometry from 30% to 70% semispan, while the remaining part of the wing used the original supercritical sections. The inverse boundary condition was enforced from 5% to 80% chord. The airfoil aft of 80% chord was fixed so that it maintained the NACA 0012 trailing edge shape. The input pressures were obtained through a medium grid inviscid analysis of the wing with the original supercritical sections used throughout. Furthermore, to provide for a smooth transition at the aft direct-inverse junction, the displacements were smoothed in the chordwise direction. The type II-2 design method was used in this case.

The resulting section shapes are shown in Fig. 63. The target airfoil section would actually be the first 80% of the supercritical section and the last 20% of the NACA 0012 section. Surprisingly, even with the aft portion of the wing fixed, the designed sections came quite close to matching the original Wing-A profiles at the 30% and 50% semispan locations. At the 70% semispan location, the designed section

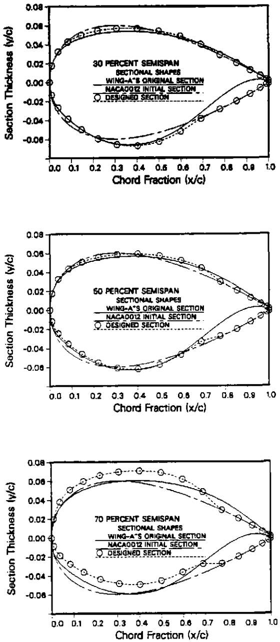

Fig. 63 Comparison of the sectional shapes designed with a fixed trailing edge region with a NACA 0012 and the original Lockheed Wing-A section

as compared to the original Wing-A section is much thicker on top and thinner on the bottom leading to a more cambered profile. This shape is probably due to the interaction of the geometric constraints and the required design pressures. The shock strength of the input C_p distribution does become quite large at this location and it appears that the section may have become more cambered to account for this increase. Or, the increased camber may have been needed to provide the necessary lift required by the inverse boundary condition. The pressure distributions obtained from an inviscid analysis of the resulting shapes are compared with those produced by the original Wing-A sections and the NACA 0012 sections in Fig. 64 The figure reveals that the design pressure distributions are a combination of the Wing-A and NACA 0012 pressure distributions. It is also interesting that it seems a secondary shock near the aft limit of the design region was necessary to meet the constraints of this problem. This very impractical case, of course, was only meant to demonstrate that it is feasible to fix the aft region of the wing. If a more realistic trailing edge were used, better results would surely follow.

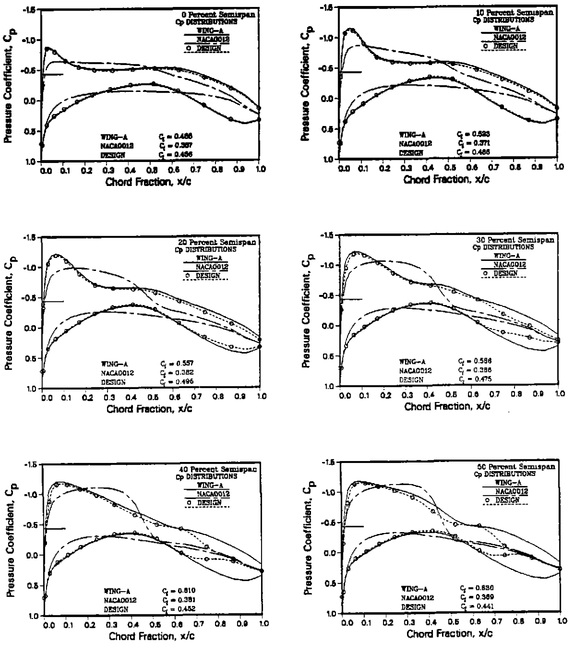

Fig. 64 Comparison of the pressure distributions obtained by an inviscid analysis of the sectional shapes designed with a fixed trailing edge region with those for a NACA 0012 and the original Lockheed Wing-A section. ($M = .8$, $\alpha = 2^o$)

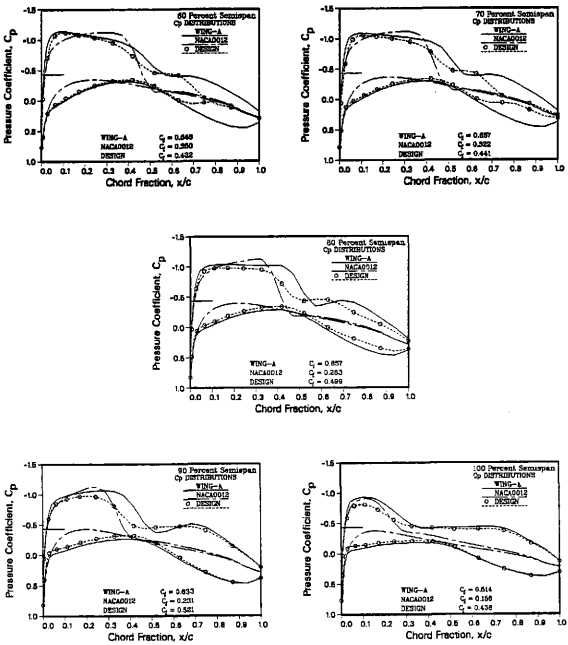

Fig. 64 Continued

CHAPTER VI

CONCLUSIONS AND RECOMMENDATIONS

Progress in the direct-inverse wing design method in curvilinear coordinates has been made, which included the remedying of a spanwise oscillation problem and the assessment of grid skewness, viscous interaction, grid refinement and the initial airfoil section on the final design. Some of the important conclusions were:

(1) In response to the spanwise oscillation problem, designing at every other spanwise station produced the smoothest results for the cases presented.

(2) A smoothly varying grid is especially needed for the accurate design at the wing tip.

(3) The final designed airfoil section is independent of the initial section if the chordwise direct-inverse junction is moved close to the leading edge.

(4) Boundary layer displacement thicknesses must be included in the successful design of a wing in a viscous environment.

(5) Presently the design of only high and medium aspect ratio wings is possible with this code.

(6) A partial wing design beginning aft of the leading edge and terminating prior to the trailing edge is possible with the present method

(7) Designs must be performed on a fine grid.

It is recommended that more work be done to fully understand the fundamental motivation behind the spanwise decoupling problem in order to eliminate all spanwise oscillations in sectional thickness from the solution. This work should also include the development of a better way to handle the formulation of the residual at the spanwise direct-inverse junction to eliminate the initial spanwise jump in the residual located there. Furthermore, the design scheme at the wing root and tip should be refined to provide more accurate airfoil sections in those regions.

In addition, the necessary logic should be added to begin the integration of the flow tangency boundary condition on either side of the section's stagnation point at the present iteration level. This addition should allow the entire airfoil section to be designed with the pressure boundary condition specified everywhere on the wing's surface except at the stagnation point.

Prelimenary results have indicated that by allowing the trailing edge ordinate to float an untwisted wing can be twisted. If this is a well-posed problem, methods should be devised to accurately calculate the twist given the inverse displacements at the present time level and to include this in the iterative process such that the twist angle converges without undue oscillation. It would also be interesting to investigate the possibility of also allowing the leading edge ordinate to vary in a constrained fashion so that the local dihedral angle could change.

And finally, since the potential solution and, hence, the design, converge rather slowly due to the SLOR numerical scheme, the design scheme should be incorporated into the multi-grid version of FLO-30 to hasten convergence.

REFERENCES

1 Agrawal, S., Vermeland, R.E, and Lowrie, R.B., "Euler Transonic Solutions Over Finite Wings," presented at the AIAA 26^{th} Aerospace Sciences Meeting, Reno, Nevada, January 11-14, 1988, AIAA paper 88-0009.

2 Vatsa, V.N., "Navier-Stokes Solutions for Transonic Flow Over a Wing Mounted in a Tunnel," presented at the AIAA 26^{th} Aerospace Sciences Meeting, Reno, Nevada, January 11-14, 1988, AIAA paper 88-0102.

3 Pulliam, T.H., "Euler and Thin Layer Navier-Stokes Codes: ARC2d, ARC3d," Master's Thesis, NASA Ames Research Center, Moffett Field, California, 1987.

4 Campbell, R.C., and Smith, L.A., "A Hybrid Algorith for Transonic Airfoil and Wing Design," presented at the AIAA 5th Applied Aerodynamics Conference, Monterey, California, August 17-19, AIAA paper 88-0009.

5 Carlson, L. A., "Transonic Airfoil Flowfield Analysis Using Cartesian Coordinates," NASA CR-2577, August 1975.

6 Carlson, L. A., "Transonic Airfoil Design Using Cartesian Coordinates," NASA CR-2578, April 1976.

7 Carlson, L. A., "Inverse Transonic Airfoil Design Including Viscous Interaction," NASA CP-2001, November, 1976.

8 Carlson, L. A., "TRANDES: A Fortran Program for Transonic Airfoil Analysis or Design," NASA CR-2821, June 1977.

9 Carlson, L.A., Ratcliff, R.R., Gally, T. A. , "Inverse Wing Design In Transonic Flow Including Viscous Interaction," *Transonic Symposium*, NASA Langley Research Center, Hampton, Virginia, April 19-21, 1988, NASA CP-3020, Vol. 1, Part 2, pp. 497.

10 Carlson, L.A. and Weed, R.A, "A Direct-Inverse Transonic Wing-Design Analysis With Viscous Interaction," *AIAA Proceedings*, Colorado Springs, Colorado, October 14-16, pp. 1-11. 1985

11 Carlson, L.A. and Weed, R.A, "A Direct-Inverse Transonic Wing Analysis-Design Method with Viscous Interaction," *Journal of Aircraft*, vol. 23, September, 1986, pp. 711-718.

12 Carlson, L. A., Rocholl, B. M., "Application of Direct-Inverse Techniques to Airfoil Analysis and Design," *Advanced Technology Airfoil Research*, Langley Research Center, Hampton, Virginia, NASA CP-2045, Part 1, June 1977.

13 Gally, T. A., "Inverse Transonic Wing Design Using Finite-Volume Methods in Curvilinear Coordinates," Master's Thesis, Texas A&M University, May 1987.

14 Gally, T. A. and Carlson, L. A., "Inverse Transonic Wing Design Using Inverse Methods in Curvilinear Coordinates," *5th Applied Aerodynamics Conference*, Monterey, California, August 17-19, 1987, pp. 516-526.

15 Gally, T.A. and Carlson, L.A., "Transonic Wing Design Using Inverse Methods in Curvilinear Coordinates," *Journal of Aircraft*, vol. 25, November, 1988, pp. 1009-1017.

16 Weed, R. A., Anderson, W. K., and Carlson, L. A., "A Direct-Inverse Three-Dimensional Transonic Wing Design Method for Vector Computers," AIAA Paper 84-2156, August 1984.

17 Weed, R.A, Carlson, L.A., "A Direct-Inverse Three-Dimensional Transonic Wing Design Method for Vector Computers," *AIAA 2^{nd} Applied Aerodynamics Conference*, Seattle, Washington, AIAA paper 84-2156, pp. 1, August, 21-23, 1984.

18 Anderson, W. K., and Carlson, L. A., "Inverse Transonic Wing Design on a Vector Processor," Texas A&M Research Foundation Report TAMRF-4535-8212, December 1982.

19 Schlicting, Herman, *Boundary Layer Theory*, 7^{th} Edition, McGraw-Hill Book Co., New York, New York, 1979.

20 Streett, C.L, "Viscous-Inviscid Interaction For Transonic Wing-Body Configurations Including Wake Effects," *AIAA Journal*, vol. 20. July,1982. pp. 915.

21 Smith, P.D., "An Integral Prediction Method For Three-Dimensional Turbulent Boundary Layers," *Royal Aeronautical Establishment R&M* , vol. 3739, 1972, pp. 1-54.

22 Stock, H.W., "Integral Method for the Calculation of Three-Dimensional, Laminar and Turbulent Boundary Layers," NASA TM-75320, N78-27365, July, 1978.

23 Shankar, V., Malmuth, N.D, "Computational Transonic Design Procedure for Three-Dimensional Wings and Wing-Body Combinations," presented at the

17^{th} Aerospace Sciences Meeting, New Orleans, Louisiana, January 15-17, 1979, AIAA paper 79-0344.

24 Shankar, V. and Malmuth, N.D.,, "Computational Transonic Inverse Procedure for Wing Design," AIAA Paper 80-1390R, 1980.

25 Melson, N. D. and Streett, C. L., "TAWFIVE: A User's Guide," NASA TM84619, September 1983.

26 Green, J.E., "The Prediction of Turbulent Boundary Layer Development in Compressible Flow," *Fluid Mechanics*, vol. 31, part 4, 1968, pp. 753–778.

27 Green, J.E., Weeks, D.J., Brooman, J.W.F, "Prediction of Turbulent Boundary Layers and Wakes in Compressible Flow by a Lag-Entrainment Method," RAE TR - 72231, January, 1973.

28 Green, J.E., "Application of Head's Entrainment Method to the Prediction of Turbulent Boundary Layers and Wakes in Compressible Flow," RAE TR - 72079, June, 1972.

29 Jameson, Anthony, "Iterative Solution of Transonic Flows over Airfoils and Wings, Including Flows at Mach 1," *Comm. Pure Appl. Math.*, vol. 27, 1974, pp. 283-309.

30 Jameson, Anthony, "Transonic Potential Flow Calculations Using Conservative Form," *Proceedings of AIAA 2nd Computational Fluid Dynamics Conference*, Hartfort, Connecticut, June 1975, pp. 148-161.

31 Jameson, Anthony and Caughey, D. A., "A Finite Volume Method for Transonic Potential Flow Calculations," *Proceedings of AIAA 3rd Computational Fluid Dynamics Conference*, Albuquerque, New Mexico, June 1977, pp. 35-54.

32 Caughey, D.A., and Jameson, Anthony, "Numerical Calculation of Transonic Potential Flow about Wing-body Combinations," *AIAA Journal*, vol. 77-677, 1977, pp. 175-181.

33 Caughey, D.A., "A Systematic Procedure for Generating Useful Conformal Mappings," *International Journal for Numerical Methods in Engineering*, vol. 12, 1978, pp. 1651-1657.

34 Caughey, D. A. and Jameson, Anthony, "Progress in Finite-Volume Calculation for Wing-Fuselage Combinations," AIAA Paper 79-1513R, 1979.

35 Caughey, D.A., "Multi-Grid Calculation of Three-Dimensional Transonic Potential Flows," *AIAA 21st Aerospace Sciences Meeting*, Reno, Nevada, AIAA paper 83-0374, pp. 1-9, January 10-13, 1983.

36 Anderson, D.A., Tannehill, J.C., and Pletcher, R.H., *Computational Fluid Mechanics and Heat Transfer*, First Edition, Hemisphere Publishing Co., Washington, New York, London, 1984, pp. 50–53,63–66.

37 Melnik, R.E., Chow, R., and Mead, H.R., "Theory of Viscous Transonic Flow Over Airfoils at High Reynolds Number," presented at the AIAA Plasma Dynamics Conference, , 1977, no. 77, pp. 651-700.

38 Cumpsty, N.A. and Head, M.R., "The Calculation of Three-Dimensional Turbulent boundary Layers, Part II: Attachment-Line flow on an Infinite Swept Wing," Aeronautical Quarterly, vol. XVIII, pp. 150, July 1966.

39 Lock, R.C, "A Review of Methods for Predicting Viscous Effects on Aerofoils and Wings at Transonic Speeds," Royal Aircraft Establishment, London. England, pp. 2-9.

40 Bristow, D. R., and Hawk, J.D., "Subsonic Panel Method for Designing Wing Surfaces From Pressure Distribution," NASA CR-3713, 1983.

41 Davis, W., "TRO-2D: A Code for Rational Transonic Aero Optimization," AIAA Paper 85-0425, January 1985.

42 Holman, Jack P., *Experimental Methods for Engineers*, 4^{th} Edition, McGraw-Hill Book Co., New York, New York, 1984.

43 Volpe, G., and Melnik, R.E,, "The Role of Constraints in the Inverse Design Problem for Transonic Airfoils," presented at the AIAA 14^{th} Fluid and Plasma Dynamics Conference, Palo Alto, California, June 23-25, 1981, AIAA paper 81-1233.

44 Flores, J., Holst, T.L., Kwak, D., and Batiste, D., "A New Consistent Spatial Differncing Scheme for the Transonic Full Potential Equation," presented at the AIAA 21^{th} Aerospace Sciences Meeting, Reno, Nevada, January 10-13, 1983, AIAA paper 83-0373.

45 Liepmann, H.W., and Roshko, A., *Elements of Gasdynamics*, 1^{st} Edition, John Wiley & Sons, Inc., New York, New York, 1957.

Supplementary Sources Consulted

1 Bauer, F., Garabedian, P., and McFadden, G., "The NYU Inverse Swept Wing Code," NASA CR-3662, January 1983.

2 Boppe, C. W., "Transonic Flow Field Analysis for Wing-Fuselage Configurations," NASA CR-3243, 1980.

3 Bristow, D.R. and Hawk, J.D., "A Mixed Analysis and Design Surface Panel Method for Two-Dimensional Flows," *AIAA 2^{nd} Applied Aerodynamics Conference*, Orlando, Florida, AIAA paper 82-0022, pp. January 11-14, 1982.

4 Cosentino, G. B. and Holst, T. L., "Numerical Optimization Design of Advanced Transonic Wing Configurations," AIAA Paper 85-0424, January 1985.

5 Daripa, P.K., and Sirovich, Lawrence, "Exact and Approximate Gas Dynamics Using the Tangent Gas," *Journal of Computational Physics*, vol. 62 no. 2, February, 1986, pp. 400-413.

6 Daripa, P.K., and Sirovich, Lawrence, "An Inverse Method for Subcritical Flows," *Journal of Computational Physics*, vol. 63 no. 2, April, 1986, pp. 311-328.

7 Daripa, P.K., "A Fast Approach to Designing Airfoils from Given Pressure Distribution in Compressible Flows," presented at the AIAA/AHS/ASEE Aircraft Design, Systems and Operations Meeting, St. Louis, Missouri, September 14-16, 1987, AIAA paper 87-2862.

8 Daripa, P.K, "On Inverse Airfoil Design," presented at the AIAA 6^{th} Applied Aerodynamics Conference, Williamsburg, Virginia, June 6-8, 1988, AIAA paper 88-2573.

9 Daripa, P.K., "An Exact Inverse Method for Subsonic Flows," *Quarterly of Applied Mathematics*, vol. XLVI, Number 3, September, 1988, pp. 505-526.

10 Hassan, A., Sobieczky, H., Seebass, A.R., "Subsonic Airfoils with a Given Pressure Distribution," *AIAA Journal*, vol. 22, No. 9, September 1984, pp. 1185-1191.

11 Hess, J.L., "Calculation of Potential Flow About Arbitrary Three -Dimensional Lifting Bodies," Aerodynamics Division, Douglas Aircraft Company, Longbeach, California, MDC J5679-01, October, 1972.

12 Hicks. R., "Wing Design by Numerical Optimization," presented at the AIAA Aircraft Systems & Technology Meeting, Seattle, Washington, August 22-24, 1977, AIAA Paper 77-1247.

13 Holst, Terry L. and Ballhaus, William F., "Fast, Conservative Schemes for the Full Potential Equation Applied to Transonic Flow," *AIAA Journal*, vol. 17 no. 2, Febuary 1979, pp. 145-152.

14 Holst, T. and Thomas, S., "Numerical Solution of Transonic Wing Flow Fields," presented at the AIAA 20^{th} Aerospace Sciences Meeting, Orlando, Florida, January 11-14, 1982, AIAA paper 82-0105.

15 Holst, Terry L., "Numerical Solution of Transonic Potential Flows," Handout #4, AA 292S, .Stanford University, July, 1982

16 Kaplan, W., *Advanced Calculus*, Third Edition, Addison-Wesley Publishing, Reading, Massachusetts, August, 1984, pp. 44,101,94–99,110–117,122–125.

17 Klopfer, G.H. and Nixon, D., "Non-Isentropic Potential Formulation for Transonic Flows," *AIAA 21^{st} Aerospace Sciences Meeting*, Reno, Nevada, AIAA paper 83-0375, pp. January 10-13, 1983.

18 Ludford, G. S. S., "the Behavior at Infinity of the Potential Function of a Two Dimensional Subsonic Compressible Flow," *Journal of Mathematics and Physics*, vol. XXX, Number 3, October, 1951, pp. 117-130.

19 Malone, J. B., "An Optimal Surface Transpiration Subsonic Panel Method for Iterative Design of Complex Aircraft Configurations," *Fourteenth Fluid and Plasma Dynamics Conference*, Palo Alto, California, AIAA paper 81-1254, pp. 1-9, June 23-25, 1981.

20 Miranda, L.R., "A Perspective of Computational Aerodynamics from the Viewpoint of Airplane Design Applications," *AIAA 20^{th} Aerospace Sciences Meeting*, Orlando, Florida, AIAA paper 82-0018, pp. January 11-14, 1982.

21 Smith, C.W., Braymen, W.W., Bhateley, I.C., and Londenberg, W.K, "The Application of CFD to Military Aircraft Design at Transonic Speeds," presented at the Transonic Symposium, NASA Langley Research Center, Hampton, Virginia, April 19-21, 1988.

22 Strand, T., "Exact Method of Designing Airfoils With Given Velocity Distributions in Incompressible Flow," *Journal of Aircraft*, vol. Vol. 10, No 11, November 1973, pp. 651-659.

23 Tatsumi, S. and Takanashi, S., "Experimental Verification of Three-Dimensional Transonic Inverse Method," AIAA Paper 85-4077, October 1985.

24 Woodrow, W., Jr., "Application of a Nonisentropic Full Potential Method to Agard Standard Airfoils," AIAA paper 88-0710, 1988.

25 Woods, L. C., "The Design of Two-Dimesional Aerofoils With Mixed Boundary Conditions," *Quarterly of Applied Mathematics*, vol. 13, 1955, pp. 139-146.

APPENDIX A

DERIVATION OF THE FULL POTENTIAL EQUATION IN CURVILINEAR COORDINATES

The full potential equation transformed from cartesian to curvilinear coordinates is derived here as a courtesy to the reader.

The full potential or the continuity equation written in cartesian coordinates is

$$(\rho u)_x + (\rho v)_y + (\rho w)_z = 0 \qquad (A-1)$$

where

$$\rho = \left(1 - \frac{\gamma - 1}{\gamma + 1}\left(u^2 + v^2 + w^2\right)\right)^{\frac{1}{\gamma - 1}} \qquad (A-2)$$

It is desired to transform this equation to a curvilinear coordinate system of ξ, η, and ζ where

$$\xi = \xi\,(x, y, z) \qquad \eta = \eta\,(x, y, x) \qquad \zeta = \zeta\,(x, y, z) \qquad (A-3)$$

By using the standard chain rule, the following operators can be defined

$$\begin{aligned}
\frac{\partial}{x} &= \xi_x \frac{\partial}{\xi} + \eta_x \frac{\partial}{\eta} + \zeta_x \frac{\partial}{\zeta} \\
\frac{\partial}{y} &= \xi_y \frac{\partial}{\xi} + \eta_y \frac{\partial}{\eta} + \zeta_y \frac{\partial}{\zeta} \\
\frac{\partial}{z} &= \xi_z \frac{\partial}{\xi} + \eta_z \frac{\partial}{\eta} + \zeta_z \frac{\partial}{\zeta}
\end{aligned} \qquad (A-4)$$

Using these operators in Eq. (A-1) yields

$$\begin{aligned}
&\xi_x (\rho u)_\xi + \eta_x (\rho u)_\eta + \zeta_x (\rho u)_\zeta \\
&+ \xi_y (\rho v)_\xi + \eta_y (\rho v)_\eta + \zeta_y (\rho v)_\zeta \\
&+ \xi_z (\rho w)_\xi + \eta_z (\rho w)_\eta + \zeta_z (\rho w)_\zeta = 0
\end{aligned} \qquad (A-5)$$

Defining the Jacobian, J, as

$$J = \frac{\partial(\xi,\eta,\zeta)}{\partial(x,y,z)} = \begin{vmatrix} \xi_x & \xi_y & \xi_z \\ \eta_x & \eta_y & \eta_z \\ \zeta_x & \zeta_y & \zeta_z \end{vmatrix} \qquad (A-6)$$

Then after Holst, multiplying the Eq. (A-5) by J^{-1}, and rearranging to conservative form plus remainder gives

$$\begin{aligned}
&\left[\left((\rho u)\,\xi_x J^{-1}\right) + \left((\rho v)\,\xi_y J^{-1}\right) + \left((\rho w)\,\xi_z J^{-1}\right)\right]_\xi \\
&+ \left[\left((\rho u)\,\eta_x J^{-1}\right) + \left((\rho v)\,\eta_y J^{-1}\right) + \left((\rho w)\,\eta_z J^{-1}\right)\right]_\eta \\
&+ \left[\left((\rho u)\,\zeta_x J^{-1}\right) + \left((\rho v)\,\zeta_y J^{-1}\right) + \left((\rho w)\,\zeta_z J^{-1}\right)\right]_\zeta \\
&- (\rho u)\left[\left(\xi_x J^{-1}\right)_\xi + \left(\eta_x J^{-1}\right)_\eta + \left(\zeta_x J^{-1}\right)_\zeta\right] \\
&- (\rho v)\left[\left(\xi_y J^{-1}\right)_\xi - \left(\eta_y J^{-1}\right)_\eta + \left(\zeta_y J^{-1}\right)_\zeta\right] \\
&- (\rho w)\left[\left(\xi_z J^{-1}\right)_\xi + \left(\eta_z J^{-1}\right)_\eta + \left(\zeta_z J^{-1}\right)_\zeta\right] = 0
\end{aligned} \qquad (A-7)$$

Now using the fact that

$$\frac{\partial J^{-1}}{\partial s} = -J^{-2}\frac{\partial J}{\partial s} \qquad (A-8)$$

the last three terms in brackets can be shown to be zero. For example, equating the first of these terms to zero

$$(\rho u)\left[\left(\xi_x J^{-1}\right)_\xi + \left(\eta_x J^{-1}\right)_\eta + \left(\zeta_x J^{-1}\right)_\zeta\right] = 0 \qquad (A-9)$$

and expanding the derivatives and collecting like terms gives

$$\begin{aligned}
&J^{-1}\left[(\xi_x)_\xi + (\eta_x)_\eta + (\zeta_x)_\zeta\right] \\
&- J^{-2}\left[\xi_x J_\xi - \eta_x J_\eta + \zeta_x J_\zeta\right] = 0
\end{aligned} \qquad (A-10)$$

Rewriting Eq. (A-4) in matrix notation

$$\begin{pmatrix} \frac{\partial}{x} \\ \frac{\partial}{y} \\ \frac{\partial}{z} \end{pmatrix} = \begin{pmatrix} \xi_x & \eta_x & \zeta_x \\ \xi_y & \eta_y & \zeta_y \\ \xi_z & \eta_z & \zeta_z \end{pmatrix} \begin{pmatrix} \frac{\partial}{\xi} \\ \frac{\partial}{\eta} \\ \frac{\partial}{\zeta} \end{pmatrix} \qquad (A-11)$$

After solving for $\frac{\partial}{\partial\xi}, \frac{\partial}{\partial\eta}, \frac{\partial}{\partial\zeta}$, this becomes

$$\begin{pmatrix} \frac{\partial}{\partial\xi} \\ \frac{\partial}{\partial\eta} \\ \frac{\partial}{\partial\zeta} \end{pmatrix} = \begin{pmatrix} A_{11} & -A_{12} & A_{13} \\ -A_{21} & A_{22} & -A_{23} \\ A_{31} & -A_{32} & A_{33} \end{pmatrix} \begin{pmatrix} \frac{\partial}{\partial x} \\ \frac{\partial}{\partial y} \\ \frac{\partial}{\partial z} \end{pmatrix} [J^{-1}] \qquad (A-12)$$

where :

$$\begin{aligned} A_{11} &= \eta_y\zeta_z - \zeta_y\eta_z \quad A_{12} = \xi_y\zeta_z - \xi_z\zeta_y \quad A_{13} = \xi_y\eta_z - \eta_y\xi_z \\ A_{21} &= \eta_x\zeta_z - \eta_z\zeta_x \quad A_{22} = \xi_x\zeta_z - \xi_z\zeta_x \quad A_{23} = \xi_x\eta_z - \xi_z\eta_x \\ A_{31} &= \eta_x\zeta_y - \eta_y\zeta_x \quad A_{32} = \xi_x\zeta_y - \xi_y\zeta_x \quad A_{33} = \xi_x\eta_y - \eta_x\xi_y \end{aligned} \qquad (A-13)$$

These operators can be used to expand the derivatives of ξ_x, η_x, and ζ_x so that

$$\begin{aligned} (\xi_x)_\xi &= [A_{11}\xi_{xx} - A_{21}\xi_{xy} + A_{31}\xi_{xz}]\, J^{-1} \\ (\eta_x)_\eta &= [A_{12}\eta_{xx} - A_{22}\eta_{xy} + A_{32}\eta_{xz}]\, J^{-1} \\ (\zeta_x)_\zeta &= [A_{13}\zeta_{xx} - A_{23}\zeta_{xy} + A_{33}\zeta_{xz}]\, J^{-1} \end{aligned} \qquad (A-14)$$

Substituting these into Eq. (A-10) and collecting terms yields

$$\begin{aligned} &J^{-2}[A_{11}\xi_{xx} - A_{21}\xi_{xy} + A_{31}\xi_{xz} \\ &-A_{12}\xi_{xx} - A_{22}\xi_{xy} + A_{32}\xi_{xz} \\ &+A_{13}\xi_{xx} - A_{23}\xi_{xy} + A_{33}\xi_{xz}] \\ -&J^{-3}[A_{11}J_x\xi_x - A_{21}J_y\xi_x + A_{31}J_z\xi_x \\ &-A_{12}J_x\eta_x - A_{22}J_y\eta_x + A_{32}J_z\eta_x \\ &+A_{13}J_x\zeta_x - A_{23}J_y\zeta_x - A_{33}J_z\zeta_x] = 0 \end{aligned} \qquad (A-15)$$

$$\text{with} \quad J = \xi_x A_{11} - \eta_x A_{12} + \zeta_x A_{13}$$

Expanding the second term in brackets in the previous equation to

$$\begin{aligned} -J^{-3}[&J_x J + J_y(\xi_x\eta_z\zeta_x - \xi_x\eta_x\zeta_z \\ &+\xi_x\eta_x\zeta_z - \xi_z\eta_x\zeta_x + \xi_z\eta_x\zeta_x - \xi_x\eta_z\zeta_x) \\ &+J_z(\xi_x\eta_x\zeta_y - \xi_x\eta_y\zeta_x - \xi_x\eta_x\zeta_y \\ &+\xi_y\eta_x\zeta_x + \xi_x\eta_y\zeta_x - \xi_y\eta_x\zeta_x)] \end{aligned} \qquad (A-16)$$

and cancelling like terms, this reduces simply to

$$\text{Second term } = J^{-2}J_x \qquad (A-17)$$

$$\begin{aligned} \text{where : } J_x =&\xi_x (A_{11})_x - \eta_x (A_{12})_x + \zeta_x (A_{13})_x \\ &+ \xi_{xx}A_{11} - \eta_{xx}A_{12} + \zeta_{xx}A_{13} \end{aligned} \qquad (A-18)$$

Partially expanding J_x to

$$\begin{aligned} J_x =&\xi_{xx}A_{11} - \eta_{xx}A_{12} + \zeta_{xx}A_{13} \\ &+\xi_x (\eta_{xy}\zeta_z + \eta_y\zeta_{xz} - \eta_z\zeta_{xy} - \zeta_y\eta_{xz}) \\ &-\eta_x (\xi_{xy}\zeta_z + \xi_y\zeta_{xz} - \xi_{xz}\zeta_y - \xi_z\zeta_{xy}) \\ &+\zeta_x (\xi_{xy}\eta_z + \xi_y\eta_{xz} - \eta_{xy}\xi_z - \eta_y\xi_{xz}) \end{aligned} \qquad (A-19)$$

Upon collection of like terms, this becomes identical to the first term in brackets in Eq. (A-15), thus satisfying the equality. This can be shown to be true of the other remainder type terms in Eq. (A-7).

Now, reducing the conservative part of Eq. (A-7) to

$$\begin{aligned} &\left[J^{-1} ((\rho u)\, \xi_x + (\rho v)\, \xi_y + (\rho w)\, \xi_z)\right]_\xi \\ &+ \left[J^{-1} ((\rho u)\, \eta_x + (\rho v)\, \eta_y + (\rho w)\, \eta_z)\right]_\eta \\ &+ \left[J^{-1} ((\rho u)\, \zeta_x + (\rho v)\, \zeta_y + (\rho w)\, \zeta_z)\right]_\zeta = 0 \end{aligned} \qquad (A-20)$$

and defining the contravariant velocities, U, V, W, as

$$\begin{pmatrix} U \\ V \\ W \end{pmatrix} = \begin{pmatrix} \xi_x & \xi_y & \xi_z \\ \eta_x & \eta_y & \eta_z \\ \zeta_x & \zeta_y & \zeta_z \end{pmatrix} \begin{pmatrix} u \\ v \\ w \end{pmatrix} \qquad (A-21)$$

with

$$\text{h} = J^{-1} = \begin{vmatrix} x_\xi & x_\eta & x_\zeta \\ y_\xi & y_\eta & y_\zeta \\ z_\xi & z_\eta & z_\zeta \end{vmatrix} \qquad (A-22)$$

Eq. (A-20) reduces to the desired conservative form of

$$(\rho \text{h} U)_\xi + (\rho \text{h} V)_\eta - (\rho \text{h} W)_\zeta = 0 \qquad (A-23)$$

APPENDIX B

DERIVATION OF THE C_P EQUATION

Although this derivation probably appears in most good books on aerodynamics, it is included here as a courtesy to the reader.

C_p is defined as

$$C_p = \frac{p - p_\infty}{\frac{1}{2}\rho_\infty {q^2}_\infty} \qquad (B-1)$$

Using the definition of the speed of sound and isentropic relations, this can be rewritten as

$$C_p = \frac{2}{\gamma {M^2}_\infty}\left(\frac{p}{p_\infty} - 1\right) \qquad (B-2)$$

It is desired to obtain a relation for the pressure coefficient, C_p, in terms of soley the freestream Mach number and the local q_∞. This can be easily accomplished by beginning with Eq. (2-14),

$$\rho = (aM_\infty)^{\frac{2}{\gamma-1}} \qquad (B-3)$$

and using the isentropic relation in Eq. (2-10), pressure can be written as

$$\frac{p}{p_\infty} = (aM_\infty)^{\frac{2\gamma}{\gamma-1}} \qquad (B-4)$$

Upon substituting this into Eq. (B-2), equation, C_p becomes

$$C_p = \frac{2}{\gamma {M^2}_\infty}\left((aM_\infty)^{\frac{2}{\gamma-1}} - 1\right) \qquad (B-5)$$

And finally, making use of Eqs. (2-8) and (2-9), the previous equation can be reduced to the desired relation :

$$C_p = \frac{2}{\gamma {M^2}_\infty}\left[\left[1 + \frac{\gamma-1}{2}{M_\infty}^2\left(1 - \frac{q^2}{q^2_\infty}\right)\right]^{\frac{\gamma}{\gamma-1}} - 1\right] \qquad (B-6)$$

where $q^2 = (u^2 + v^2 + w^2)\,{q^2}_\infty$.

VITA

Robert R. Ratcliff was born in the nation's capital of Washington D.C. on January 26, 1963. He grew up in the west Texas town of El Paso and graduated from Irvin high school in 1981. He received a B.S in Mechanical and Aerospace engineering from Texas A&M in the spring of 1986 and a M.S. in Aerospace engineering in August, 1989.

Any correspondance may be addressed to him in care of his mother, Jane E. Ratcliff, at 8706 Magnetic, El Paso, Texas 79904.